Design of Reconfigurable Planar Parallel Robot

by

© Cheng Yin

A Thesis submitted to the

School of Graduate Studies

in partial fulfillment of the requirements for the degree of

Master of Engineering

Faculty of Engineering and Applied Science

Memorial University of Newfoundland

October 2016

St. John’s Newfoundland

Abstract

A 3-RPR planar parallel robot is a kind of planar mechanism; three prismatic actuators connected with the end effector in parallel.

This thesis will begin with the kinematic analysis for the manipulator to determinate the optimized dimension of the manipulator, including the workspace analysis, determinate of Jacobian analysis, and Direction Selective Index (DSI) analysis.

Secondly, a multi-body bond graph system will be built for the 3-RPR planar parallel manipulator (PPM), along with three PID controllers, which give commands to three DC motors respectively. The advantage of bond graphs is that they can integrate different types of dynamics systems. The manipulator, the control and the motor can be modelled and simulated altogether in the same process. The bond graph will be established for each rigid body with body-fixed coordinate's reference frames, which are connected with parasitic elements (damping and compliance) to each other. Furthermore, Virtual Work method will be used to evaluate the previous dynamic analysis result.

Eventually, the Solidworks design will be demonstrated with images, which show the overall appearance and a detailed drawing of this project. After the mechanical design of the manipulator is finished, the controller design is considered as a future work to conduct.

ACKNOWLEDGEMENTS

I would like to express my sincere thanks to my supervisor Dr. Luc Rolland for his guidance and continuous encouragement throughout my research.

I am also grateful to the Research & Development Corporation (RDC) for providing the financial support to this project.

I would like to thank Shengqi Jian, Md Hassan Faghih and Md. Toufiqul Islam who are always willing to help and give suggestions to my research. I was very delighted to work with them in the High Performance Robot Lab during my study.

I would like to thank Dr. Geoff Rideout, Dr. Leonard Lye, Dr. Michael Hinchey and Dr. George Mann for the instruction of four courses over the past two years.

I would also like to thank my parents for their support and encouragement with their heart.

Finally yet importantly, I would like to thank God, the peace of which transcends all understanding, guarding my heart and my mind in Christ Jesus.

Table of Contents

Abstract i

ACKNOWLEDGEMENTS ii

Table of Contents iii

List of Tables x

List of Figures xii

Nomenclature xvii

Abbreviation xxii

Chapter 1 1

Introduction 1

1.1 Parallel Robots 1

1.1.1 The Advantages of Parallel Robots 2

1.1.2 The Disadvantages of Parallel Robots 3

1.1.3 The Origin of the Parallel Robot 4

1.1.4 The Application of Parallel Robot 6

1.2 Break Down of Chapters 11

Chapter 2 13

State of the Art 13

2.1 Variable Actuated Mechanism....13

2.2 Variable Geometry Mechanism....14

2.3 Device for the Movement and Orientation of an Object in Space and Use Thereof in Rapid Machining....16

2.4 Planar Parallel 3-RPR Manipulator....17

Chapter 3....19

Research Project Presentation....19

3.1 The General Task....19

3.2 Constraints....22

3.3 Specifications....23

3.4 Objective of the Thesis....23

3.4.1 The Main Goal of the Thesis....23

3.4.2 The Detailed Objective of the Thesis....24

3.5 Methodology....25

3.5.1 Workspace....25

3.5.2 Singularities....26

3.5.3 Direction Selective Index (DSI)....27

3.5.4 Dynamic Analysis....28

Chapter 4....29

Kinematic Analysis with the Vectorial Approach 29

4.1 Inverse Kinematic Problem (IKP) 29

4.2 Workspace Analysis 32

4.3 Differential Kinematic Analysis 34

4.4 Comparison among Different Configurations 39

4.4.1 Introduction 39

4.4.2 Workspace Analysis 41

4.4.3 Differential Kinematic Analysis 42

4.5 Direction Selective Index (DSI) 44

4.5.1 DSI Equations 44

4.5.2 Comparison 45

4.5.3 Platform Dimension: L_{MP} 52

Chapter 5 58

Kinematic Analysis with the Matrix Approach 58

5.1 Description of Model 58

5.2 Kinematics of 3-RPR PPM 59

5.2.1 Position Analysis 60

5.2.2 Velocity Analysis 62

5.2.3 Acceleration Analysis 64

5.3 Summary 66

Chapter 6 67

Dynamic Analysis 67

6.1 Introduction to Bond Graph 68

6.2 A General Description for the Configuration 69

6.3 Development of Bond Graph Model 71

6.3.1 Body-fixed Coordinates 71

6.3.2 Actuated Parts ($\boldsymbol{\rho i}$) 77

6.3.3 Parasitic Elements 78

6.3.4 DC Motors and PID Control 79

6.3.5 Overall Bond Graph 83

6.4 Initial Values for Kinematics Calculations 85

6.4.1 Inverse Kinematic Equations 85

6.4.2 Initial Orientation of Each Link (th_i) 86

6.4.3 Initial Position of Each Link's Central Point 86

6.5 Bond Graph Simulation 88

6.6 Bond Graph Result 89

6.7 Virtual Work Principle 92

6.7.1 Link Jacobian Matrix 93

6.7.2 Inertia and Applied Wrenches 96

Chapter 7 98

Comparison between Bond Graph and Virtual Work Results 98

7.1 Description of the Model for Comparison 98

7.2 Zero Order Results Comparison 103

7.3 First Order Results Comparison 105

7.4 Second Order Results Comparison 109

7.5 Inverse Dynamic Comparison 112

7.6 Conclusion 115

Chapter 8 116

Robot Hardware Design for Construction 116

8.1 Mechanical Hardware Design 116

8.1.1 The Frame Design 116

8.1.2 The Fixed Joint Design 118

8.1.3 The Moving Platform Design 126

8.1.4 The Moving Platform Revolute Joint Design 127

8.1.5 The Clamp Design 128

8.1.6 The Linear Actuator Attachment Design 135

8.1.7 Introduction to High Performance Linear Actuator 137

8.2 Mechanical Assembly 139

8.2.1 The Moving Platform Assembly 139

8.2.2 The Fixed Revolute Joints and Frame Assembly 140

8.2.3 The Linear Actuator and Potentiometer Assembly 141

8.2.4 Overall Mechanical System Assembly 143

8.3 Electric Hardware Connection 144

8.3.1 Beaglebone Single-board Computer 144

8.3.2 Potentiometer Connection 146

8.3.3 Motor Driver Board Connection 147

8.3.4 Overall Electrical Hardware Connection 149

8.4 Summary 150

Chapter 9 151

Conclusion 151

9.1 Conclusion 151

9.2 Future Work 154

Bibliography 156

Appendix A 162

Surface Plot Matlab Code 162

Appendix B 167

Virtual Work Analysis Matlab Code 167

List of Tables

Table 4.1: Equations Based on Rotational Matrix 31

Table 4.2: Four Typical Configurations to Analyze 40

Table 4.3: Workspace Analysis Result 41

Table 4.4: Determinant of Inverse Jacobian Matrix Analysis Result 43

Table 4.5: Highest and average DSI values 46

Table 4.6: Rotational DSI with different units 47

Table 4.7: DSI analysis results of Configuration 3 48

Table 4.8: DSI analysis results of Configuration 4 50

Table 4.9: Performance Indices Calculation 53

Table 6.1: Some Effort and Flow Quantities (from reference [12]) 68

Table 6.2: Explanations for l_i, $\boldsymbol{\rho i}$ and l_{ri} 70

Table 6.3: Velocity relationship 73

Table 6.4: Explanation of TF, MTF, GY, MGY Elements 76

Table 6.5: Parasitic elements 79

Table 6.6: Explanation of Figure 6.6 81

Table 6.7: Parameter values 83

Table 6.8: Initial Parameters for Simulation 87

Table 6.9: 3D animation result 88

Table 6.10: Moving platform and link kinematic data during simulation 90

Table 6.11: Dynamic data 90

Table 6.12: Error analysis 91

Table 7.1: Inertia Parameters 101

Table 7.2: The input of zero order comparison 105

Table 7.3: The output of zero order comparison 105

Table 7.4: The input of first order comparison 106

Table 7.5: The output of first order comparison 106

Table 7.6: The input of second order comparison 109

Table 7.7: The output of second order comparison 110

Table 7.8: The input of inverse dynamic comparison 114

Table 7.9: The output of inverse dynamic comparison 115

Table 8.1: Bending Moment Calculation 120

Table 8.2: Description of the headers to use 146

List of Figures

Figure 1.1: SCARA robot (image from EPSON website) 2

Figure 1.2: Adept Quattro Pro robot (image comes from adept website) 3

Figure 1.3: Amusement device (US patent NO. 1789680) [38] 4

Figure 1.4: The first industry parallel robot concept (US patent NO. 2213108) [37] 5

Figure 1.5: The improved painting device by W. L. V. Pollard (US patent NO. 2286571) [36] 6

Figure 1.6: Gough platform 7

Figure 1.7: Original Stewart platform design 8

Figure 1.8: Flight simulator today 9

Figure 1.9: Original Delta Robot design (U. S. patent NO. 4976582) [40] 10

Figure 1.10: Delta 3D printer 11

Figure 2.1: Variable actuated mechanism (courtesy of "Institut de Recherche en Cybernétique de Nantes" (IRCCyN)) 14

Figure 2.2: Redundant kinematic mechanism 15

Figure 2.3: The device figure (US Patent 7997161 B2) 16

Figure 2.4: 3-RPR PPM from Robert in 1999 17

Figure 3.1: A sketch of 3-RPR PPM 20

Figure 3.2: Overall manipulator assembling of the 3-RXR 22

Figure 4.1: A sketch of 3-RPR PPM with classic configuration 30

Figure 4.2: Algorithm for the workspace boundary 33

Figure 4.3: Workspace area 34

Figure 4.4: Manipulator configuration with θ_i marking 35

Figure 4.5: Algorithm of the Matlab code to map determinant plot 37

Figure 4.6: Distribution of determinant of Jacobian 38

Figure 4.7: Fixed joints positions in configuration 3 42

Figure 4.8: Highest values of three performance indices 54

Figure 4.9: Average values of three performance indices 55

Figure 4.10: Highest values of two performance indices 56

Figure 4.11: Average values of two performance indices 56

Figure 5.1: 3-RPR link i for kinematic and virtual work analysis 58

Figure 5.2: Moving platform reference 60

Figure 6.1: Bond graph example with causal strokes (from the reference [12]) 68

Figure 6.2: 3-RPR mechanism for bond graph 70

Figure 6.3: The L_i configuration in bond graph 72

Figure 6.4: Bond graph for L_3 75

Figure 6.5: Bond graph for actuated part ($\boldsymbol{\rho i}$) 78

Figure 6.6: DC motor, PID controller and transformer 81

Figure 6.7: Overall bond graph 84

Figure 7.1: Actuated joint in the bond graph model for comparison 99

Figure 7.2: Overall bond graph system 100

Figure 7.3: Moving platform trajectory 101

Figure 7.4: Moving platform position in X direction versus time 102

Figure 7.5: Moving platform position in Y direction versus time 102

Figure 7.6: The comparison result of the leg length in the first joint 103

Figure 7.7: The comparison result of the leg length in the second joint.....104

Figure 7.8: The comparison result of the leg length in the third joint 104

Figure 7.9: The comparison result of the velocity in the first joint 107

Figure 7.10: The comparison result of the velocity in the second joint.....108

Figure 7.11: The comparison result of the velocity in the third joint 108

Figure 7.12: The comparison result of the acceleration in the first joint.....110

Figure 7.13: The comparison result of the acceleration in the second joint 111

Figure 7.14: The comparison result of the acceleration in the third joint.....111

Figure 7.15: The comparison result of the inverse dynamic force in the first joint.....113

Figure 7.16: The comparison result of the inverse dynamic force in the second joint 113

Figure 7.17: The comparison result of the inverse dynamic force in the third joint.....114

Figure 8.1: Fixed frame drawing 117

Figure 8.2: Frame static analysis result.....118

Figure 8.3: Fixed joint assembly.....119

Figure 8.4: Sketch of the force and bending moment applied on the shaft 121

Figure 8.5: Bending moment distribution diagram.....122

Figure 8.6: Displacement distribution due to external loads 124

Figure 8.7: Stress distribution due to external load 125

Figure 8.8: Moving platform design 126

Figure 8.9: The assembly of moving platform revolute joint 127

Figure 8.10: Static analysis result of the platform connector 128

Figure 8.11: Clamp drawing 129

Figure 8.12: Stress Analysis when Closest 130

Figure 8.13: Displacement Analysis when Closest.....131

Figure 8.14: Displacement of Bi Assumption when Closest 131

Figure 8.15: Stress Analysis when Furthest.....132

Figure 8.16: Displacement Analysis when Furthest 133

Figure 8.17: Displacement of Bi Assumption when Furthest.....133

Figure 8.18: Angle error analysis.....134

Figure 8.19: Linear actuator drawing (from Firgelli official website).....135

Figure 8.20: Linear potentiometer drawing (from Firgelli official website) 136

Figure 8.21: Overall assembly of linear actuator and potentiometer.....137

Figure 8.22: High performance linear actuator.....138

Figure 8.23: Overall assembly of the 3-RPR PPM with “X” actuator.....138

Figure 8.24: Connection between fixed revolute joint and “X” actuator.....139

Figure 8.25: Moving platform assembly with joints.....140

Figure 8.26: Plate and frame connection 141

Figure 8.27: Front connection between linear actuator and potentiometer.....141

Figure 8.28: Back connection between linear actuator and potentiometer 142

Figure 8.29: Overall Mechanical System.....143

Figure 8.30: Beaglebone Black Cape Expansion Headers (from Beaglebone official website)

.....145

Figure 8.31: PWM control with 4 timers headers (from Beaglebone official website)...145

Figure 8.32: Potentiometer connection.....147

Figure 8.33: Motor driver board connection.....148

Figure 8.34: Overall electrical hardware connection.....149

Nomenclature

$\boldsymbol{O}$	The Original of the Global Reference Frame
$\boldsymbol{A_i}$	Fixed Points attached to the Base; "i" Ranges from 1 To 3
$\boldsymbol{A_{iX}}$	Fixed Points' Position in X Direction of Global Reference Frame
$\boldsymbol{A_{iY}}$	Fixed Points' Position in Y Direction of Global Reference Frame
$\boldsymbol{B_i}$	Moved Points attached to the End-Effector; "i" Ranges from 1 To 3
$\boldsymbol{B_{ix}}$	Moved Points' Position in X Direction of Global Reference Frame
$\boldsymbol{B_{iy}}$	Moved Points' Position in Y Direction of Global Reference Frame
$\boldsymbol{B_{ix}}'$	Moved Points' Position in X' Direction of Mobile Reference Frame
$\boldsymbol{B_{iy}}'$	Moved Points' Position in Y' Direction of Mobile Reference Frame
Φ	The Orientation of the End-effector
$\boldsymbol{\theta_i}$	The Orientation of i^{th} Link
X	The Position of End-effector in X Direction of Global Reference Frame
Y	The Position of End-effector in Y Direction of Global Reference Frame
$\boldsymbol{L_i}$	The Distance between A_i and B_i
$\boldsymbol{L_{MP}}$	The Side Length of Moving Platform Equilateral Triangle
$\boldsymbol{L_{imin}}$	The Minimum Length of L_i
$\boldsymbol{L_{imax}}$	The Maximum Length of L_i
$\boldsymbol{l_i}$	The Link Connect to Fixed Base
$\boldsymbol{l_{ri}}$	The Link Connect to Mobile Platform
$\boldsymbol{\rho_i}$	The Actuated Segment of Each Leg

$\boldsymbol{\rho_{imin}}$	The Minimum Length of ρ_i
$\boldsymbol{\rho_{imax}}$	The Maximum Length of ρ_i
$\boldsymbol{X_i}$	The X position in Global Frame of i^{th} Link
$\boldsymbol{Y_i}$	The Y position in Global Frame of i^{th} Link
$\boldsymbol{Z_i}$	The Z position in Global Frame of i^{th} Link
$\boldsymbol{X_i'}$	The X position in Body Fixed Frame of i^{th} Link in Bond Graph
$\boldsymbol{Y_i'}$	The Y position in Body Fixed Frame of i^{th} Link in Bond Graph
$\boldsymbol{V_{iX}}$	The Liner Velocity in Global X Direction of an i^{th} Link's General Pont
$\boldsymbol{V_{iY}}$	The Liner Velocity in Global Y Direction of an i^{th} Link's General Point
$\boldsymbol{V_{iX}'}$	V_{iX} in Body Fixed Frame of i^{th} Link in Bond Graph
$\boldsymbol{V_{iY}'}$	V_{iY} in Body Fixed Frame of i^{th} Link in Bond Graph
$\boldsymbol{\dot{X}_i'}$	The Liner Velocity in X_i' Direction of an i^{th} Link's General Pont
$\boldsymbol{\dot{Y}_i'}$	The Liner Velocity in Y_i' Direction of an i^{th} Link's General Point
$\boldsymbol{G_i}$	The Center of Mass for Every l_i Link in Bond Graph
$\boldsymbol{G_{ii}}$	The Center of Mass for Every l_{ri} Link in Bond Graph
$\boldsymbol{A_{i1}}$	The First Point of Every l_i Link in Bond Graph
$\boldsymbol{A_{i2}}$	The Second Point of Every l_i Link in Bond Graph
$\boldsymbol{B_{i1}}$	The First Point of Every l_{ri} Link in Bond Graph
$\boldsymbol{B_{i2}}$	The Second Point of Every l_{ri} Link in Bond Graph
$\boldsymbol{m_i}$	The Mass of l_i Link in Bond Graph
$\boldsymbol{m_{ri}}$	The Mass of l_{ri} Link in Bond Graph

$\boldsymbol{m_p}$	The Mass of Moving Platform
$\boldsymbol{Ora_i}$	The Initial Orientation of Link l_i and l_{ri} in Bond Graph
$\boldsymbol{e_{i1}}$	The position of mass center in Z_i direction in Link L_i
$\boldsymbol{e_{i2}}$	The position of mass center in Z_i direction in Link L_{ri}
$\boldsymbol{^2R_1}$	The rotational matrix from coordinate 2 to coordinate 1
$\boldsymbol{\omega_p}$	Angular velocity of moving platform
$\boldsymbol{\dot{\omega}_p}$	Angular acceleration of moving platform
$\boldsymbol{a_i}$	The position vector of A_i in global reference frame
$\boldsymbol{^Bb_i}$	The position vector of B_i with respect to point C in platform reference
$\boldsymbol{b_i}$	The position vector of B_i with respect to point C in global reference
$\boldsymbol{p}$	The position vector of moving platform in global reference
$\boldsymbol{^is_i}$	Unit vector of link i in body-fixed reference frame
$\boldsymbol{s_i}$	Unit vector of link i in global reference frame
$\boldsymbol{r_{1i}}$	Position vector of m_i in global reference frame
$\boldsymbol{r_{2i}}$	Position vector of m_{ri} in global reference frame
$\boldsymbol{v_{bi}}$	Velocity vector of point B_i
$\boldsymbol{v_p}$	Velocity vector of moving platform
$\boldsymbol{^i\omega_i}$	Angular velocity vector of link i in body-fixed reference frame
$\boldsymbol{^iv_{bi}}$	Linear velocity vector of point B_i in body-fixed reference frame
$\boldsymbol{^iv_{bix}}$	The first row in $\boldsymbol{^iv_{bi}}$
$\boldsymbol{^iv_{biy}}$	The second row in $\boldsymbol{^iv_{bi}}$

$^{i}\boldsymbol{v}_{biz}$	The third row in $^{i}\boldsymbol{v}_{bi}$
$^{i}\boldsymbol{v}_{1i}$	The velocity vector of m_i in body-fixed reference frame
$^{i}\boldsymbol{v}_{ri}$	The velocity vector of m_{ri} in body-fixed reference frame
$\dot{\boldsymbol{v}}_{bi}$	Acceleration vector of point B_i
$\dot{\boldsymbol{v}}_{p}$	Acceleration vector of moving platform
$^{i}\dot{\boldsymbol{\omega}}_{i}$	Angular acceleration vector of link i in body-fixed reference frame
$^{i}\dot{\boldsymbol{v}}_{bi}$	Linear acceleration vector of point B_i in body-fixed reference frame
$^{i}\dot{\boldsymbol{v}}_{bix}$	The first row in $^{i}\dot{\boldsymbol{v}}_{bi}$
$^{i}\dot{\boldsymbol{v}}_{biy}$	The second row in $^{i}\dot{\boldsymbol{v}}_{bi}$
$^{i}\dot{\boldsymbol{v}}_{biz}$	The third row in $^{i}\dot{\boldsymbol{v}}_{bi}$
$^{i}\dot{\boldsymbol{v}}_{1i}$	The acceleration vector of m_i in body-fixed reference frame
$^{i}\dot{\boldsymbol{v}}_{ri}$	The acceleration vector of m_{ri} in body-fixed reference frame
q	The vector of actuated leg length, $[L_1 \quad L_2 \quad L_3]^T$
$\boldsymbol{x}_{i}$	Six-dimensional vector showing position and orientation of link i
$\dot{\boldsymbol{x}}_{i}$	Six-dimensional vector showing linear and angular velocity of link i
$^{i}\dot{\boldsymbol{x}}_{i}$	$\dot{\boldsymbol{x}}_{i}$ in body-fixed reference frame
$\boldsymbol{x}_{p}$	Six-dimensional vector showing position and orientation of platform
$\dot{\boldsymbol{x}}_{p}$	Six-dimensional vector showing linear and angular velocity of platform
$\boldsymbol{\tau}$	Vector of actuated joint forces
$\boldsymbol{\delta}(?)$	Virtual displacement of (?)

$\boldsymbol{f_i}$	Resulting force exerted at the mass center of link i
$\boldsymbol{f_i^*}$	Inertia force exerted at the mass center of link i, $-m_i\dot{\mathrm{v}}_\mathrm{i}$
$\hat{\boldsymbol{f}}_{\boldsymbol{i}}$	$\mathbf{f_i} + \mathbf{f_i^*}$
$\boldsymbol{f_p}$	Resulting force exerted at the mass center of moving platform
$\boldsymbol{f_p^*}$	Inertia force exerted at the mass center of moving platform, $-m_p\dot{\mathrm{v}}_\mathrm{p}$
$\hat{\boldsymbol{f}}_{\boldsymbol{p}}$	$\boldsymbol{f}_\mathbf{p} + \boldsymbol{f_p^*}$
$\boldsymbol{n_i}$	Resulting momentum exerted at the mass center of link i
$\boldsymbol{n_i^*}$	Inertia momentum exerted at the mass center of link i, $-\ {}^{i}I_i\dot{\boldsymbol{\omega}}_{\boldsymbol{i}} -\ {}^{\boldsymbol{i}}\boldsymbol{\omega}_{\boldsymbol{i}} \times (\ {}^{i}I_i\ {}^{\boldsymbol{i}}\boldsymbol{\omega}_{\boldsymbol{i}})$
$\hat{\boldsymbol{n}}_{\boldsymbol{i}}$	$\mathbf{n}_i + \boldsymbol{n_i^*}$
$\boldsymbol{n_p}$	Resulting momentum exerted at the mass center of moving platform
$\boldsymbol{n_p^*}$	Inertia momentum exerted at the mass center of moving platform, $-I_p\dot{\boldsymbol{\omega}}_\mathrm{p} - \boldsymbol{\omega_p} \times (I_p\boldsymbol{\omega_p})$
$\hat{\boldsymbol{n}}_{\boldsymbol{p}}$	$\mathbf{n}_p + \boldsymbol{n_p^*}$
${}^{B}\boldsymbol{I_p}$	The rotational inertia matrix of moving platform in reference B
${}^{O}\boldsymbol{I_p}$	The rotational inertia matrix of moving platform in global reference
${}^{i}\boldsymbol{I_i}$	The rotational inertia matrix of link i in body-fixed reference frame

Abbreviation

DOF	Degree of Freedom
RPR	Revolute Prismatic Revolute
PPM	Planar Parallel Manipulator
DSI	Direction Selective Index

Chapter 1

Introduction

1.1 Parallel Robots

According to the International Organization for Standardization 8373:2012 (ISO 8373:2012) [45], a robot is an "actuated mechanism programmable in two or more axes with a degree of autonomy, moving within its environment, to perform intended tasks." (Autonomy: ability to perform intended tasks based on current state and sensing, without human intervention.)

There are many different methods to classify robots. For instance, individuals could categorize robots by their domain of operation, degree of freedom (DOF), application, or main actuating power source etc. In terms of the manipulator, the most widely used method is to classify robots according to their kinematic chains: serial robot and parallel robots.

Serial and parallel robots are the two main classes. In the class of serial robots, there are some sub-classes: Cartesian robots, Selective Compliance Articulated Robot Arm (SCARA robot), articulated robots, etc. [23]. Series of links are connected by joints from a base to an end-effector within a serial robot. Between different rigid links, there are joints with different actuated methods to connect these parts together. A typical serial robot is shown in Figure 1.1, which is called SCARA robot.

Figure 1.1: SCARA robot (image from EPSON website)

"A parallel robot is made up of an end-effector with n degrees of freedom, and of a fixed base, linked together by at least two independent kinematic chains. Actuation takes place through n simple actuators." [35] In the class of parallel robots, there are several sub-classes as well: Stewart-Gough platform, Delta robot, five-bar robot, etc. [23]. It consists of several chains of links, which connect to the end-effector or platform in parallel. Unlike a serial manipulator, the parallel manipulator has several passive joints which do not need to be actuated during the moving process.

1.1.1 The Advantages of Parallel Robots

The advantages of parallel robots are the following. Parallel robots have less mass thereby achieve faster accelerations or better torque or power transmission to the end-effector. As a result, they are not like the serial robots which cumulate errors from flexibility. In a serial manipulator, flexibility errors may be amplified by the distance from the base to end-effector.

Moreover, as there are actuators located in each joint, the serial robot has a bigger mass compared with parallel manipulators. In order to obtain a more accuracy, designers have to use more rigid joints and larger bodies to overcome errors. On the other hand, parallel robots can obtain a high performance with less mass. In Figure 1.2, a typical parallel manipulator, the Quattro Pro robot, is shown. It can reach a maximum speed of 10 m/s and a maximum acceleration of 150 m/s^2.

Figure 1.2: Adept Quattro Pro robot (image comes from adept website)

1.1.2 The Disadvantages of Parallel Robots

On the other hand, the parallel robots have a more limited workspace. The limited workspace is due to the added mechanical constraints from having more than one chain in parallel. As most of the parallel manipulators have several chains, the link groups could interact with each other to produce the end-effector motion. This also generates singularity

curves within the workspace. However, the disadvantage does not have an influence on the advantages. In summary, any robot with parallel configuration is still better than any serial one for high performance applications.

1.1.3 The Origin of the Parallel Robot

In 1931, an image of a parallel mechanism came from J. E. Gwinnett, called "Amusement Device" in the US patent 1789680 [38]. That device was just an idea of motion platform to bring excitement during movies. Audiences were supposed to have a physical experience associated with the show on the screen. This mechanism had many degrees of freedom and it was impossible for the industry to control it at that time. However, this was the first concept of a parallel mechanism in history. It is shown in Figure 1.3:

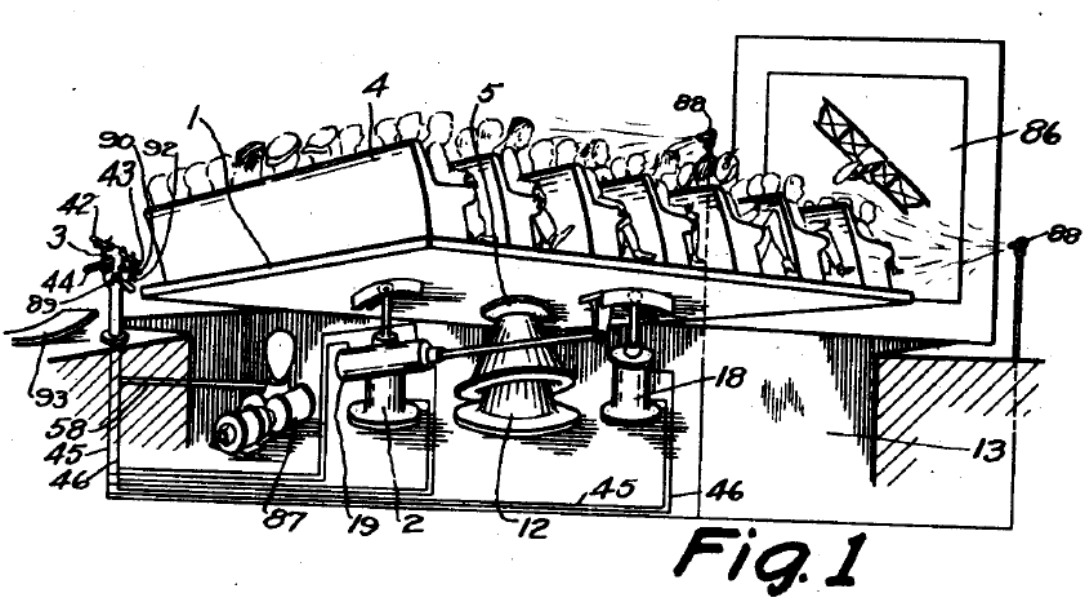

Figure 1.3: Amusement device (US patent NO. 1789680) [38]

The first parallel robot concept did not come out until 1940. It was a five-bar parallel manipulator from W. L. G. Pollard Jr, which was a painting machine idea for the vehicle industry. Not only the mechanical parts were shown in US patent 2213108 [37], but also the control method. The manipulator is shown in Figure 1.4:

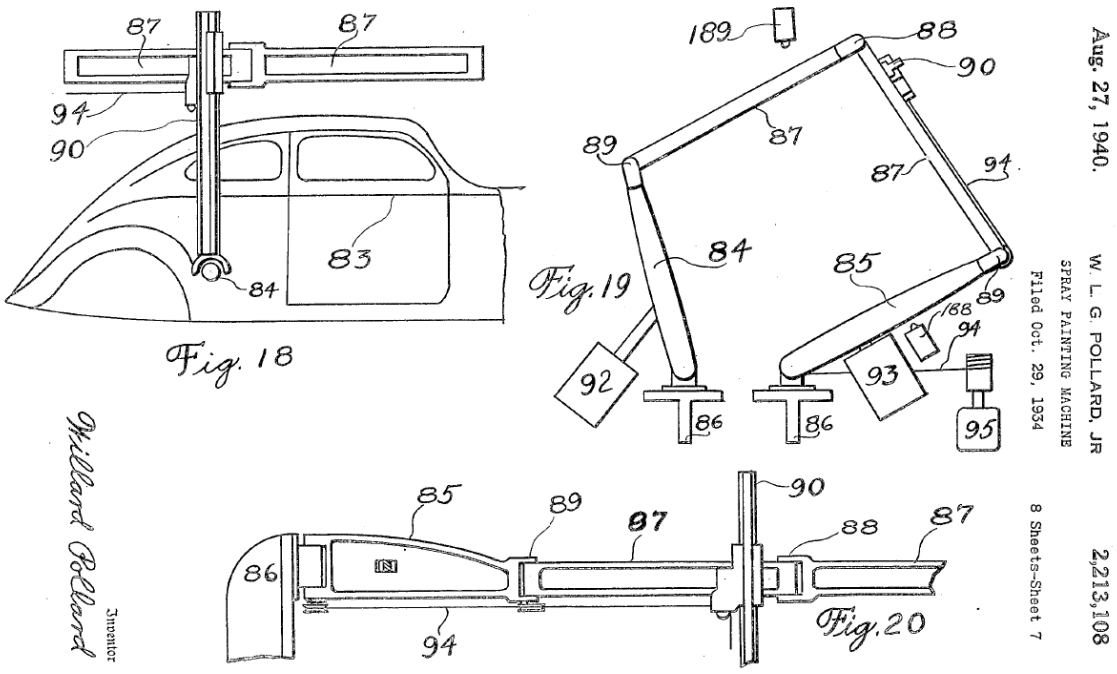

Figure 1.4: The first industry parallel robot concept (US patent NO. 2213108) [37]

In 1942, W. L. V. Pollard made an improvement over the previous manipulator. In US patent 2286571 [36], he designed a parallel robot to paint a vehicle. The image of it is shown in Figure 1.5. This manipulator had five degrees of freedom. The position of the end-effector was controlled by three motors fixed on the base.

H. A. Roselund invented a spray gun control device in 1944 with a serial mechanism (US patent NO. 2344108) [46]. This device was controlled by Mr. Pollard's method in US patent

2213108. Unfortunately, Mr. Pollard's parallel manipulator design was never applied into industry.

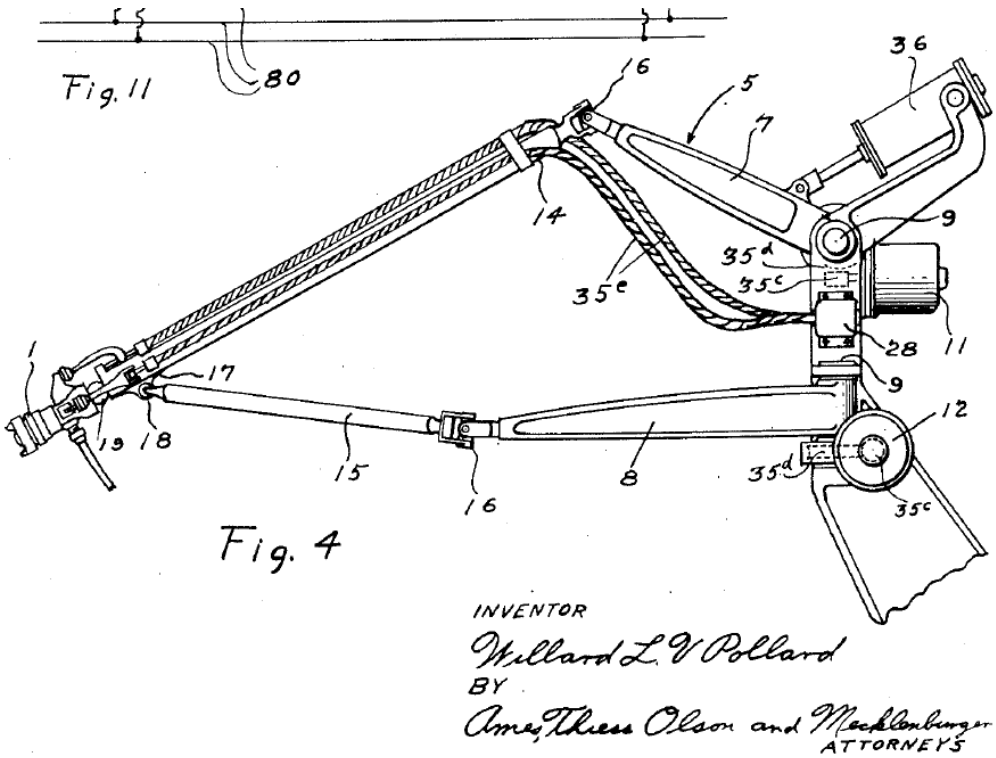

Figure 1.5: The improved painting device by W. L. V. Pollard (US patent NO. 2286571) [36]

1.1.4 The Application of Parallel Robot

As discussed in the previous section, the first parallel robot concept did not come before the 1930s. In this section, two types of parallel manipulators are going to be introduced which are applied in today's industry field: Delta robot and Stewart-Gough robot.

After the invention by Pollard, Dr. Eric Gough developed the first parallel robot for tire testing in 1947 [42]; and it was first built in 1954. As shown in Figure 1.6, there are six linear actuator connected to a platform through six ball-and-socket joints, respectively.

Changing the lengths of these actuators could alternate the position and orientation of the moving platform, containing the tested wheel.

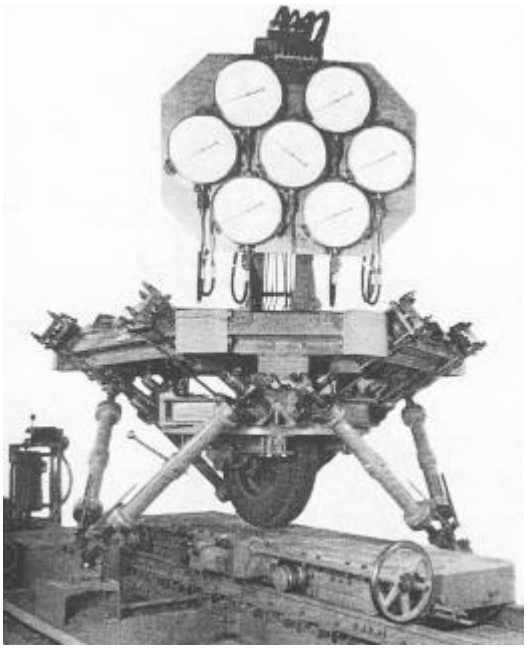

Figure 1.6: Gough platform

With different loadings applied on the tire, people could conduct wear and tear tests on tires with this parallel mechanism. It was first called the “octahedral hexapod”.

In 1965, D. Stewart published his famous paper about the original design of a parallel mechanism for pilot training simulation [41]. In his paper, he presented a spatial triangle, which had six degrees of freedom, which were controlled by six linear actuators respectively. Pilots could sit on the platform during training. These mechanisms have been named the “Stewart Platform” or “Gough/Stewart Platform”.

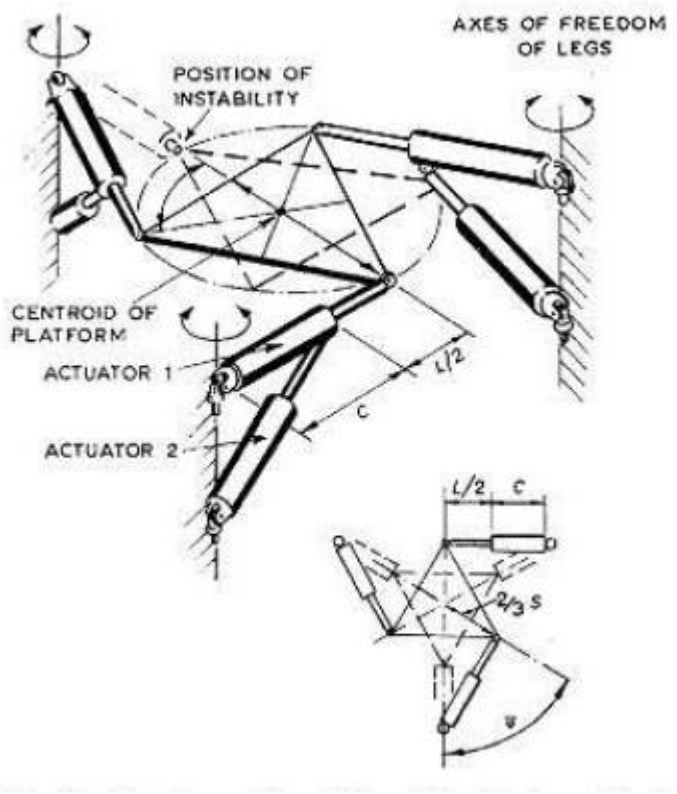

Figure 1.7: Original Stewart platform design

The original platform design is shown in Figure 1.7. This is the real Stewart Platform. There are three legs supporting the platform on the top. Each leg has two cylinders generating linear motion to control the end-effector. Even though the original design was different from the current Stewart-Gough Platform, D. Stewart conducted the first flight simulation machine design with an illustrious impact for future researchers and engineers.

Many reviewers, including Dr. Gough himself, suggested Stewart use the hexapod configuration which predicted the mechanism in flight simulation machine accurately. At the end of that paper, he also mentioned that it would be possible that the simulator could

be equipped with the same mechanism as Dr. Gough's tire testing machine. Today, because of the high accuracy and high rigidity, parallel manipulators are widely applied in the field of motion simulations.

Figure 1.8: Flight simulator today

The first Delta Robot prototype was built in 1980s by Dr. Reymond Clavel and his research team at École Polytechnique Fédérale de Lausanne (EPFL, Switzerland). The Delta Robot was patented in 1990; U. S. patent NO. is 4976582 [40]. There are three link chains connected to a mobile platform within Delta Robot, which are actuated by three rotational actuators, respectively. In the center of the manipulator, there is a telescopic arm connecting the end-effector and base, which is supposed to bring an orientation to the moving platform. The model is shown in Figure 1.9.

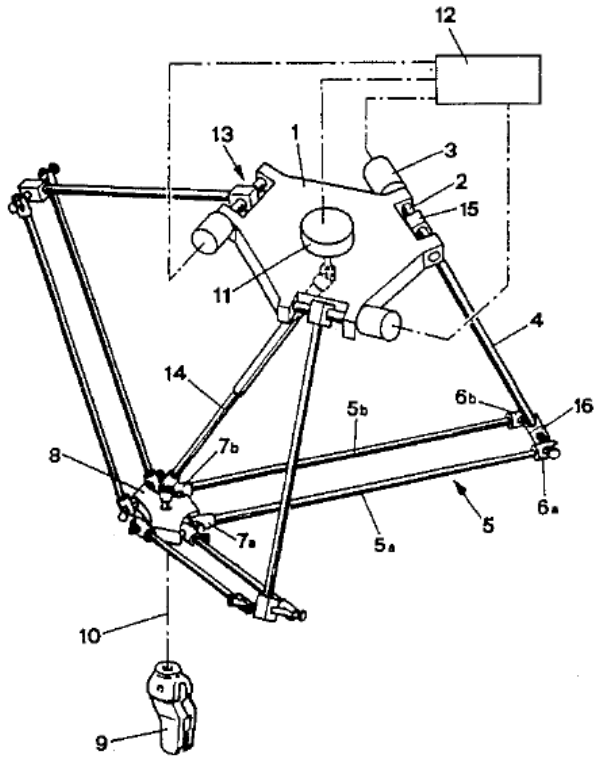

Figure 1.9: Original Delta Robot design (U. S. patent NO. 4976582) [40]

Because of the high speed and acceleration, the Delta Robot is widely applied in industry today, from packaging to the pharmaceutical industry.

Recently, Delta Robot played a fascinating role in the field of 3D printing. Since 2012, when the first delta 3D printer (Rostock) came out in USA, numerous companies have been putting effort into that field.

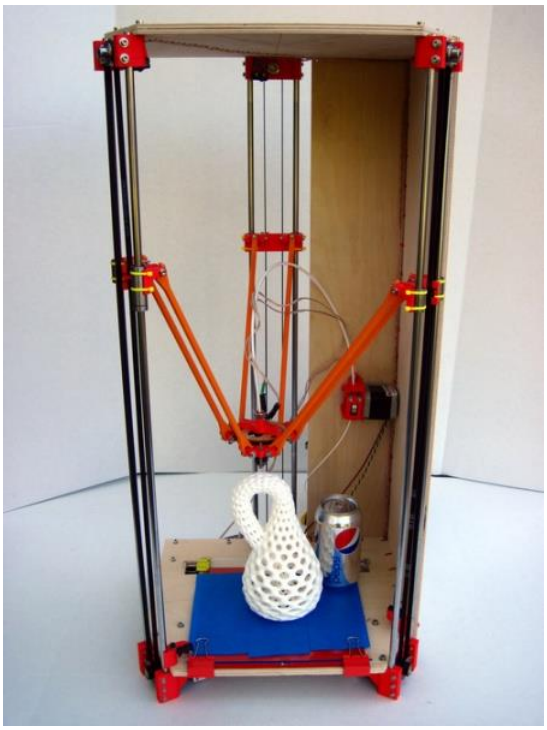

Figure 1.10: Delta 3D printer

1.2 Break Down of Chapters

Chapter 1: Introduction about the development of robotics, along with the recent research project about planar parallel manipulator.

Chapter 2: Describe the project of this research. Along with the methodology to use.

Chapter 3: Kinematic analysis for bond graph, illustrate the procedure to obtain determinant of Jacobian matrix and DSI index. Accompanied by the dimension of each part.

Chapter 4: Kinematic analysis for virtual work, which is a method different from the previous one.

Chapter 5: Dynamic analysis, including bond graph modeling and virtual work principle.

Chapter 6: Comparison. Compare the dynamic and kinematic results from bond graph and the virtual work principle.

Chapter 7: Robot hardware design, which introduces the Solidworks design and electrical hardware design of the manipulator.

Chapter 8: Discussion and conclusion.

Chapter 2

State of the Art

According to different mechanisms, parallel manipulators could be divided into three categories: planar, spherical, and spatial. As the 3-RPR planar parallel manipulator (PPM) is a part of planar parallel robots, several recent kinds of planar parallel manipulator in this chapter will be introduced.

Unfortunately, parallel robots with planar parallel mechanisms have not been applied into the industry so far. However, researchers have made a gradual effort to improve the dynamic performance of planar parallel robots in recent years.

2.1 Variable Actuated Mechanism

The manipulator will obtain an inferior performance when it reaches a place near the singularity curve within the workspace. In order to improve the design quality, N. Rakotomanga, D. Chablat, and S. Caro developed a planar parallel manipulator with variable actuated mechanism in 2008 [32]. This is a reconfigurable robot.

Figure 2.1: Variable actuated mechanism (courtesy of "Institut de Recherche en Cybernétique de Nantes" (IRCCyN))

As shown in Figure 1.11, the researchers proposed an extrapolation of a 3-RRR PPM. There are two motors in each limb. It is possible to choose a different actuated model according to certain positions and orientations of the moving platform which is located in the middle. With that mechanism, the manipulator could obtain the best performance with a suitable actuate mode.

2.2 Variable Geometry Mechanism

Despite the variable actuated mechanism, another option for researchers that is widely applied to improve manipulators' performance is the redundant mechanism. This means that the manipulators could be actuated by an additional limb compared with the classical configuration.

In 2009, Jens Kotlarski, Houssem Abdellatif, Tobias Ortmaier, and Bodo Heimann developed a PPM with a redundant mechanism. As shown in Figure 1.12, the manipulator has an additional prismatic (P) joint on the right hand side. It is called 3 (P)RRR PPM, which improves the dynamic performance of a classical 3 RRR PPM.

Once the moving platform is close to a singularity loci, the prismatic joint could reach a certain place to alter the singularity curve. As a result, the manipulator could obtain the best performance with a certain kinematical configuration. The image below comes from the website of "Institute of Mechatronic Systems, Leibniz Universit¨at Hannover". This solution has not been selected.

Figure 2.2: Redundant kinematic mechanism

For the justification, the goal of this thesis is to study a purely parallel manipulator and to further knowledge on the application of the 3-RPR. We did not deal with redundant mechanism. This adds important complexity, often leading to unsolvable kinematic problems.

2.3 Device for the Movement and Orientation of an Object in Space and Use Thereof in Rapid Machining

In August 2011, Dr. Damien Chablat and Philippe Wenger invented a rapid machining device with parallel mechanism [49]. The object of the invention is thus to provide a device for movement and orientation of an object in space comprising an object support carried by a movable intermediate support connected to a fixed frame by articulated connection means, and having characteristics suitable for use such as envisaged above and in particular in the case of high speed machining.

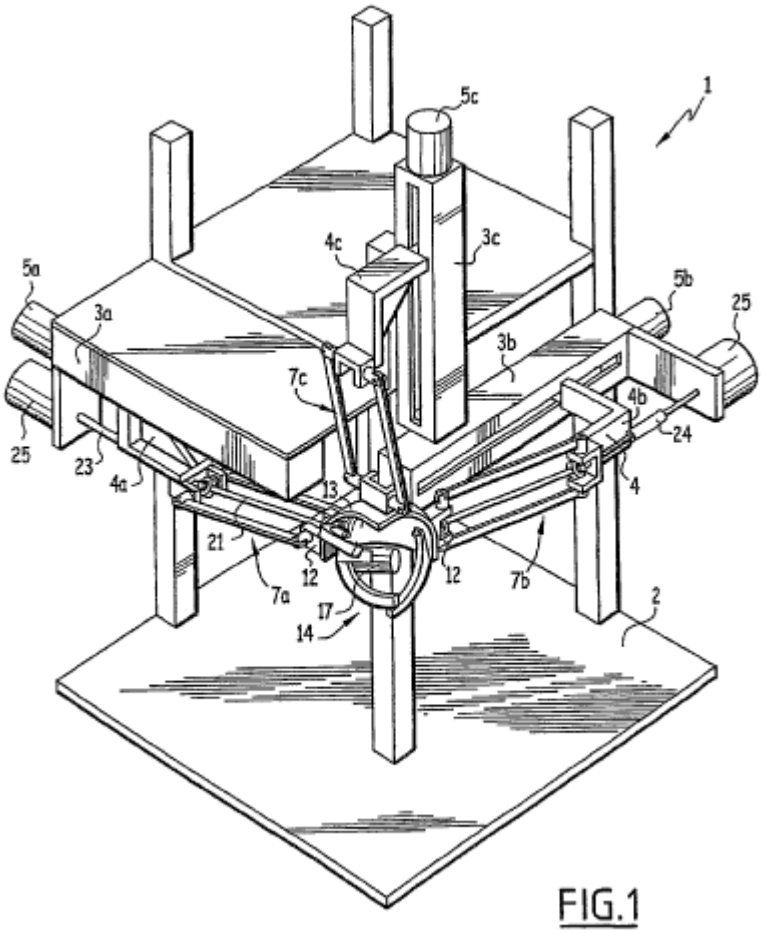

Figure 2.3: The device figure (US Patent 7997161 B2)

Until now, such devices and in particular milling tools with digital control used in industry used a construction of serial type, whose axes of movement and the corresponding motor means are mounted in series. Such machines using constructions of the serial type are less adapted to the needs of high speed machining, because of their high inertia, an upstream axle of the machine having to support a downstream axle and its motor means. With this device, the milling machine tool could have a less inertia and a higher speed and a higher accuracy.

2.4 Planar Parallel 3-RPR Manipulator

In 1999, Robert L. Williams II and Atul R. Joshi built a 3-RPR PPM with PID controlors [50]. The paper described the design, construction, and control of a planar three DOFs in parallel-actuated manipulator at Ohio University. In the paper, the authors introduced the workspace analysis of the 3-RPR PPM. Furthermore, they introduced the hardware design and the controllor design. The overall image is shown in Figure 2.4.

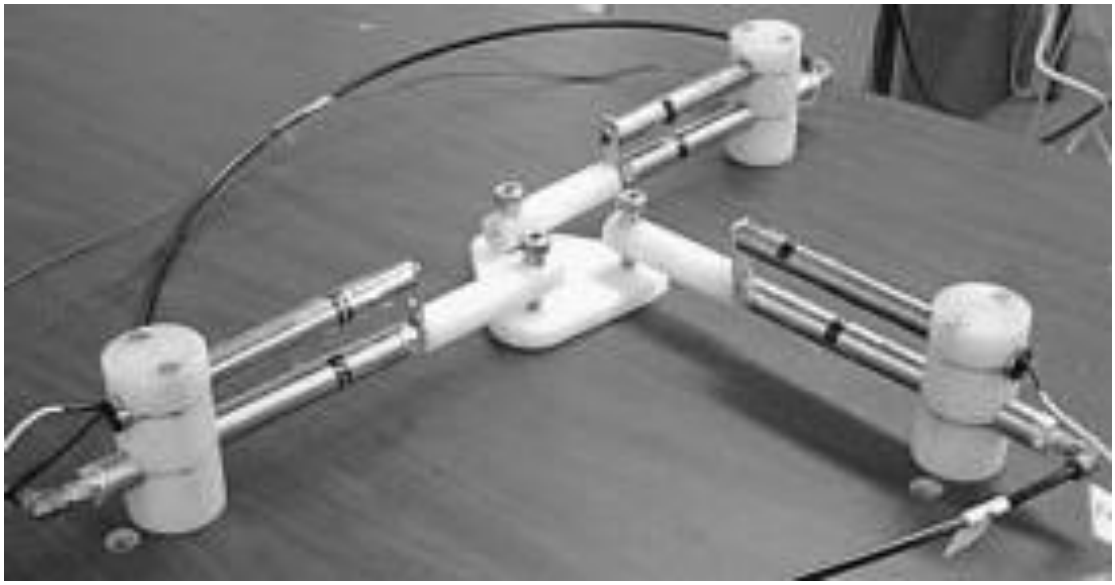

Figure 2.4: 3-RPR PPM from Robert in 1999

The manipulator was driven by three air cylinders as three linear actuators. And the three motors were controlled by three PID control loops respectively. What they built was a classical 3-RPR PPM. The platform moved inside the fixed joints area.

With the development of computer based calculation and analysis, I could conduct more kinds of analysis to improve the configuration of the manipulator present. And the manipulator has a higher performance than the classical one, according to the kinematic analysis. The detailed objectives of this master project are shown in Chapter 3.

Chapter 3

Research Project Presentation

3.1 The General Task

In this paper of a 3-R<u>P</u>R PPM, the objective of our research is to proceed with the mechanical design of a robotic manipulator; to study how to improve the performance of the 3-R<u>P</u>R PPM. The mechanical design of this robotic manipulator will be conducted. To construct the 3-R<u>P</u>R parallel manipulator, assembling all the parts in the laboratory, including the controller, the actuator, the moving platform and the frame.

A 3-R<u>P</u>R parallel robot is a kind of planar manipulators. The tripod consists of three serial links connected in parallel to the moving platform, each mechanic chain is identified as "R<u>P</u>R". The "R" stands for a passive revolute joint; the "P" represents a prismatic joint, which is actuated in this case. This is the reason that the letter "P" is underlined in the abbreviation "R<u>P</u>R". The moving platform moves within the horizontal (XY) plane.

Figure 3.1 shows a diagram of a general 3-R<u>P</u>R manipulator. The lengths of the segments A_iB_i, denoted by L_i, can be varied within the permissible ranges of the prismatic actuators L_{imin} and L_{imax}. As a manipulator with three degrees of freedom (DOF), the moving platform moves in the X and Y directions of the global reference frame, the third DOF is the rotation about an axis, which is in parallel with the global Z direction. Three linear

actuators control the pose (position and orientation) of the manipulator. They are expressed by the center of the moving platform: C_X and C_Y, and the platform's orientation: Φ.

In the general model, the positions of the fixed joints A1, A2, A3 and the platform joints B1, B2, B3 correspond to the configuration and can be modified. Several researchers have studied the model with the configuration that the mobile platform moves inside the fixed joints area. Up the author's knowledge, none has studied the impact of sending it outside the space defined by the fixed joints area.

In our study, we are going to study a purely parallel manipulator and to especially further knowledge on the planar ones where the 3-RPR has been selected.

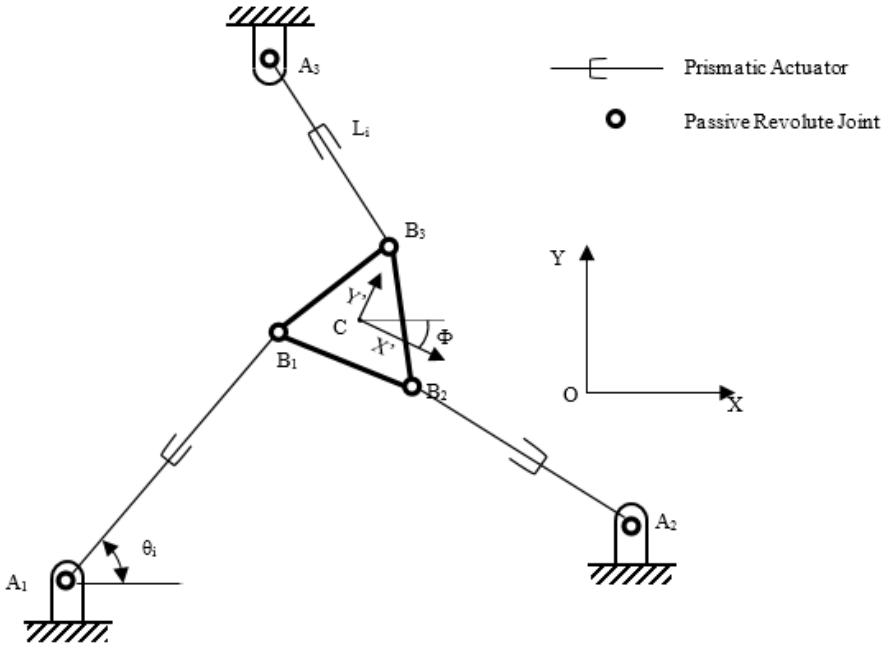

Figure 3.1: A sketch of 3-RPR PPM

In the specific case, I assume the fixed joints can be moved to any positions on the platform. As a result, the robot has to be designed reconfigurable. In this thesis, the term "reconfigurable" means that some parts of the manipulator could be replaced by others, and the configuration of the manipulator could be revised, meaning changing the positions of three fixed joints (A_1, A_2 and A_3). In order to compare the parameters of typical linear actuator and the new high performance linear actuator designed in the High Performance Robotics Laboratory, it is essential to make some of the manipulators reconfigurable by allowing replacement of the actuators. The detailed description of that will be illustrated in the "Objective" section of this chapter.

The overall manipulator-assembling graph is shown in Figure 3.2. The three actuated links distributed within three different levels in the graph. There are three fixed revolute joints, which are attached to an aluminum frame. The linear actuator bracket and high performance linear actuator will have the same dimension for the connector on the revolute joint. That makes the manipulator could be a reconfigurable one, which could obtain actuated force from a classic linear actuator or a high performance actuator "X".

The 'X' linear actuator is a newly developed actuator designed at the High Performance Laboratory based on the application of scissors in networks, reference Toufiq's thesis [51]. These actuators can reach up to 15 g accelerations.

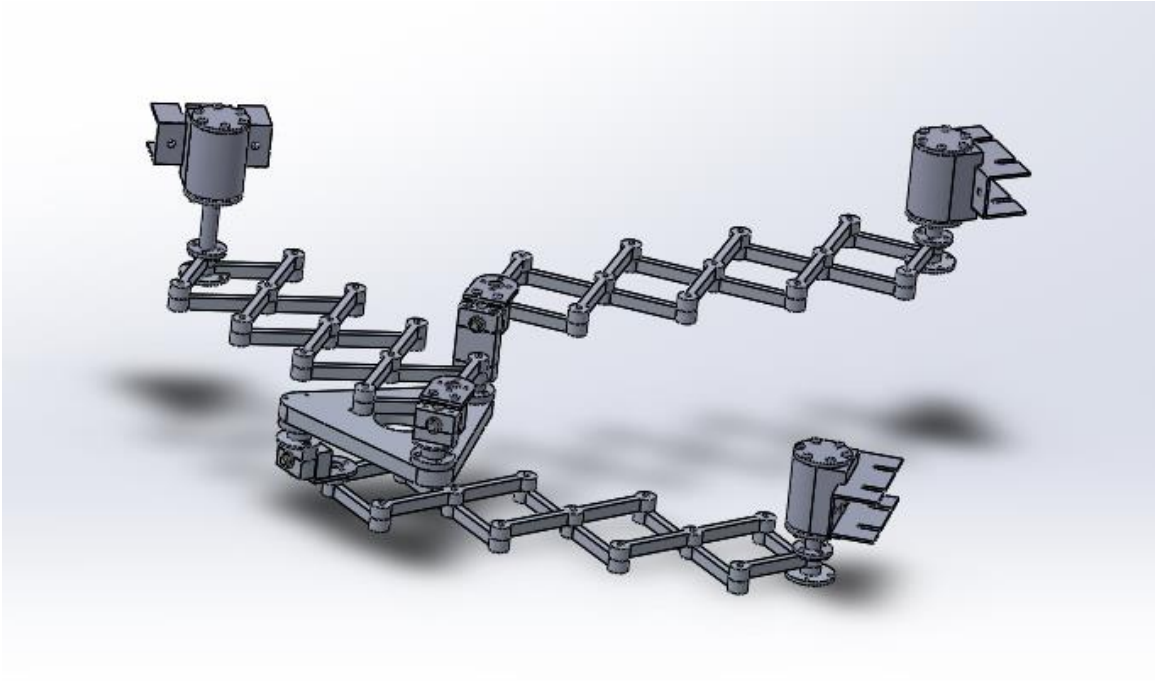

Figure 3.2: Overall manipulator assembling of the 3-RXR

3.2 Constraints

Firstly, to find some high speed and affordable linear actuators is our target, where the actuators being affordable and with improved performance. The models introduced in the section 7.1.3 of Chapter 7 have proven prohibitively costly. Furthermore, it is also difficult to find a linear actuator with 600 mm stroke with encoder on the market. The price exceed our budget as well.

Secondly, the friction model was not included in the bond graph and virtual work model. The friction models are difficult to render realistic and usually add significant complexity to the models. In this thesis, we examine the bond graph modeling approach against the virtual work one. We will try to determine how accurate the bond graph tool is.

Additionally, the configuration of the manipulator should be able to be changed, which would be like the reconfigurable PPM in reference [31]. As discussed in the section 3.1, the positions of three fixed joints could be adjusted before the manipulator is utilized; while during a task, the fixed joints would remain in the start position on the frame.

Eventually, the manipulator would be designed to be two in one: the moving platform could be moved by three classic linear actuators; furthermore, the three linear actuators could be replaced by three high performance linear actuators provided by another student in our laboratory, which are controlled to be within the new generation of actuators.

3.3 Specifications

The height of the high performance actuator is set to 30 mm, a 42 mm height difference between two connect parts has to be applied. The height of the moving platform is 20 mm. The distance in height between the bottom connector and the top one is 208 mm. The maximum displacement of each actuator is 600 mm. The dimension of the fixed frame and the detailed drawings of some important parts will be described in Chapter 7.

3.4 Objective of the Thesis

3.4.1 The Main Goal of the Thesis

In this study, the main objective of our research is to accomplish the mechanical design of one 3-RPR robot, along with the electronic hardware selection. The robot design will allow integration of a new generation of linear actuator, as well as three classic ones. The robot will be constructed.

3.4.2 The Detailed Objective of the Thesis

1. Implement the kinematic analysis of the manipulator, including the workspace analysis, determinant of inverse Jacobian analysis and the manipulability analysis.

2. Determine the geometric parameters of the manipulator to obtain a better performance, based on the kinematic analysis.

3. Design the frame. The frame should meet the reconfigurable requirements, on which the fixed joints position could be changed. These could be modified for a different purpose.

4. Design the moving platform based on the kinematic analysis.

5. Choose the electrically driven prismatic actuator, the three identical ones have the same stroke length as the high performance linear actuator.

6. Design and assemble the joints for the moving platform and fixed platform.

7. Design and assemble the manipulator. The high performance actuator could replace the general linear actuator. That is one of the reconfigurable requirement.

8. Implement the dynamic analysis for the manipulator.

9. Select and install electrical and electronic hardware for this project. The hardware includes the micro-controller.

3.5 Methodology

In this research, the kinematic analysis for 3-RPR PPM will be conducted firstly. Then calculate the direction selective index for improving the performance of it. Furthermore, use bond graph and virtual work for dynamic analysis. As bond graph is a relevant new methodology, a comparison between both dynamic analysis results will be made. In the end, the mechanical design will be completed according to the analysis, as well as the electronic hardware design.

3.5.1 Workspace

In 1997, Merlet, Gosselin and Mouly contributed to the workspace study [16]. In the paper, they generated the workspace graphs for 4 3-RPR PPMs. They defined five types of workspace: constant orientation workspace, maximal workspace, inclusive maximal workspace, total orientation workspace and dexterous workspace. The constant orientation workspace will be calculated to optimize the manipulator configuration, because the constant orientation workspace will give a certain area with a clear boundary. In addition, it will be helpful for us to study how to improve its performance later.

In 2006, Arsenault and Boudreau generated a reliable synthesis method to optimally select the geometrical parameters of 3-RPR planar parallel manipulator [2]. In their study, they analyzed workspace error (the error between its workspace and a prescribed workspace),

dexterity and stiffness; the authors choose certain configuration parameter values, which make the PPM without singularity within the workspace, furthermore, the 3-RPR PPM has the least workspace error.

3.5.2 Singularities

In 1990, Gosselin and Angeles presented a singularity analysis method for closed-loop kinematic chains [9]. According to their research, there are three types of singularities occurring in some conditions.

In 1995, Sefrioui and Gosselin drew the singularity loci for 3-RPR PPM completely [20].

In 2003, Gosselin, Bonev and Zlatanov demonstrated a detailed study of the singular configurations of 3-DOF PPM [4]. There are ten different architectures studied in the paper, all of which are examined in a compact and systematic manner using planar screw theory. The constant orientation singularity loci of a 3-DOF PPM are obtained as well. According to the paper, there is no Type 1 (blockage) singularity of 3-RPR PPM. Furthermore, Type 2 (DOF Addition) singularity loci are those parts of the quadratic curve that are within all vertex spaces.

Recently, in June 2014, Kaloorazi, Masouleh, and Caro use interval analysis to find out the max singularity-free circle or sphere of 3-RPR PPM [3]. Compared to genetic algorithms, Interval analysis has many advantages, which are listed in the paper. However, the method

can only draw the maximal circle in the workspace without singularity, not the strict boundary of the singularity free area.

In closed-loop mechanisms, the joint-space variables are defined as $\boldsymbol{\theta}$, the Cartesian-space variables as $\mathbf{X}$.

$$\mathrm{F}(\boldsymbol{\theta}, \mathbf{X}) = 0 \tag{3.1}$$

$$\mathrm{A}\dot{\boldsymbol{X}} + B\dot{\boldsymbol{\theta}} = 0 \tag{3.2}$$

$$\mathrm{A} = \frac{\partial \mathrm{F}}{\partial \mathbf{X}} \quad B = \frac{\partial F}{\partial \boldsymbol{\theta}} \tag{3.3}$$

The first type of singularity, the forward singularity, occurs when determinant of A is equal to 0; on the other hand, the inverse singularity exists when det(B) = 0. The third kind of singularity is of a slightly different nature than the first two since it requires conditions on the linkage parameters, which occurs when both A and B become singular simultaneously. Reference [9] demonstrates the singularity analysis procedure for a 3-RRR PPM, which is the first singularity study about planar parallel manipulators.

In this study, the determinant mapping will be conducted according to the Jacobian matrix of the manipulator. After the surface plot is accomplished, it would be the way to identify singularity locus proximity and choose a certain configuration accordingly.

3.5.3 Direction Selective Index (DSI)

In 2011, G Boschetti, R Rosa., and A Trevisani wrote a paper which mentioned an index for robot performance evaluation [26]. In their dissertation, they conducted a DSI analysis on the Delta robot.

This index represents the mobility in a certain direction. For instance, the manipulator can move effortlessly where the DSI value is high; the position is far away from the singularity loci as well. In this study, it is needed to analyze this index in order to optimize the configuration of the manipulator.

3.5.4 Dynamic Analysis

In 2009, Stefan Staicu presented 2 papers about the dynamic analysis of two kinds of PPMs; one is about the 3-PRR [21], the other one is about the 3-RPR [22]. Besides the inverse dynamic analysis with virtual work for the 3-PRR, he also studied the power requirements when the manipulator was actuated by revolute or prismatic joints.

In the year of 2014, Firoozabadi, Ebrahimi and Amirian did the dynamic analysis of 3-RPR PPM with flexible links [8]. In their study, the movement of the moving platform was successfully simulated under 3 different end-effector loading conditions: a constant external force, a constant external torque and harmonic forces.

After comparing the principles of Newton-Euler, Lagrange, and virtual work, it is decided to use the virtual work principle as it needs less variables and it is based on the kinematic analysis of the manipulator. Virtual work also eliminates the constraint forces and moments between different links. Overall, it is more efficient and suitable for parallel manipulator dynamic analysis [23]. In this chapter, the research project has been introduced, including the task, objectives and methodologies. In the next chapter, the project will be started with the kinematic analysis.

Chapter 4

Kinematic Analysis with the Vectorial Approach

In this chapter, the kinematic analysis will be proceed for 3-RPR PPM using the vectorial approach, including the workspace analysis, Jacobian calculations and the DSI analysis. In the end of this chapter, the DSI analysis will point towards the optimal configuration and the platform size of the manipulator. In the Chapter 6, the bond graph simulation method will be based on the derived kinematics models of this chapter.

4.1 Inverse Kinematic Problem (IKP)

The relation giving the actuated joint coordinates for a given pose of the end-effector is called the inverse kinematics [35]. In Figure 4.1, a fixed reference frame OXY is defined, which is attached to the manipulator's base; and a mobile reference frame CX'Y' which is attached to the manipulator's moving platform. Henceforth, quantities expressed in the mobile reference frame will be denoted by the 'symbol.

In Figure 4.1, $A_1A_2A_3$ constitutes an equilateral triangle, so is the triangle defined by $B_1B_2B_3$. The distance between A_1A_2 is 900 mm. The distance between B_1B_2 is 200 mm, which is called "L_{MP}" in this paper. "L_{MP}" and the positions of Ai and Bi become configuration parameters. The configuration in Figure 4.1 is called classic configuration in this dissertation.

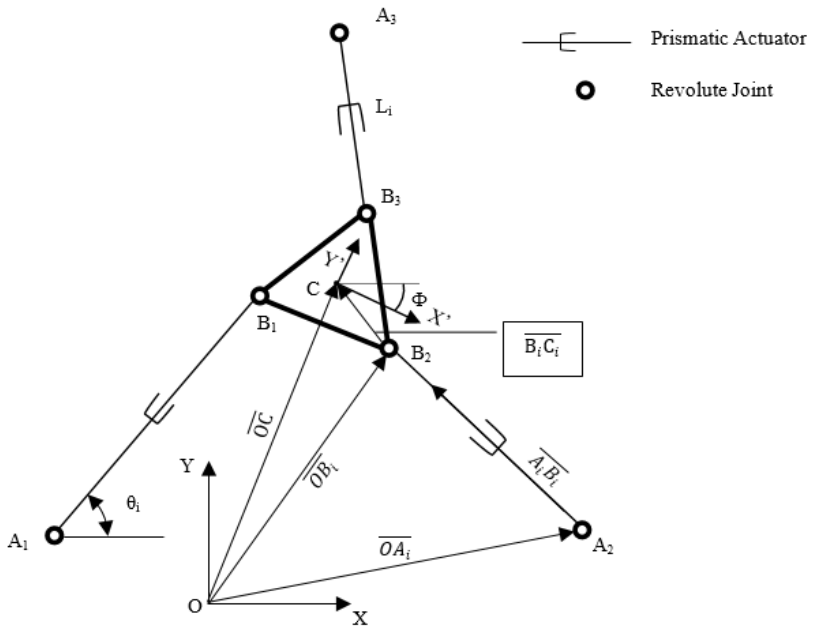

Figure 4.1: A sketch of 3-RPR PPM with classic configuration

There are three kinematic chains attached to the moving platform. Consequently, in the inverse kinematic equations, the position and orientation of moving platform compose the inputs ("X" in the Equation: $\mathrm{F(L, X)} = 0$): x, y, Φ; the outputs are three links' lengths ("L" in the Equation: $\mathrm{F(L, X)} = 0$), where $L_i = |A_iB_i|$(i ranges from 1 to 3).

$$\overline{OC} = \overline{OA_i} + \overline{A_iB_i} + \overline{B_iC} \tag{4.1}$$

$$\overline{A_iB_i} = -\overline{OA_i} + \overline{OC} + \overline{CB_i} \tag{4.2}$$

$$\overline{A_iB_i} = -\overline{OA_i} + \overline{OB_i} \tag{4.3}$$

On the right side of Equation 4.2, $\overline{OA_i}$ represents the position of point A_i in the global reference frame; $\overline{OC}$ represents the position of point C in the global reference frame; $\overline{CB_i}$ is the position vector between point B_i and C in the global reference frame. Where

$$\overline{CB_i} = R * \overline{CB_i}' \tag{4.4}$$

$$R = \begin{bmatrix} \cos(\Phi) & -\sin(\Phi) \\ \sin(\Phi) & \cos(\Phi) \end{bmatrix} \tag{4.5}$$

The vector "$\overline{CB_i}'$" is the position vector, which shows the position of point B_i according to the point C in body-fixed reference frame X'Y'. Then the rotational matrix R is multiplied with this vector, transfering the position from body-fixed coordinates to global coordinates. As there are two vectors in equation 4.3, firstly, the expressions of the vector $\overline{OB_i}$ have to be calculated. The Equations 4.6~4.8 come from the calculation in Table 4.1, which are based on the rotational matrix and the position of the moving platform:

Table 4.1: Equations Based on Rotational Matrix

	Equations
Link 1	$\begin{bmatrix} B_{1x} \\ B_{1y} \end{bmatrix} = \begin{bmatrix} x \\ y \end{bmatrix} + \begin{bmatrix} \cos(\Phi) & -\sin(\Phi) \\ \sin(\Phi) & \cos(\Phi) \end{bmatrix} \begin{bmatrix} -L_{MP}\cos(\pi/6)/\sqrt{3} \\ -L_{MP}\sin(\pi/6)/\sqrt{3} \end{bmatrix}$
Link 2	$\begin{bmatrix} B_{2x} \\ B_{2y} \end{bmatrix} = \begin{bmatrix} x \\ y \end{bmatrix} + \begin{bmatrix} \cos(\Phi) & -\sin(\Phi) \\ \sin(\Phi) & \cos(\Phi) \end{bmatrix} \begin{bmatrix} L_{MP}\cos(\pi/6)/\sqrt{3} \\ L_{MP}\sin(\pi/6)/\sqrt{3} \end{bmatrix}$
Link 3	$\begin{bmatrix} B_{3x} \\ B_{3y} \end{bmatrix} = \begin{bmatrix} x \\ y \end{bmatrix} + \begin{bmatrix} \cos(\Phi) & -\sin(\Phi) \\ \sin(\Phi) & \cos(\Phi) \end{bmatrix} \begin{bmatrix} 0 \\ L_{MP}/\sqrt{3} \end{bmatrix}$

$$\begin{bmatrix} B_{1x} \\ B_{1y} \end{bmatrix} = \begin{bmatrix} x \\ y \end{bmatrix} - \begin{bmatrix} L_{MP} * \cos(\Phi + \pi/6)/\sqrt{3} \\ L_{MP} * \sin(\Phi + \pi/6)/\sqrt{3} \end{bmatrix} \tag{4.6}$$

$$\begin{bmatrix} B_{2x} \\ B_{2y} \end{bmatrix} = \begin{bmatrix} x \\ y \end{bmatrix} - \begin{bmatrix} L_{MP} * \cos(\Phi + 5\pi/6)/\sqrt{3} \\ L_{MP} * \sin(\Phi + 5\pi/6)/\sqrt{3} \end{bmatrix} \tag{4.7}$$

$$\begin{bmatrix} B_{3x} \\ B_{3y} \end{bmatrix} = \begin{bmatrix} x \\ y \end{bmatrix} - \begin{bmatrix} L_{MP} * \cos(\Phi + 3\pi/2)/\sqrt{3} \\ L_{MP} * \sin(\Phi + 3\pi/2)/\sqrt{3} \end{bmatrix} \tag{4.8}$$

Secondly, the vector $\overline{OA_i}$ in Equation 4.3 are the configuration parameters, which are the positions of three fixed joints A_i, staying constant over the robot life span.

$$\overline{OA_i} = \begin{bmatrix} A_{ix} \\ A_{iy} \end{bmatrix} \tag{4.9}$$

As a result, the inverse kinematic equation is:

$$L_i = \sqrt{(A_{ix} - B_{ix})^2 + \left(A_{iy} - B_{iy}\right)^2} \tag{4.10}$$

4.2 Workspace Analysis

From inverse kinematic equations (4.10), the lengths of L_i actuators can be obtained. According to the selected linear actuator, the L_i length ranges from 100 mm to 600 mm. In order to map the constant orientation workspace, the orientation is set to zero degree; Matlab is used to generate the workspace analysis. The algorithm and result are shown in Figure 4.2 and 4.3.

The constant orientation workspace is more intuitive than others are, because the boundary of the workspace versus the joint space can be sketched. In Matlab, it is not possible to map workspace continually. In order to map the workspace, I needed to choose a certain number of points to separate the Cartesian Space. By tried and error, it was decided to run 200000 sets of data for a good compromise between accuracy and running time. Additionally, the Monte Carlo method for mapping was used, which improves the calculation performance relatively [44].

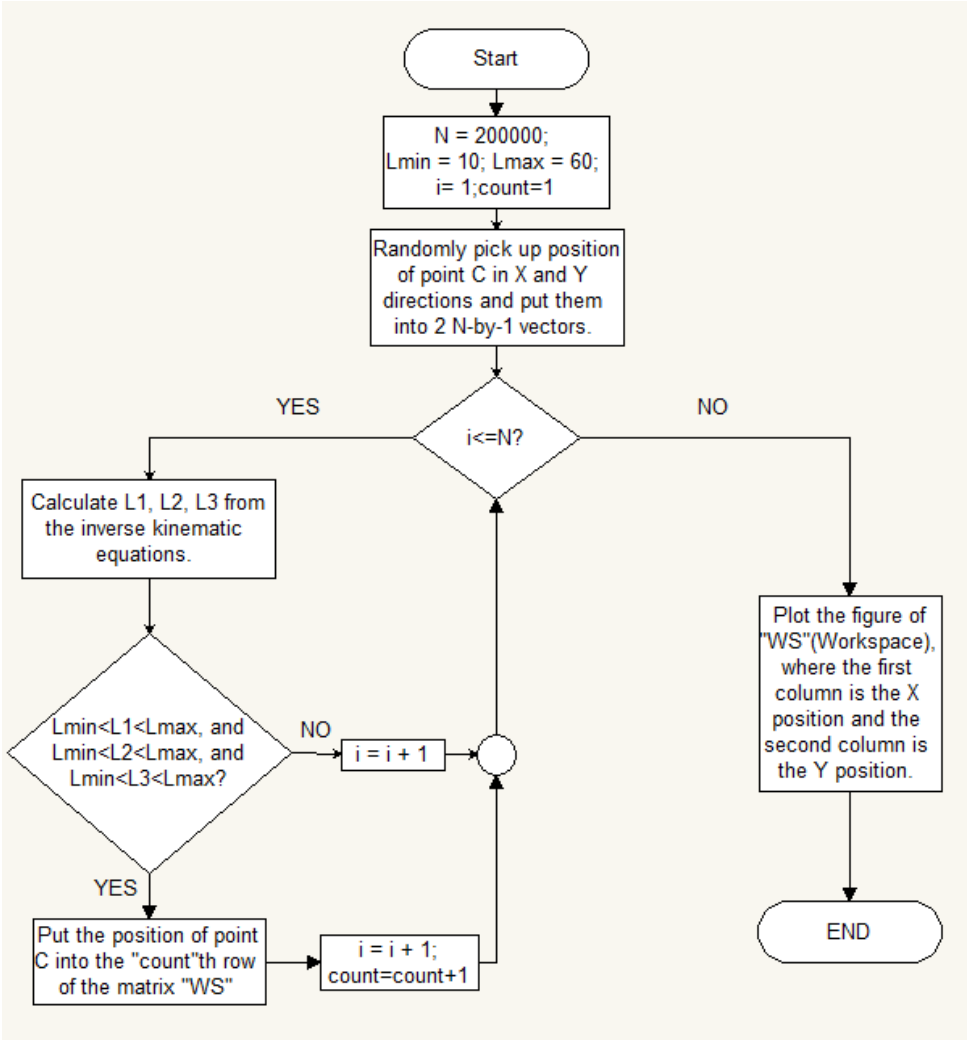

Figure 4.2: Algorithm for the workspace boundary

In the Figure 4.2, “N” sets of data were computed, where L_{min} is the minimum leg length (10 centimeters) and the L_{max} is the maximum one (60 centimeters). After finding a point which is within the workspace, put the position of that point into the matrix “WS”.

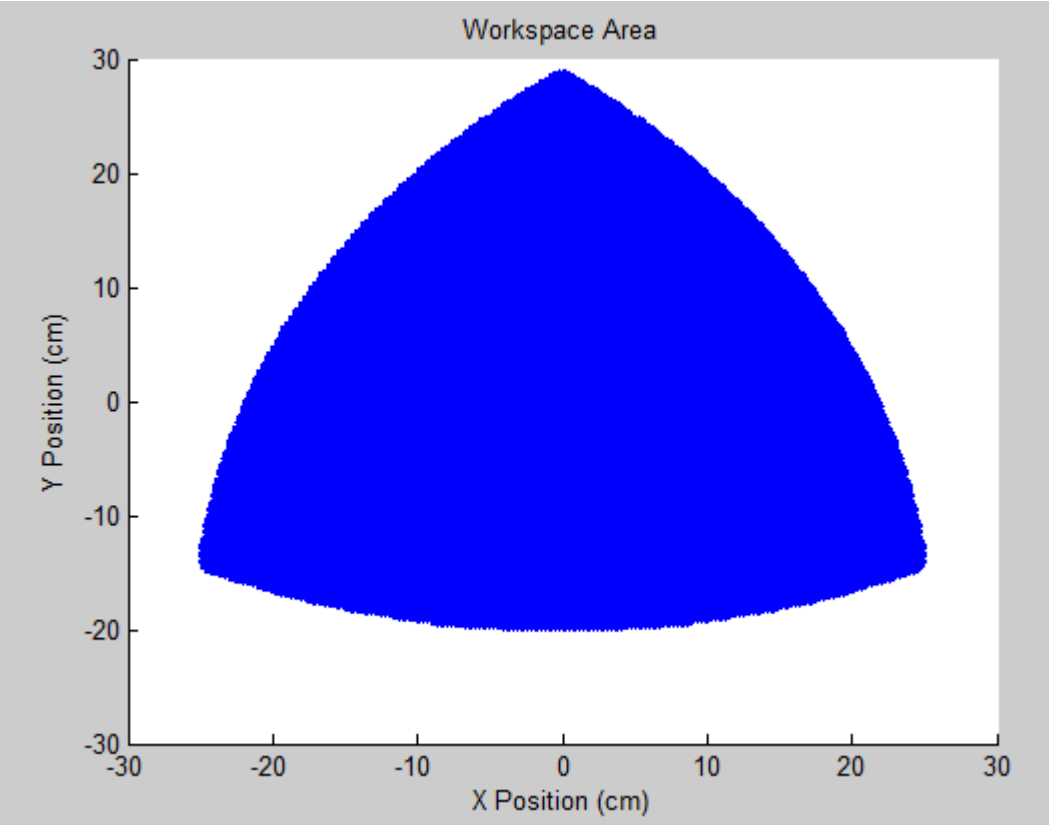

Figure 4.3: Workspace area

Figure 4.3 shows the Matlab result, where the boundary of the workspace area is the intervsection of three smooth curves. A good understanding of the workspace area of this manipulator can be obtained when it has the centered configuration.

4.3 Differential Kinematic Analysis

Firstly, calculate the angles θ_1, θ_2 and θ_3 in Figure 4.4, which are attached to three fixed points: A_1, A_2, and A_3. Then rewrite the equation 4.10 as the equation 4.12.

$$\theta_i = atan2((B_{iy} - A_{iy}), (B_{ix} - A_{ix})) \tag{4.11}$$

$$L_i^{\,2} = (B_{ix} - A_{ix})^2 + (B_{iy} - A_{iy})^2 \tag{4.12}$$

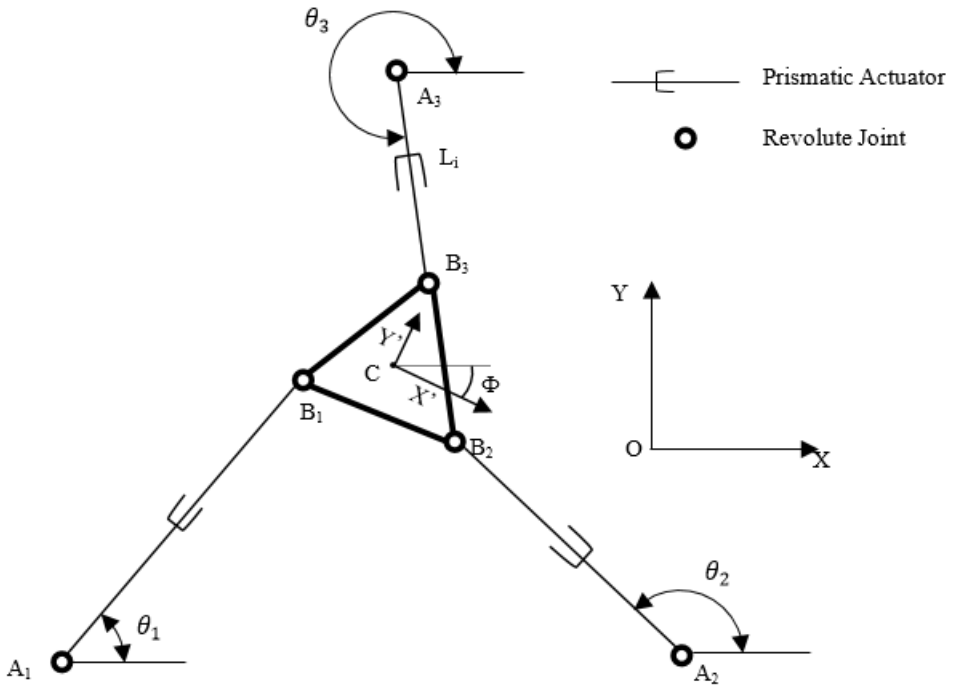

Figure 4.4: Manipulator configuration with θ_i marking

In order to solve the differential kinematic problem, the equation 4.11 is differentiated with time on both sides to obtain the equation 4.13.

$$\begin{bmatrix} L_1 & 0 & 0 \\ 0 & L_2 & 0 \\ 0 & 0 & L_3 \end{bmatrix} \begin{bmatrix} \dot{L_1} \\ \dot{L_2} \\ \dot{L_3} \end{bmatrix} = \begin{bmatrix} (\mathrm{B_{1x}} - \mathrm{A_{1x}}) & (\mathrm{B_{1y}} - \mathrm{A_{1y}}) & a13 \\ (\mathrm{B_{2x}} - \mathrm{A_{2x}}) & (\mathrm{B_{2y}} - \mathrm{A_{2y}}) & a23 \\ (\mathrm{B_{3x}} - \mathrm{A_{3x}}) & (\mathrm{B_{3y}} - \mathrm{A_{3y}}) & a33 \end{bmatrix} \begin{bmatrix} \dot{X} \\ \dot{Y} \\ \dot{\Phi} \end{bmatrix} \tag{4.13}$$

$$a13 = (L_{MP}/\sqrt{3})\left((B_{1x} - A_{1x}) \cdot sin(\,\Phi + \pi/6) - (B_{1y} - A_{1y}) \cdot cos(\,\Phi + \pi/6)\right);$$

$$a23 = (L_{MP}/\sqrt{3})\left((B_{2x} - A_{2x}) \cdot sin(\,\Phi + 5\pi/6) - (B_{2y} - A_{2y}) \cdot cos(\,\Phi + 5\pi/6)\right);$$

$$a33 = (L_{MP}/\sqrt{3})\left((B_{3x} - A_{3x}) \cdot sin(\,\Phi + 3\pi/2) - (B_{3y} - A_{3y}) \cdot cos(\,\Phi + 3\pi/2)\right);$$

According to the reference [23], the matrix on the left hand side of equation 4.13 is J_q and the other matrix is J_x. In order to obtain the inverse Jacobian matrix, use $J_q^{-1} \cdot J_x$. The result is shown in equation 4.14.

$$\begin{bmatrix} \dot{L_1} \\ \dot{L_2} \\ \dot{L_3} \end{bmatrix} = \begin{bmatrix} \cos\theta_1 & \sin\theta_1 & (L_{MP}/\sqrt{3})\sin(\Phi + \pi/6 - \theta_1) \\ \cos\theta_2 & \sin\theta_2 & (L_{MP}/\sqrt{3})\sin(\Phi + 5\pi/6 - \theta_2) \\ \cos\theta_3 & \sin\theta_3 & (L_{MP}/\sqrt{3})\sin(\Phi + 3\pi/2 - \theta_3) \end{bmatrix} \begin{bmatrix} \dot{X} \\ \dot{Y} \\ \dot{\Phi} \end{bmatrix} \quad (4.14)$$

Use Matlab to map the determinant of the Jacobian when the orientation is 0 degree. The algorithm and result are shown in Figure 4.5 and 4.6. As Matlab could only implement surface plot when the variables are distributed orthogonally, meaning the data should be distributed with the same space along the X and Y axis. As a result, it is needed to define all the points in the mapping area are void at the beginning of the simulation. If one void point is within the workspace, rewrite the void point with the determinant value at that position.

In the Figure 4.5, it is the algorithm of the determinant mapping code in Matlab, which is different from the algorithm in Figure 4.2. Use two for-loops to scan all the points within the workspace area at first. The scan step is equal to the x or y range divided by the number of runs: N.

Alike the method in section 4.2, if the point is within the workspace, put the position information into "j"th row of the matrix "WS". After that, rewrite the (i, k) element in the matrix "DET" with the determinant value from the inverse Jacobian matrix.

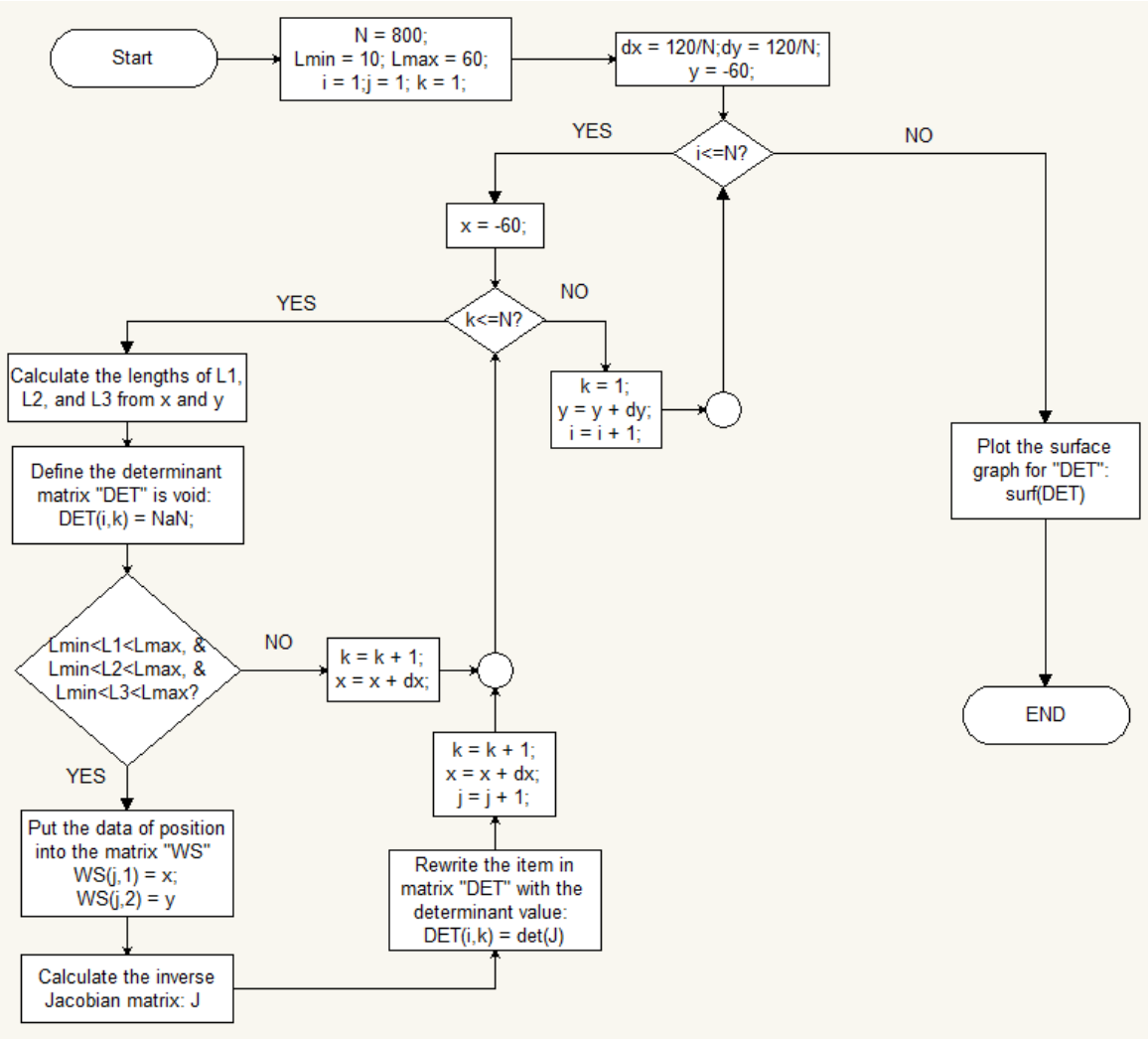

Figure 4.5: Algorithm of the Matlab code to map determinant plot

Figure 4.6 is the determinant distribution of the classic 3-RPR configuration, when the manipulator has the symmetrical configuration: three fixed joints construct an equilateral triangle and every side is in parallel with the corresponding side of moving platform.

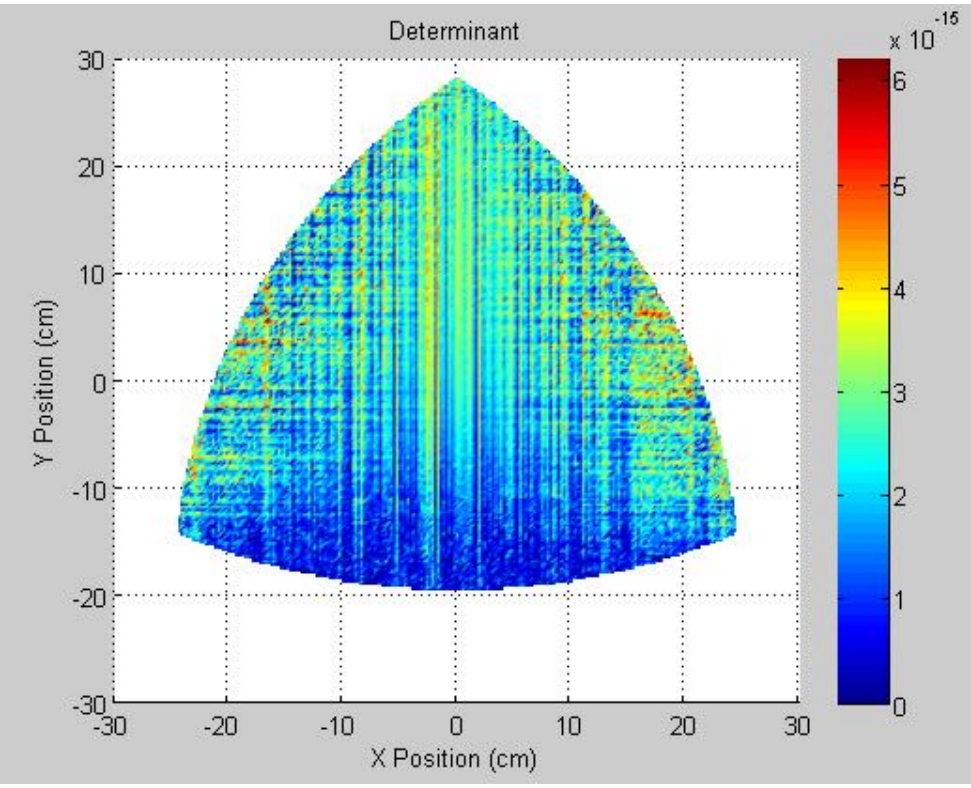

Figure 4.6: Distribution of determinant of Jacobian

From the result in Figure 4.6, it can be observed that the performance of the manipulator is poor because all the determinant values are almost zero within the workspace. This means that the robot operates very close to a singularity.

In fact, the centered platform can easily be turned by hand even when three actuators are locked. The matrix on the right hand side in Equation 4.13 is the matrix "B" in Equation 3.1. The determinant of it is shown below:

$$\det(B) = \left(-\frac{X*L_{MP}^3}{2}\right)\cos(\Phi)\sin^2(\Phi) - \left(\frac{L_{MP}^4}{6}\cos(\Phi) + \frac{Y*\sqrt{3}L_{MP}^3}{6}\right)(\cos(\Phi)-1)^2 + \left(\frac{Y*L_{MP}^3}{2} + \frac{\sqrt{3}L_{MP}^4 - X*\sqrt{3}L_{MP}^3}{6}\right)\cos(\Phi)\sin(\Phi)(\cos(\Phi)-1) - (X^2+Y^2)\frac{\sqrt{3}}{2}L_{MP}^2\sin(\Phi) + \frac{\sqrt{3}}{3}L_{MP}^4\sin(\Phi)(1-\cos(\Phi))$$

From the equation above, it can be observed that the determinant is zero when the orientation is zero, where the inverse singularity occurs. According to the reference [48], this means that the lines normal to the directions of the prismatic joints and passing through points Bi are concurrent or parallel. The moving platform would be locked in terms of translations. As a result, it is needed to choose an improved configuration for the manipulator from kinematic analysis.

4.4 Comparison among Different Configurations

4.4.1 Introduction

Assume there are four kinds of configurations to analysis. The platform moves inside the three fixed joints in two configuration. On the other hand, suppose the platform moves outside the three fixed joints in the other two. Furthermore, there are two different kinds of combination between points A_i and B_i.

In all the configurations, the platform size "L_{MP}" is equal to 200 mm.

The Configuration 1 is the centered configuration as seen in many references ([5], [8]), which is as same as the one in Figure 4.1. In the Configuration 2, three fixed joints A_1, A_2 and A_3 constitute an equilateral triangle, the side of which is 600 mm. A_1, A_2 and A_3 are not distributed symmetrically with the three revolute joints B_1, B_2 and B_3. Both Configuration 1 and Configuration 2 have the platform moving inside the fixed joints area.

Table 4.2: Four Typical Configurations to Analyze

Configuration 1	Configuration 2
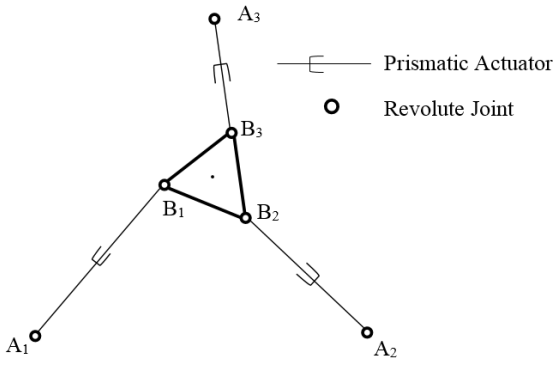	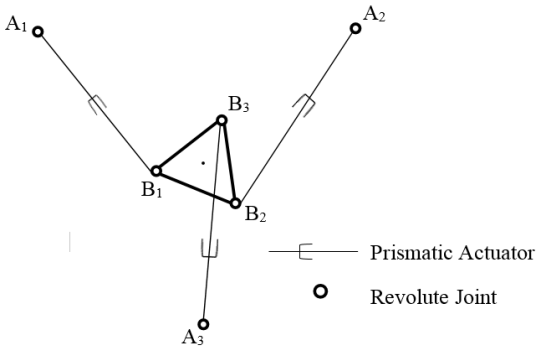
Configuration 3	**Configuration 4**
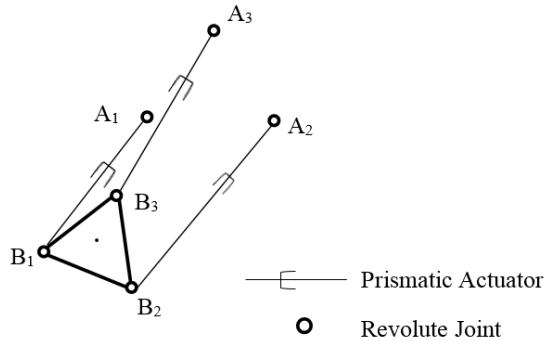	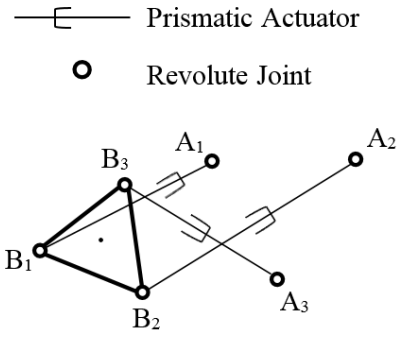

The Configuration 3 is like the centered configuration; the three fixed joints are distributed symmetrically with the three revolute joints B_1, B_2 and B_3. The difference is that the platform moving outside the fixed joints area. In the Configuration 4, the platform moves outside the fixed joints area as well. However, it is not a symmetrical configuration. In both Configuration 3 and 4, the side of equilateral triangle $A_1A_2A_3$ is equal to 300 mm.

4.4.2 Workspace Analysis

Use the Algorithm in Figure 4.2 to generate the Matlab code for workspace analysis.

Table 4.3: Workspace Analysis Result

Configuration 1	Configuration 2
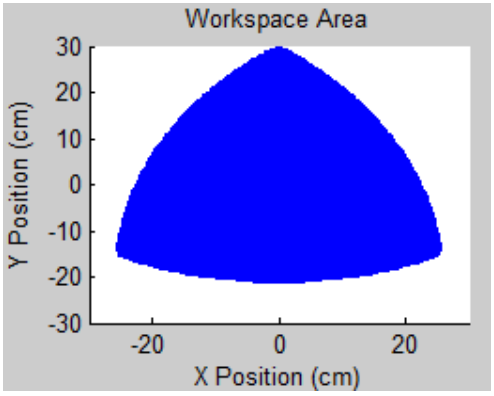	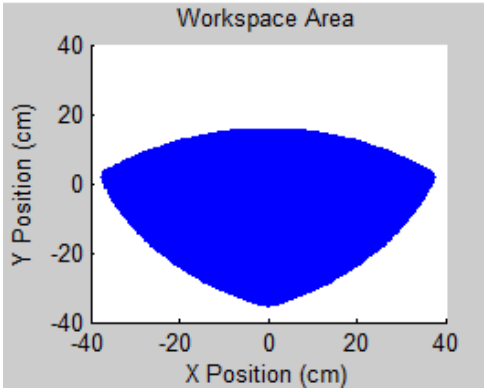
Configuration 3	**Configuration 4**
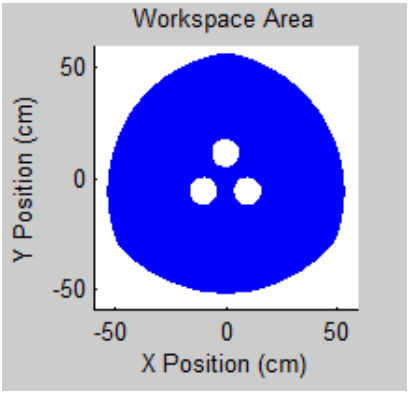	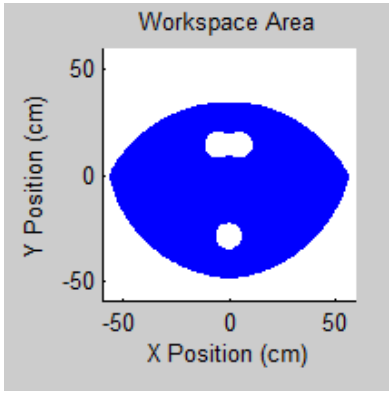

The code is similar to the one in the section 4.2. With different fixed joints' positions, the corresponding plot to each configuration are mapped in Table 4.3. The Configuration 1 has the smallest workspace area, while the Configuration 3 has the largest area. In order to choose a compromised configuration for reachable area and mobility performance, the determinant of the inverse Jacobian matrix for each case will be calculated.

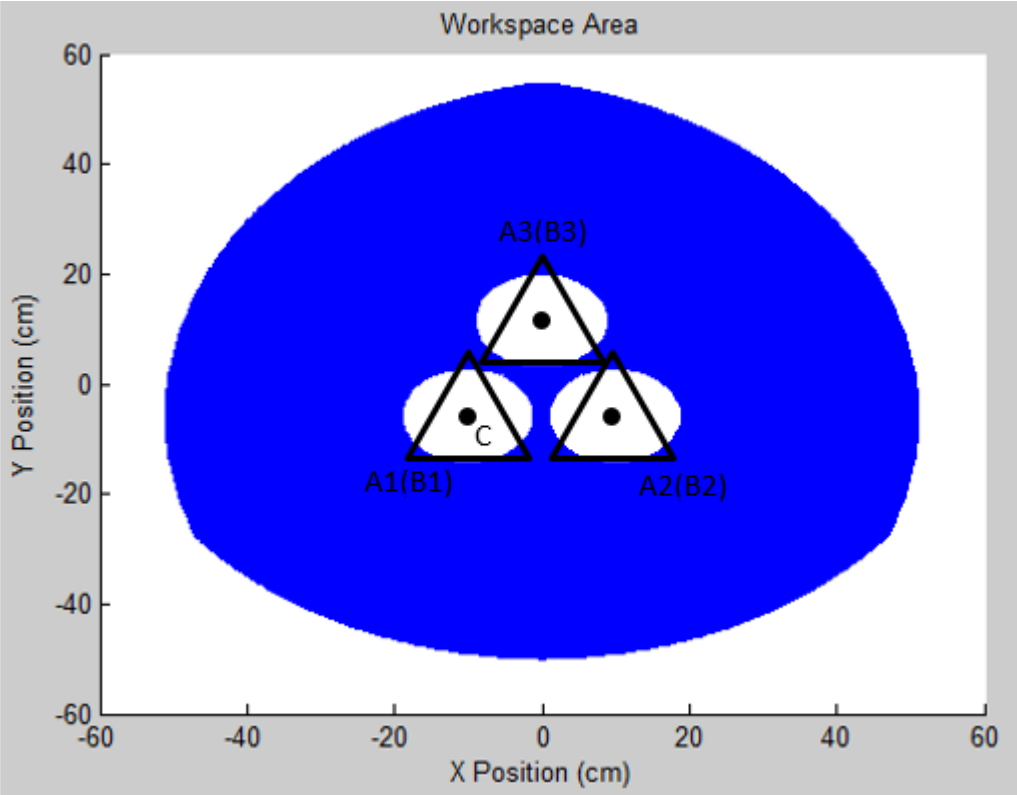

Figure 4.7: Fixed joints positions in configuration 3

Figure 4.7 is the Matlab result (excepted for the auxiliary marks). In the figure, there are three white circle within the large blue area. The point C on the platform is the center of each circle when the point B_i coincides with the point A_i. The minimum leg length of L_i determines the diameter of each circle. This is also the cause of the circles in the workspace area of the Configuration 4.

4.4.3 Differential Kinematic Analysis

Use the Algorithm in Figure 4.5 to generate the Matlab code for differential kinematic analysis.

Table 4.4: Determinant of Inverse Jacobian Matrix Analysis Result

Configuration 1	Configuration 2
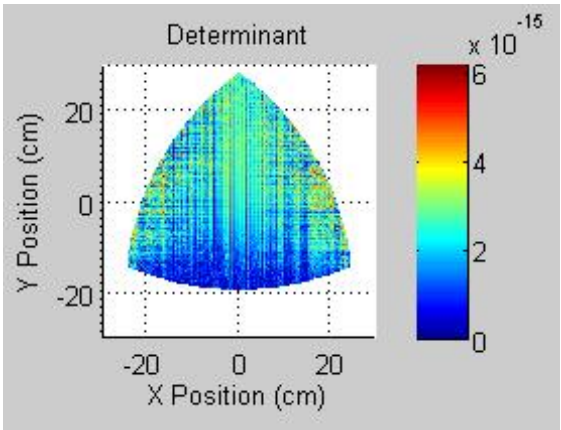	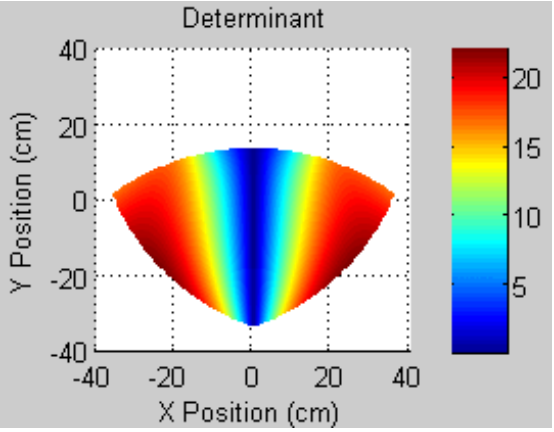
Configuration 3	**Configuration 4**
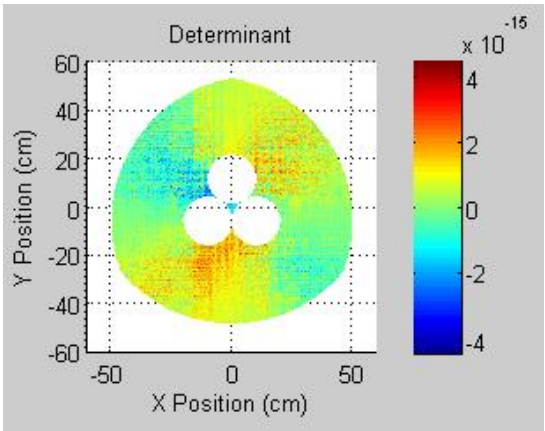	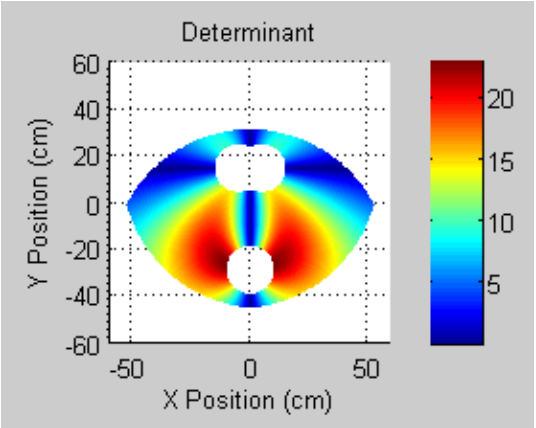

From the result in Table 4.4, a comparison of the four typical configurations can be made. When the configuration is symmetrical, the determinant is very close to zero, meaning the manipulator is close to a singularity. The workspace in the Configuration 4 is the larger than the area of the Configuration 2. Moreover, it has a favorable compromise between the overall singularity performance and workspace area. As a result, the "cross-leg" Configuration 4 is chosen as the configuration of our 3-RPR PPM.

4.5 Direction Selective Index (DSI)

According to Boschetti, G [26], the DSI provides evaluations of robot translational and rotational performances along specific directions. In this project, the DSI analysis is implemented to obtain the manipulator mobility performance in different directions: the translation along the global X direction, Y direction and rotation around an axis which is perpendicular to the X-Y plane. Based on the DSI analysis, the manipulator's mobility performance at different positions within the workspace are observed. In this section, this evaluation method will be used to determine the appropriate platform.

4.5.1 DSI Equations

The inverse Jacobian matrix in equation 4.14 could be written in the form as following:

$$J^{-1} = [J_X^{-1}| \quad J_Y^{-1}| \quad J_\omega^{-1}] \tag{4.15}$$

$$J_X^{-1} = [cos\,\theta_1 \quad cos\,\theta_2 \quad cos\,\theta_3]^T$$

$$J_Y^{-1} = [sin\,\theta_1 \quad sin\,\theta_2 \quad sin\,\theta_3]^T$$

$$J_\omega^{-1} = \begin{bmatrix} (L_{MP}/\sqrt{3})\,sin(\Phi + \pi/6 - \theta_1) \\ (L_{MP}/\sqrt{3})\,sin(\Phi + 5\pi/6 - \theta_2) \\ (L_{MP}/\sqrt{3})\,sin(\Phi + 3\pi/2 - \theta_3) \end{bmatrix}^T$$

Then obtain the DSI values from the equations:

$$\mu = \left(abs\left(det((J^{-1})^T \cdot J^{-1})\right)\right)^{1/2} \tag{4.16}$$

$$\mu_X = \left(abs(J_X^{-T} \cdot J_X^{-1})\right)^{1/2} \tag{4.17}$$

$$\mu_Y = \left(abs(J_Y^{-T} \cdot J_Y^{-1})\right)^{1/2} \tag{4.18}$$

$$\mu_\omega = \left(abs(J_\omega^{-T} \cdot J_\omega^{-1})\right)^{1/2} \tag{4.19}$$

The equations 4.16 ~ 4.19 represent the DSI calculation for the manipulator. The equation 4.16 calculates the overall mobility index μ of the manipulator. It is equal to the square root of the absolute determinant value in the bracket. The values vary when the manipulator reaches different positions in the workspace. The equations 4.17 and 4.18 are the mobility indexes in X, Y directions, which are equal to the square root of the vector product's absolute value. Similarly, the equation 4.19 is the calculation of the rotational performance of the moving platform inside the workspace.

Where the DSI value is higher, the manipulator could have a better performance in one direction. Before choose the ideal platform size, it is necessary to compare the DSI performances among the four configurations in Section 4.5.2.

4.5.2 Comparison

In this section, the DSI performance among the four configurations will be compared in Table 4.2. The highest and average performance values inside the workspace are calculated. To verify if the Configuration 4 has a good performance, it is needed to conduct the DSI distribution analysis for two configurations from overall DSI analysis to rotational DSI analysis: Configuration 3 and 4.

The detailed comparison results are shown in Table 4.5, 4.7, and 4.8:

Table 4.5: Highest and average DSI values

	Configuration 1	Configuration 2	Configuration 3	Configuration 4
Highest Overall DSI	2.9042e-07	22.175	9.5903e-07	23.049
Average Overall DSI	8.1414e-08	14.642	1.5164e-07	10.119
Highest DSI in X Direction	1.4312	1.2796	1.7273	1.6201
Average DSI in X Direction	1.2352	0.95718	1.1746	1.2205
Highest DSI in Y Direction	1.5217	1.6664	1.7280	1.7280
Average DSI in Y Direction	1.1986	1.4274	1.0407	1.1133
Highest Rotational DSI	7.9010	17.014	16.330	18.647
Average Rotational DSI	5.3791	14.996	14.114	14.033

From the Table 4.5, it can be observed that the performance of Configuration 2 and 4 are close to each other. However, the values of rotational DSI in each configuration are several times larger than the DSI values in X and Y directions. It is not a calculation error. The equations 4.17 to 4.19 can be rewritten as the equations 4.20 to 4.22.

$$\mu_X = \sqrt{sin^2\,\theta_1 + sin^2\,\theta_2 + sin^2\,\theta_3} \tag{4.20}$$

$$\mu_Y = \sqrt{cos^2\,\theta_1 + cos^2\,\theta_2 + cos^2\,\theta_3} \tag{4.21}$$

$$\mu_\omega = (L_{MP}/\sqrt{3})\sqrt{sin^2(\Phi + \pi/6 - \theta_1) + sin^2(\Phi + 5\pi/6 - \theta_2) + sin^2(\Phi + 3\pi/2 - \theta_3)} \tag{4.22}$$

From the three equations above, it can be observed that μ_X and μ_Y are unit-less indices. However, the index μ_ω has a unit which is based on the unit L_{MP}. Centimeter was used as the unit of length and position in the Matlab code. From the code, the results were obtained in Tables 4.3 and 4.4 before. If use meter as the unit instead of centimeter, the rotational index would become 1/100 of the values in Table 4.5. Calculate the results from two units, the distributions of rotational DSI are shown in Table 4.6.

Table 4.6: Rotational DSI with different units

μ_ω with centimeter unit	μ_ω with meter unit
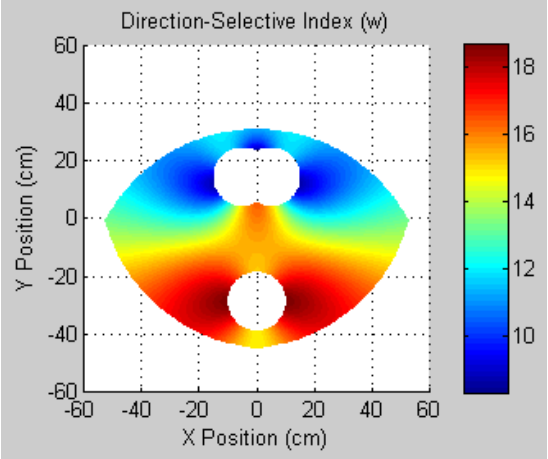	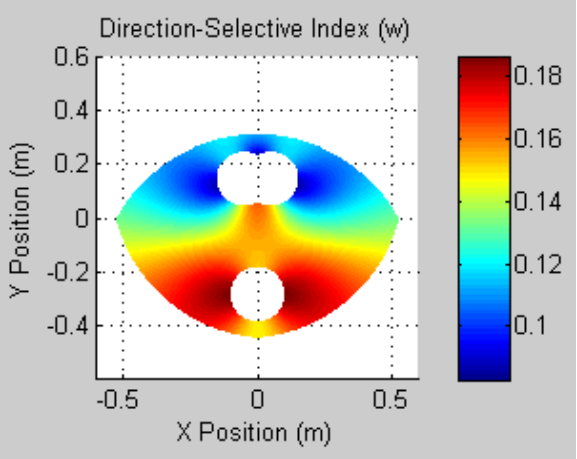

From the analysis in Section 4.4, the Configuration 2 has a smaller workspace than the Configuration 4. Furthermore, the Configuration 3 has the largest workspace area, the performance of which is close to Configuration 4 except for the overall DSI performance. In the Table 4.7 and 4.8, the DSI distribution of these two configurations are analyzed for detailed information.

Table 4.7: DSI analysis results of Configuration 3

	Configuration 3
Overall DSI	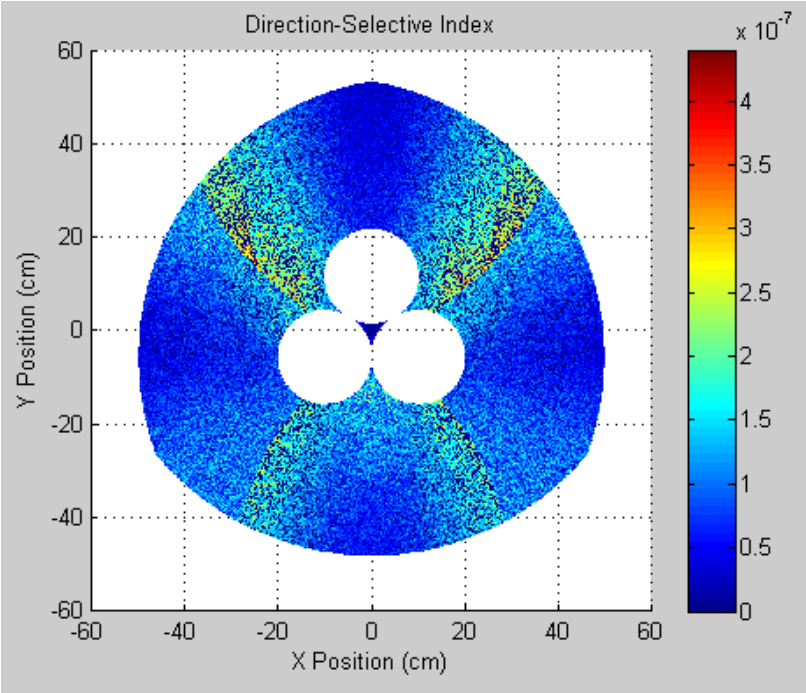
DSI in X Direction	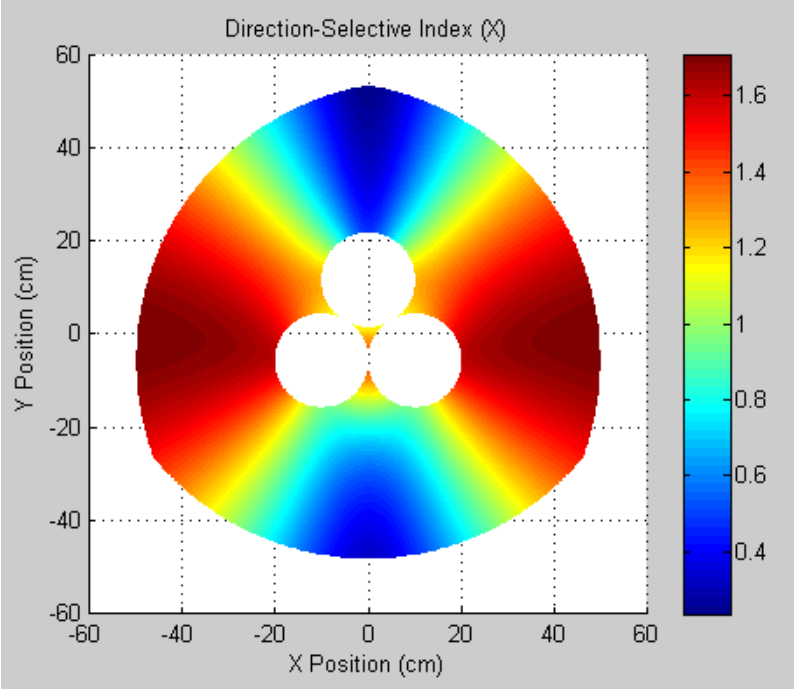

DSI in Y Direction	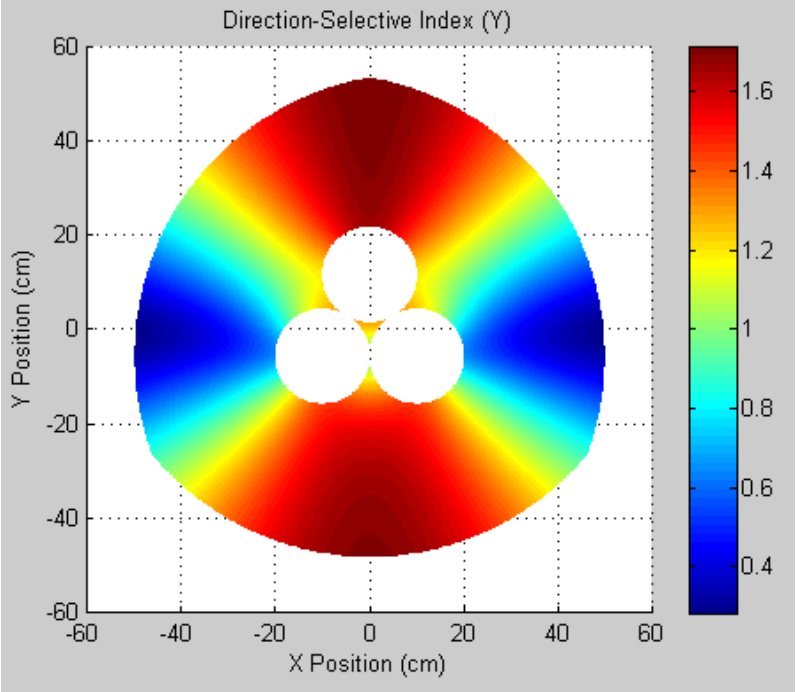
Rotational DSI	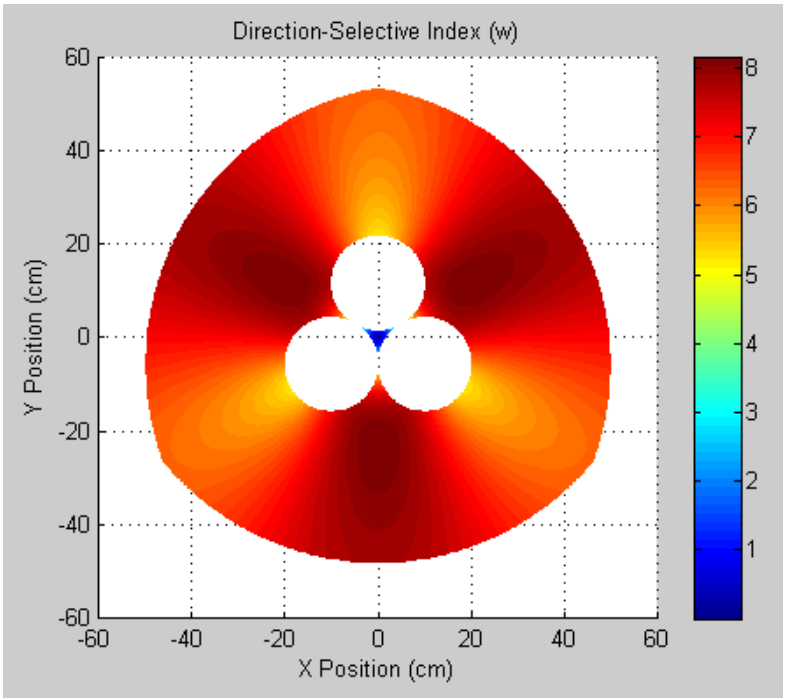

Table 4.8: DSI analysis results of Configuration 4

	Configuration 4
Overall DSI	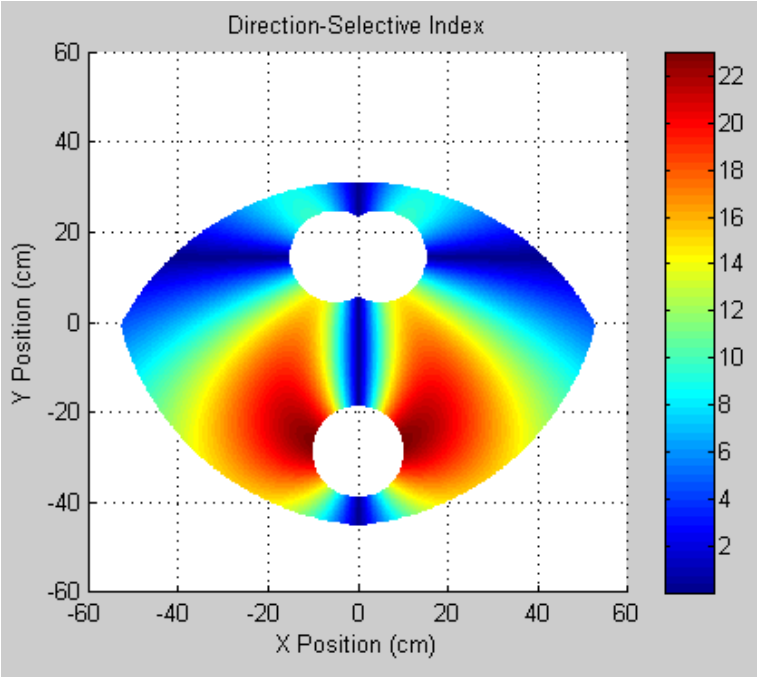
DSI in X Direction	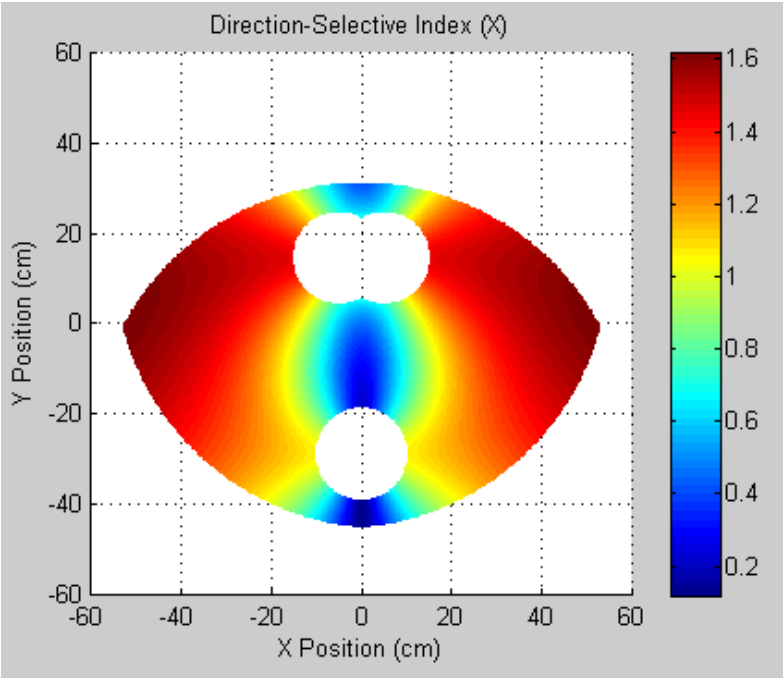

DSI in Y Direction	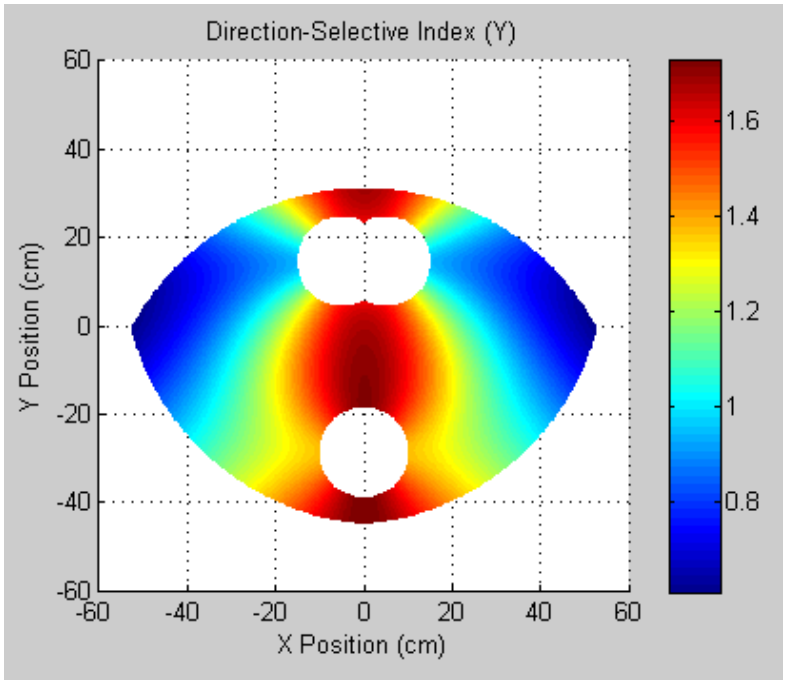
Rotational DSI	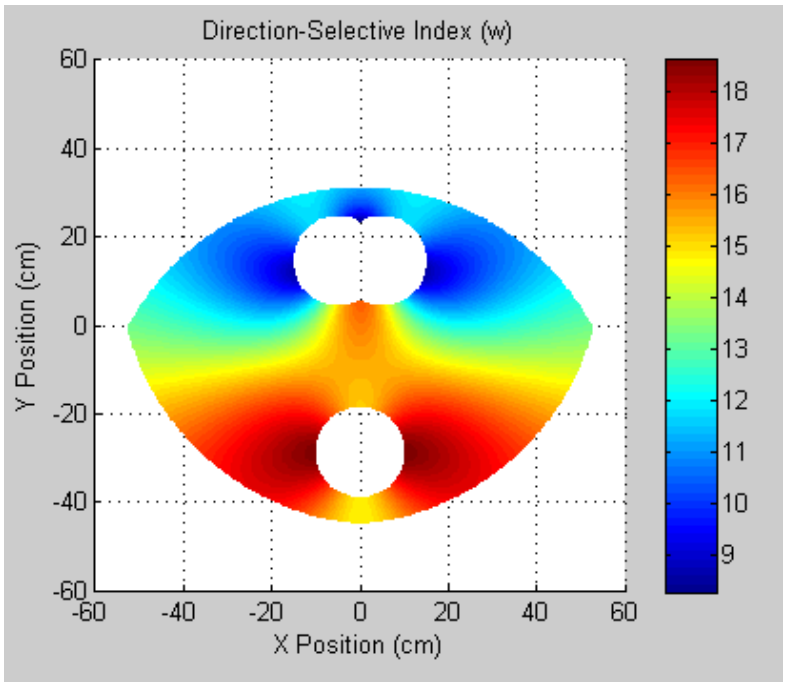

From the results in the Table 4.7 and 4.8, it could be observed that the overall DSI distribution and the determinant of inverse Jacobian matrix distribution are very close to

each other. When the platform is closer to the fixed joints, the manipulator has the higher performance.

The Configuration 1 and the Configuration 3's overall DSI values are very close to zero anywhere within the workspace as well. Symmetry is the reason of that. As a result, choose the asymmetrical configuration: Configuration 4.

4.5.3 Platform Dimension: L_{MP}

The ratio between platform dimension "L_{MP}" and fixed points distance will be modified to obtain the appropriate side length for moving platform. From the figures in Table 4.8, it can be observed that the lower left or right section would be a suitable workspace for manipulator. The highest and average performance indices are calculated with different ratios between L_{MP} and the distance between fixed joints.

$$\text{ratio} = L_{MP}/|\overline{A_1A_2}| \tag{4.23}$$

Then put all the results into the Table 4.9 and plot them.

Table 4.9: Performance Indices Calculation

Ratio	Highest Determinant	Average Determinant	Highest DSI	Average DSI	Highest DSI X
0.1	4.4563	1.9403	4.4563	1.9403	1.6627
0.2	8.6997	3.8679	8.6997	3.8679	1.6566
0.3	12.6084	5.7229	12.6084	5.7229	1.6506
0.4	16.145	7.6408	16.145	7.6408	1.6437
0.5	19.262	9.5505	19.262	9.5505	1.6339
0.6	22.0161	11.3914	22.0161	11.3914	1.6239
0.7	24.4418	13.1446	24.4418	13.1446	1.6123
0.8	26.5253	14.7908	26.5253	14.7908	1.5982
0.9	28.3687	16.3127	28.3687	16.3127	1.5823
1	29.9902	17.693	29.9902	17.693	1.564
1.1	31.3675	18.7193	31.3675	18.7193	1.5437
1.2	32.6124	19.4945	32.6124	19.4945	1.5221
	Average DSI X	**Highest DSI Y**	**Average DSI Y**	**Highest DSI ω**	**Average DSI ω**
0.1	1.2665	1.7024	1.0766	2.9911	2.29E+00
0.2	1.2596	1.7087	1.0839	5.9494	4.55E+00
0.3	1.2539	1.7143	1.0889	8.8423	6.79E+00
0.4	1.2383	1.7189	1.1073	11.6817	9.03E+00
0.5	1.219	1.723	1.1295	14.4502	1.13E+01
0.6	1.1991	1.7263	1.151	17.1356	1.35E+01
0.7	1.1782	1.7288	1.1723	19.7819	1.57E+01

	Average DSI X	Highest DSI Y	Average DSI Y	Highest DSI ω	Average DSI ω
0.8	1.1564	1.7306	1.1934	22.3659	1.78E+01
0.9	1.1339	1.7317	1.2145	24.8811	1.99E+01
1	1.1116	1.7321	1.2358	27.3774	2.20E+01
1.1	1.0942	1.7317	1.2536	29.8267	2.38E+01
1.2	1.0752	1.7306	1.2731	32.2259	2.56E+01

Plot the highest values of three DSI indices versus ratio. From the Figure 4.8, it can be observed that the highest rotational performance indices would be much superior to the other two indices. Then plot the average values of the three DSI indices, which is the diagram in Figure 4.9. The results are close to the ones in Figure 4.8.

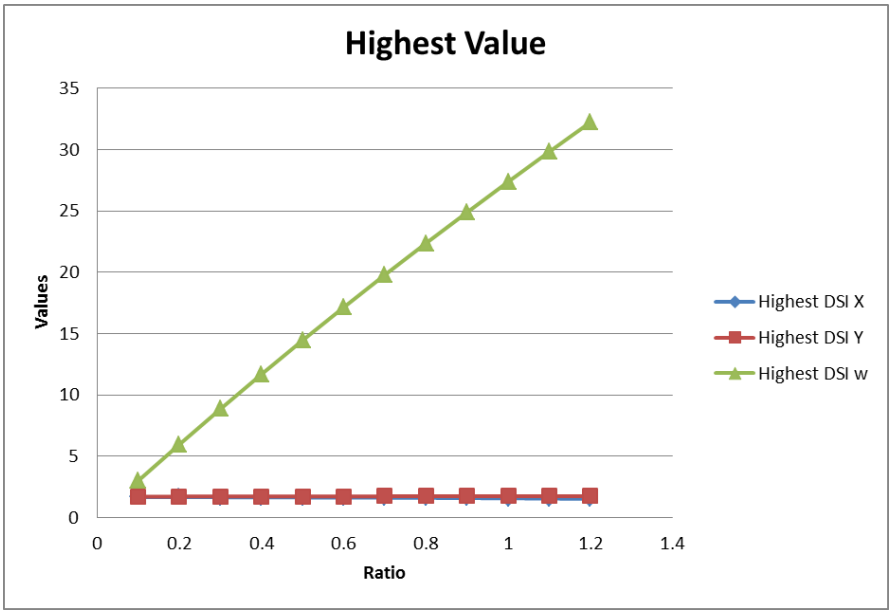

Figure 4.8: Highest values of three performance indices

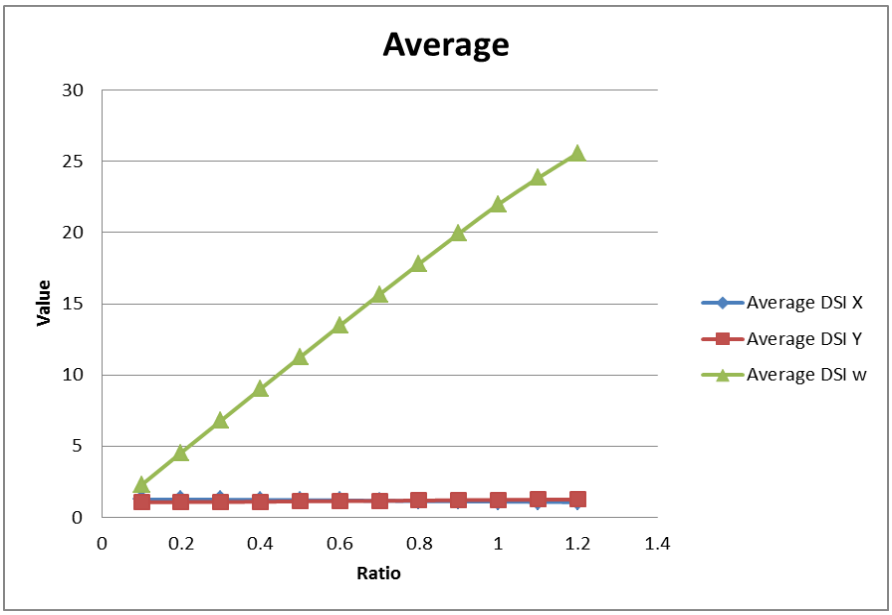

Figure 4.9: Average values of three performance indices

According to the description of the rotational DSI in Section 4.5.2, it can be observed that the units of the DSI X and Y are different to the rotational DSI. In other words, the rotational DSI is a performance index in a different domain. As a result, this index should not be included to study the proper platform dimension.

Then plot the highest values of X and Y DSI indices versus ratio in Figure 4.10. In addition, plot the average values diagram in Figure 4.11. The difference between Figure 4.8 and 4.10 is that the rotational DSI index is not included in the Figure 4.10. It was not included in Figure 4.11 either.

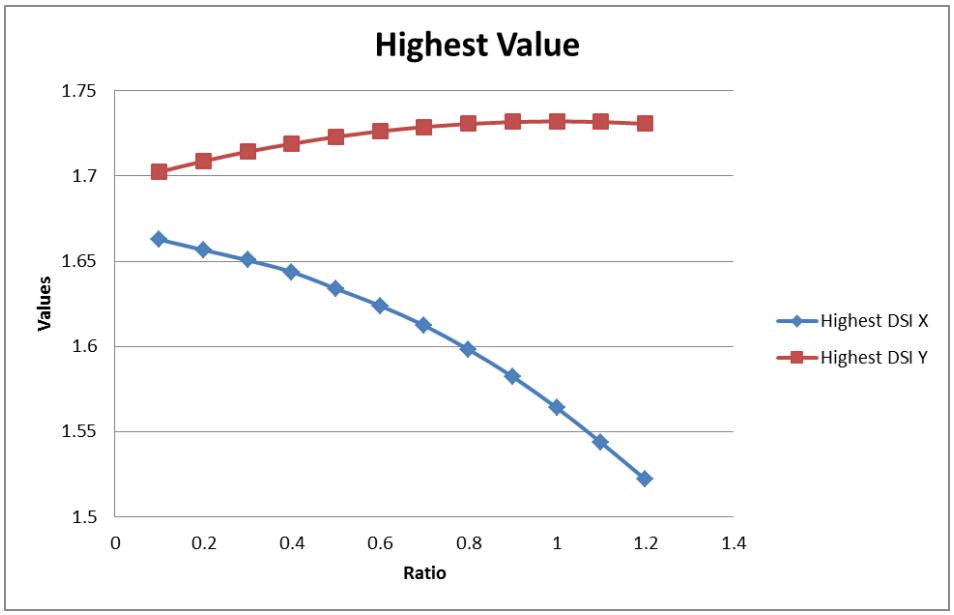

Figure 4.10: Highest values of two performance indices

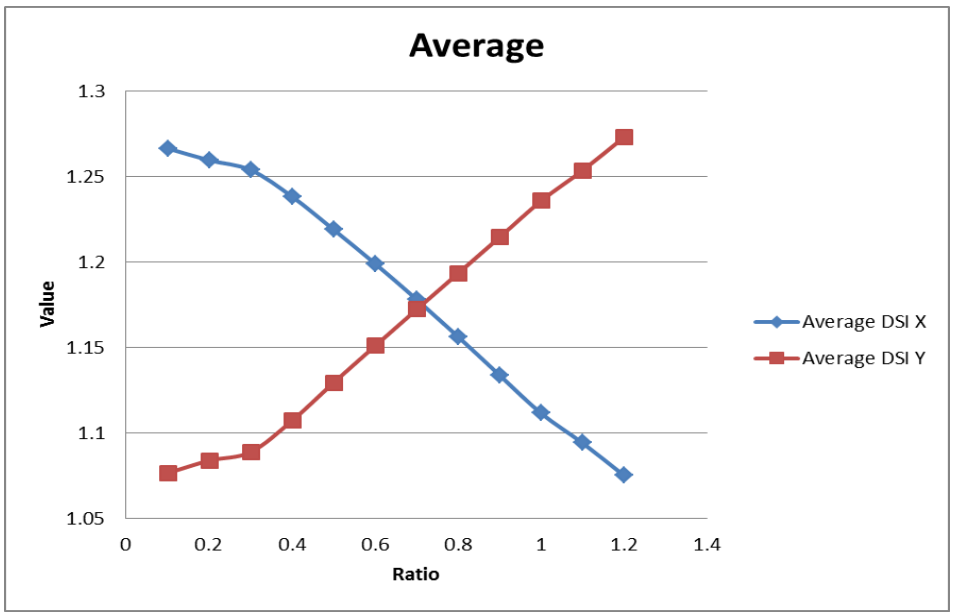

Figure 4.11: Average values of two performance indices

From the Figure 4.10, it can be observed that when the ratio is getting higher, the manipulator would have a better performance in Y direction; however, it would see it

becoming lower in the X direction. On the other hand, from the result in Figure 11, the manipulator has a good compromise between the mobility performances in both directions when the ratio is close to 0.7. From the anterior calculation and analysis, a good 3-RPR configuration design can be chosen. As a result, 200 mm is selected as the platform dimension: L_{MP}.

In this Chapter, the kinematic analysis of the 3-RPR PPM has been conducted. The analysis is the base to choose an appropriate configuration and improve its performance. With the configuration, the manipulator has a good compromise between the workspace area and the mobility performance.

Chapter 5

Kinematic Analysis with the Matrix Approach

In this chapter, one matrix approach (homogeneous transforms) is going to be used to analyze the kinematic problems of the manipulator according to reference [23]. As this approach will provide the required variables for the virtual work inverse dynamic analysis in next chapter, a harmonized kinematic analysis with this method will be conducted, which is appealingly different from the approach in Chapter 4. The goal is to obtain the link length L_i, linear velocity $\dot{L}_\iota$ and acceleration $\ddot{L}_\iota$ from this approach according to a certain position, velocity and acceleration of the moving platform.

5.1 Description of Model

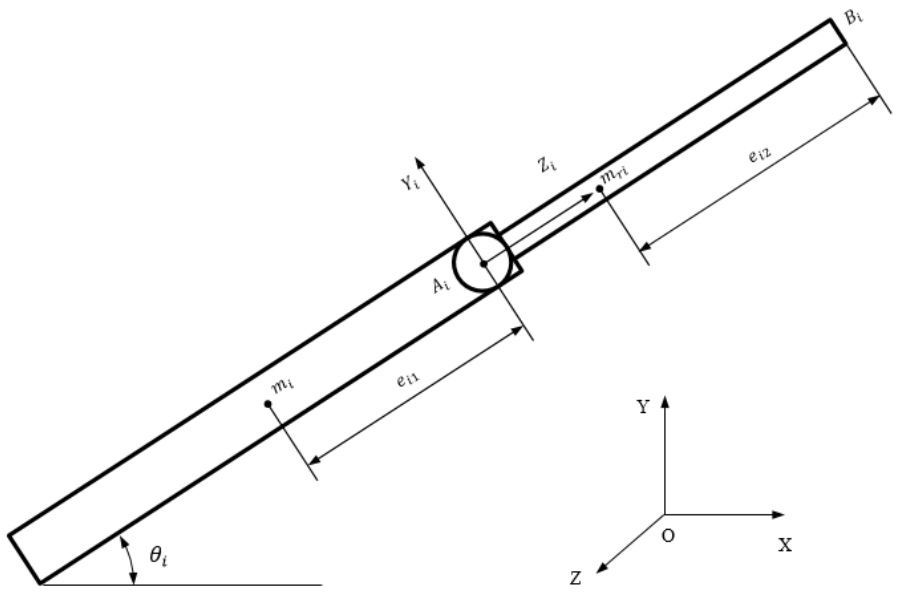

Figure 5.1: 3-RPR link i for kinematic and virtual work analysis

As shown in Figure 5.1, put the manipulator in the X-Y plane of the global reference frame. Then the gravity force points towards the negative direction of the Z axis. The body-fixed reference frame is X_i-Y_i-Z_i, which is similar to the body-fixed frame X'-Y' in Chapter 4. The X_i axis is defined by right handed rule from Y_i and Z_i. The "Z_i" axis is parallel to the pointing axis of the moving-platform. The angle this pointing axis rotating along the global Z axis determines the orientation of each link: "θ_i".

The rotational center of link i is the original point of the body fixed reference frame. The position of linkage mass center is recorded as e_{i1} and e_{i2}. The detailed description is illustrated in the "Nomenclature" section.

5.2 Kinematics of 3-RPR PPM

Firstly, it is needed to define the rotational matrix between the moving platform's body-fixed reference "B" and the global reference "O" as ${}^{O}R_B$. If multiple matrix ${}^{O}R_B$ by the coordinates in reference B, its coordinates in global reference frame could be obtained. From Figure 5.2, axes u and v are the same as the vectors X' and Y' in Figure 4.1 of the Chapter 4. As a result, a third w axis could be got by right-handed principle from u and v, which points out from the plane defined by u and v axes perpendicularly.

$$ {}^{O}R_B = \begin{bmatrix} \cos\Phi & -\sin\Phi & 0 \\ \sin\Phi & \cos\Phi & 0 \\ 0 & 0 & 1 \end{bmatrix} \tag{5.1} $$

The angular velocity of the moving platform ω_p can be written in terms of the angle and body-fixed w axis, which is shown below:

$$\boldsymbol{\omega}_p = \begin{bmatrix} 0 \\ 0 \\ \dot{\Phi} \end{bmatrix} \tag{5.2}$$

Similarly, express he angular acceleration of moving platform:

$$\dot{\boldsymbol{\omega}}_p = \begin{bmatrix} 0 \\ 0 \\ \ddot{\Phi} \end{bmatrix} \tag{5.3}$$

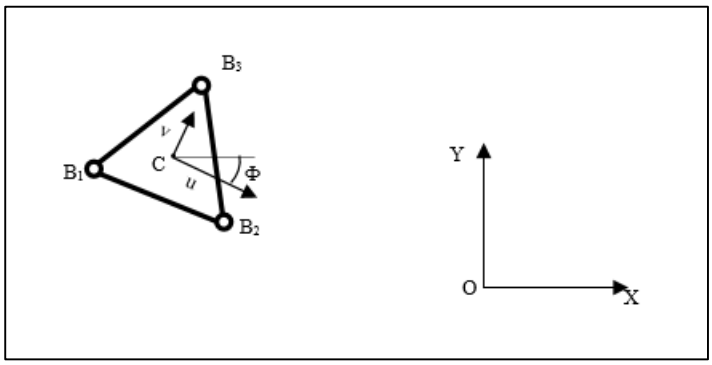

Figure 5.2: Moving platform reference

5.2.1 Position Analysis

The position vector loop for each link could be written as:

$$\boldsymbol{a_i} + L_i \boldsymbol{s_i} = \mathbf{p} + \boldsymbol{b_i} \tag{5.4}$$

Where "$\boldsymbol{a_i}$" is the position vector of 3 fixed points "A_i": $[A_{iX} \quad A_{iY} \quad 0]^T$. L_i is the distance between A_i and B_i, which could be obtained from equation 4.10. "$\boldsymbol{s_i}$" is the unit vector of link i in global reference frame, which comes from equation 5.7. "**p**" is the position vector of moving platform, which is $[X \quad Y \quad 0]^T$. "$\boldsymbol{b_i}$" represents the position vector pointing to Point B_i from Point C, which is similar to the vector -$\overline{B_i C}$ in Figure 4.1.

The rotational matrix between link i and global reference frame could be written as:

$$ {}^{O}R_i = \begin{bmatrix} 0 & -\sin\theta_i & \cos\theta_i \\ 0 & \cos\theta_i & \sin\theta_i \\ -1 & 0 & 0 \end{bmatrix} \tag{5.5} $$

The unit vector $\boldsymbol{s_i}$ comes from the unit vector in link i: ${}^{\boldsymbol{i}}\boldsymbol{s_i}$

$$ {}^{\mathbf{i}}\mathbf{s}_{\mathbf{i}} = \begin{bmatrix} 0 \\ 0 \\ 1 \end{bmatrix} \tag{5.6} $$

$$ \boldsymbol{s_i} = {}^{O}R_i \ {}^{\boldsymbol{i}}\boldsymbol{s_i} $$

$$ \boldsymbol{s_i} = \begin{bmatrix} \cos\theta_i \\ \sin\theta_i \\ 0 \end{bmatrix} \tag{5.7} $$

In order to obtain $\boldsymbol{b_i}$, define the position vector from C to B_i in body-fixed reference frame as ${}^{\boldsymbol{B}}\boldsymbol{b_i}$. The equation is similar to equation 5.7 above:

$$ \boldsymbol{b_i} = {}^{O}R_B \ {}^{\boldsymbol{B}}\boldsymbol{b_i} $$

$$ \begin{cases} {}^{\mathbf{B}}\mathbf{b_1} & \left[-\cos(\pi/6) * \mathrm{L_{MP}}/\sqrt{3} \quad -\sin(\pi/6) * \mathrm{L_{MP}}/\sqrt{3} \quad 0\right]^{\mathrm{T}} \\ {}^{\mathbf{B}}\mathbf{b_2} = & \left[\cos(\pi/6) * \mathrm{L_{MP}}/\sqrt{3} \quad -\sin(\pi/6) * \mathrm{L_{MP}}/\sqrt{3} \quad 0\right]^{\mathrm{T}} \\ {}^{\mathbf{B}}\mathbf{b_3} & \left[0 \quad \mathrm{L_{MP}}/\sqrt{3} \quad 0\right]^{\mathrm{T}} \end{cases} \tag{5.8} $$

$$ \begin{cases} \boldsymbol{b_1} & \left[-\mathrm{L_{MP}} * \cos(\Phi + \pi/6)/\sqrt{3} \quad -\mathrm{L_{MP}} * \sin(\Phi + \pi/6)/\sqrt{3} \quad 0\right]^{T} \\ \boldsymbol{b_2} = & \left[-\mathrm{L_{MP}} * \cos(\Phi + 5\pi/6)/\sqrt{3} \quad -\mathrm{L_{MP}} * \sin(\Phi + 5\pi/6)/\sqrt{3} \quad 0\right]^{T} \\ \boldsymbol{b_3} & \left[-\mathrm{L_{MP}} * \cos(\Phi + 3\pi/2)/\sqrt{3} \quad -\mathrm{L_{MP}} * \sin(\Phi + 3\pi/2)/\sqrt{3} \quad 0\right]^{T} \end{cases} \tag{5.9} $$

It is obvious that the relative between points Bi and C are as same as right part of the result from equation 4.6, 4.7 and 4.8. In order to calculate the leg lengths and orientation for each link, use “norm” and “atan2” function in Matlab, which is shown below:

$$L_i = \|\mathbf{p} + \boldsymbol{b_i} - \boldsymbol{a_i}\| \tag{5.10}$$

$$\mathbf{s_i} = (\mathbf{p} + \boldsymbol{b_i} - \boldsymbol{a_i})/L_i$$
$$\theta_i = atan2(s_{iy}, s_{ix}) \tag{5.11}$$

The result from equation 5.10 and 5.11 are as same as the one from equation 4.10 and 4.11. The position vector of mass center could be represented as equation 5.12 and 5.13. The detailed description of "r_{1i}" and "r_{2i}" could be found in Nomenclature section.

$$\mathbf{r_{1i}} = \boldsymbol{a_i} - e_{i1}\mathbf{s_i} \tag{5.12}$$
$$\mathbf{r_{2i}} = \boldsymbol{a_i} + (L_i - e_{i2})\mathbf{s_i} \tag{5.13}$$

5.2.2 Velocity Analysis

In order to calculate linear velocity of each link, firstly calculate the derivative of the equation 5.4. As a consequence, the equation 5.14 could be obtained:

$$\boldsymbol{v_{bi}} = \boldsymbol{v_p} + \dot{\Phi}\begin{bmatrix} -\sin\Phi & -\cos\Phi & 0 \\ \cos\Phi & -\sin\Phi & 0 \\ 0 & 0 & 0 \end{bmatrix} * {}^{B}\boldsymbol{b_i}$$
$$\boldsymbol{v_{bi}} = \boldsymbol{v_p} + \dot{\Phi}\begin{bmatrix} 0 & -1 & 0 \\ 1 & 0 & 0 \\ 0 & 0 & 0 \end{bmatrix} * \boldsymbol{b_i}$$
$$\boldsymbol{v_{bi}} = \boldsymbol{v_p} + \boldsymbol{\omega_p} \times \boldsymbol{b_i} \tag{5.14}$$

Secondly, differentiate left-hand side of the equation 5.4 to obtain the equation below:

$$\boldsymbol{v_{bi}} = \dot{L}_i\boldsymbol{s_i} + L_i * \boldsymbol{\omega_i} \times \boldsymbol{s_i} \tag{5.15}$$

Then multiple both sides with rotational matrix ${}^{i}R_O$ (${}^{O}R_i^T$), the equation 5.15 could be rewrite as the equation 5.16:

$${}^{i}\boldsymbol{v_{bi}} = \dot{L}_i\ {}^{i}\boldsymbol{s_i} + L_i * \ {}^{i}\boldsymbol{\omega_i} \times \ {}^{i}\boldsymbol{s_i} \tag{5.16}$$

$$^{i}\boldsymbol{v_{bi}} = {}^{i}R_O * \boldsymbol{v_{bi}}$$

$${}^{i}R_O * (\boldsymbol{\omega_i} \times \boldsymbol{s_i}) = \left({}^{i}R_O * \boldsymbol{\omega_i}\right) \times \left({}^{i}R_O * \boldsymbol{s_i}\right) = {}^{i}\boldsymbol{\omega_i} \times {}^{i}\boldsymbol{s_i}$$

The term " $^{i}\boldsymbol{v_{bi}}$" represents the velocity of point B_i in the body-fixed reference frame, which could be written as $\left[{}^{i}v_{bix},\ {}^{i}v_{biy},\ {}^{i}v_{biz}\right]^{T}$. Left multiple both sides of equation 5.16 by $^{i}\boldsymbol{s_i^T}$ to get the equation below, which could help people obtain linear velocity in each link.

$$\dot{L}_i = {}^{i}v_{biz} \tag{5.17}$$

Because each link does not rotate along its own longitudinal axis, the $\boldsymbol{\omega_i^T s_i} = 0$, so is the " $^{i}\boldsymbol{\omega_i^T}\ {}^{i}\boldsymbol{s_i}$". In order to obtain the angular velocity of each link, left cross-multiple $^{i}\boldsymbol{s_i}$ on both sides of equation 5.16:

$${}^{i}\boldsymbol{s_i} \times {}^{i}\boldsymbol{v_{bi}} = \dot{L}_i\ {}^{i}\boldsymbol{s_i} \times {}^{i}\boldsymbol{s_i} + L_i * {}^{i}\boldsymbol{s_i} \times ({}^{i}\boldsymbol{\omega_i} \times {}^{i}\boldsymbol{s_i})$$

$${}^{i}\boldsymbol{s_i} \times {}^{i}\boldsymbol{v_{bi}} = L_i * \left({}^{i}\boldsymbol{\omega_i} * ({}^{i}\boldsymbol{s_i^T} * {}^{i}\boldsymbol{s_i}) - {}^{i}\boldsymbol{s_i} * ({}^{i}\boldsymbol{s_i^T} * {}^{i}\boldsymbol{\omega_i})\right)$$

$${}^{i}\boldsymbol{\omega_i} = ({}^{i}\boldsymbol{s_i} \times {}^{i}\boldsymbol{v_{bi}})/L_i = \frac{1}{L_i}\begin{bmatrix} -{}^{i}v_{biy} \\ {}^{i}v_{bix} \\ 0 \end{bmatrix} \tag{5.18}$$

Once the angular velocity found, differentiate both sides of the equations 5.12 and 5.13 to obtain the mass center velocity. The expressions are shown in the equations 5.19 and 5.20.

$${}^{i}\boldsymbol{v_{1i}} = -e_{i1}\ {}^{i}\boldsymbol{\omega_i} \times {}^{i}\boldsymbol{s_i} \tag{5.19}$$

$${}^{i}\boldsymbol{v_{ri}} = \dot{L}_i\ {}^{i}s_i + (L_i - e_{i2})\ {}^{i}\boldsymbol{\omega_i} \times {}^{i}\boldsymbol{s_i} \tag{5.20}$$

In order to get angular velocity and velocity in global reference frame, left dot multiple (not cross multiple) the vectors $^{i}\boldsymbol{\omega_i}$, $^{i}\boldsymbol{v_{1i}}$ and $^{i}\boldsymbol{v_{ri}}$ with the matrix ${}^{O}R_i$. From this calculation, the absolute angular velocity ω_i of each link, absolute velocity v_{1i} and v_{2i} of two mass centers could be generated in the end.

5.2.3 Acceleration Analysis

The calculation principle in this section is similar to the one in Section 5.2.2. Firstly, differentiate both sides of equation 5.14 with time to obtain equation 5.21 below:

$$\dot{\boldsymbol{v}}_{\boldsymbol{bi}} = \dot{\boldsymbol{v}}_{\boldsymbol{p}} + \dot{\boldsymbol{\omega}}_{\boldsymbol{p}} \times \boldsymbol{b_i} + \boldsymbol{\omega_p} \times \left(\boldsymbol{\omega_p} \times \boldsymbol{b_i}\right) \tag{5.21}$$

The acceleration of Point B_i could be written as the form following, which is corresponding to the body-fixed frame of link i:

$$^{i}\dot{\boldsymbol{v}}_{\boldsymbol{bi}} = \ {}^{i}R_O * \dot{\boldsymbol{v}}_{\boldsymbol{bi}} \tag{5.22}$$

The acceleration could be expressed with the angular acceleration and linear acceleration in each link. Derivative equation 5.16 to get the equation 5.23:

$$^{i}\dot{\boldsymbol{v}}_{\boldsymbol{bi}} = \ddot{L}_i \ {}^{i}\boldsymbol{s_i} + L_i \ {}^{i}\dot{\boldsymbol{\omega}}_{\boldsymbol{i}} \times \ {}^{i}\boldsymbol{s_i} + L_i \ {}^{i}\boldsymbol{\omega_i} \times \left(\ {}^{i}\boldsymbol{\omega_i} \times \ {}^{i}\boldsymbol{s_i}\right) + 2\dot{L}_i * \ {}^{i}\boldsymbol{\omega_i} \times \ {}^{i}\boldsymbol{s_i}$$

$$^{i}\dot{\boldsymbol{v}}_{\boldsymbol{bi}} = \ddot{L}_i \ {}^{i}\boldsymbol{s_i} + L_i \ {}^{i}\dot{\boldsymbol{\omega}}_{\boldsymbol{i}} \times \ {}^{i}\boldsymbol{s_i} - L_i \ {}^{i}\boldsymbol{s_i}\left(\ {}^{i}\boldsymbol{\omega_i}\right)^2 + 2\dot{L}_i * \ {}^{i}\boldsymbol{\omega_i} \times \ {}^{i}\boldsymbol{s_i} \tag{5.23}$$

The term " $^{i}\dot{\boldsymbol{v}}_{\boldsymbol{bi}}$" represents the acceleration of point B_i in the body-fixed reference frame, which could be written as $\left[\ {}^{i}\dot{v}_{bix},\ {}^{i}\dot{v}_{biy},\ {}^{i}\dot{v}_{biz}\right]^T$. Left multiple both sides of equation 5.23 by $^{i}\boldsymbol{s_i^T}$ to get the equation 5.24 below, giving the linear acceleration in each link.

$$ {}^{i}\dot{v}_{biz} = \ddot{L}_i + L_i\left({}^{i}\boldsymbol{s}_i^T \cdot {}^{i}\boldsymbol{\omega}_i\right) \times {}^{i}\boldsymbol{s}_i - L_i\left({}^{i}\boldsymbol{\omega}_i\right)^2 + 2\dot{L}_i\left({}^{i}\boldsymbol{s}_i^T \cdot {}^{i}\boldsymbol{\omega}_i\right) \times {}^{i}\boldsymbol{s}_i $$

$$ \ddot{L}_i = {}^{i}\dot{v}_{biz} + L_i\left({}^{i}\boldsymbol{\omega}_i\right)^2 \tag{5.24} $$

In order to obtain the angular acceleration of each link, left cross-multiple ${}^{i}\boldsymbol{s}_i$ on both sides of equation 5.23:

$$ {}^{i}\boldsymbol{s}_i \times {}^{i}\dot{\boldsymbol{v}}_{bi} = \ddot{L}_i\ {}^{i}\boldsymbol{s}_i \times {}^{i}\boldsymbol{s}_i + L_i * {}^{i}\boldsymbol{s}_i \times \left({}^{i}\dot{\boldsymbol{\omega}}_i \times {}^{i}\boldsymbol{s}_i\right) + 2\dot{L}_i\ {}^{i}\boldsymbol{s}_i \times \left({}^{i}\boldsymbol{\omega}_i \times {}^{i}\boldsymbol{s}_i\right) $$

$$ {}^{i}\boldsymbol{s}_i \times {}^{i}\dot{\boldsymbol{v}}_{bi} = L_i * {}^{i}\dot{\boldsymbol{\omega}}_i + 2\dot{L}_i\ {}^{i}\boldsymbol{\omega}_i $$

$$ {}^{i}\dot{\boldsymbol{\omega}}_i = \left({}^{i}\boldsymbol{s}_i \times {}^{i}\dot{\boldsymbol{v}}_{bi} - 2\dot{L}_i\ {}^{i}\boldsymbol{\omega}_i\right)/L_i = \frac{1}{L_i}\begin{bmatrix} -{}^{i}\dot{v}_{biy} + \frac{2\ {}^{i}v_{biz}\ {}^{i}v_{biy}}{L_i} \\ {}^{i}\dot{v}_{bix} - \frac{2\ {}^{i}v_{biz}\ {}^{i}v_{bix}}{L_i} \\ 0 \end{bmatrix} \tag{5.25} $$

Then differentiate both sides of equations 5.19 and 5.20 to obtain the mass center acceleration. The expressions are shown in the equations 5.26 and 5.27.

$$ {}^{i}\dot{\boldsymbol{v}}_{1i} = -e_{i1}\ {}^{i}\dot{\boldsymbol{\omega}}_i \times {}^{i}\boldsymbol{s}_i - e_{i1}\ {}^{i}\boldsymbol{\omega}_i \times \left({}^{i}\boldsymbol{\omega}_i \times {}^{i}\boldsymbol{s}_i\right) $$

$$ {}^{i}\dot{\boldsymbol{v}}_{1i} = -e_{i1}\ {}^{i}\dot{\boldsymbol{\omega}}_i \times {}^{i}\boldsymbol{s}_i + e_{i1}\ {}^{i}\boldsymbol{s}_i\left({}^{i}\boldsymbol{\omega}_i\right)^2 \tag{5.26} $$

$$ {}^{i}\dot{\boldsymbol{v}}_{ri} = \ddot{L}_i\ {}^{i}\boldsymbol{s}_i + (L_i - e_{i2})\ {}^{i}\dot{\boldsymbol{\omega}}_i \times {}^{i}\boldsymbol{s}_i + (L_i - e_{i2})\ {}^{i}\boldsymbol{\omega}_i \times \left({}^{i}\boldsymbol{\omega}_i \times {}^{i}\boldsymbol{s}_i\right) + 2\dot{L}_i\ {}^{i}\boldsymbol{\omega}_i \times {}^{i}\boldsymbol{s}_i $$

$$ {}^{i}\dot{\boldsymbol{v}}_{ri} = \ddot{L}_i\ {}^{i}\boldsymbol{s}_i + (L_i - e_{i2})\ {}^{i}\dot{\boldsymbol{\omega}}_i \times {}^{i}\boldsymbol{s}_i - (L_i - e_{i2})\ {}^{i}\boldsymbol{s}_i\left({}^{i}\boldsymbol{\omega}_i\right)^2 + 2\dot{L}_i\ {}^{i}\boldsymbol{\omega}_i \times {}^{i}\boldsymbol{s}_i \tag{5.27} $$

In order to get angular acceleration and linear acceleration of each link in global reference frame, compute the following vectors ${}^{i}\dot{\boldsymbol{\omega}}_i$, ${}^{i}\dot{\boldsymbol{v}}_{1i}$ and ${}^{i}\dot{\boldsymbol{v}}_{ri}$ with the matrix ${}^{O}R_i$. From this calculation, the absolute angular acceleration of each link $\dot{\omega}_i$, absolute acceleration of mass center $\dot{v}_{1i}$ and $\dot{v}_{ri}$ could be determined.

5.3 Summary

In this chapter, matrix approach has been successfully used to analysis the kinematic problems of 3-RPR PPM. After completing all the calculations, the link length L_i, linear velocity $\dot{L}_i$ and acceleration $\ddot{L}_i$ of each link were obtained according to a certain position vector **p**, velocity vector $\boldsymbol{v_p}$ and acceleration vector $\dot{\boldsymbol{v}}_{\boldsymbol{p}}$ of the moving platform. In the next chapter, dynamic analysis with the bond graph approach and the virtual work principle will be conducted.

Chapter 6

Dynamic Analysis

In this chapter, bond graph is going to be utilized to simulate 3-RPR robot's movement under three PID control loops; and to utilize the virtual work principle to conduct inverse dynamic analysis. Because bond graph is a relatively new method in the field of dynamic analysis [18], virtual work principle will be used to verify the dynamics results from bond graph. Consequently, two different methods will be applied for dynamic analysis.

Hence, the bond graph method is used to simulate the movement of 3-RPR robot, as three linear actuators L_i are controlled by three PID loops. Bond graph will be implemented to model the system in the software 20-Sim. 20-Sim is a modeling and simulation program for mechatronic systems. With 20-Sim, the designers can enter the model graphically. The models can simulate and analyze the behavior of multi-domain dynamic systems and the control systems [47]. As 20-Sim is based on the bond graph methodology for modeling and simulation, it is suitable for dynamic analysis.

In the end of this chapter, the virtual work principle is used for inverse dynamic analysis, which aims to find the actuator forces required to generate a desired trajectory of the manipulator [23].

6.1 Introduction to Bond Graph

A bond graph essentially consists of subsystems linked together by lines representing "power bonds". Each bond represents the instantaneous flow of energy (dE/dt) or power [12]. A bond graph is based on graphical configurable blocks like Simulink. Dissimilarly it can incorporate multiple domains seamlessly with ports connecting different sub-systems. Places at which subsystems can be interconnected are those at which power can flow between the subsystems. Such places are called ports [12]. In bond graph, all power variables are called effort or flow. In different domains, they have different units and names.

Table 6.1: Some Effort and Flow Quantities (from reference [12])

Domain	Effort, e(t)	Unit	Flow, f(t)	Unit
Mechanical Translation	Force, F(t)	N	Velocity, V(t)	m/s
Mechanical Rotation	Torque, $\tau(t)$	N.m	Angular Velocity, $\omega(t)$	rad/s
Hydraulic	Pressure, P(t)	Pa	Volume Flow Rate, Q(t)	m^3/s
Electric	Voltage, e(t)	V	Current, i(t)	A

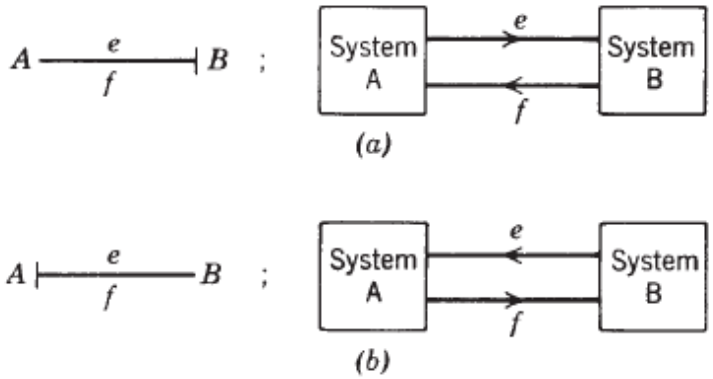

Figure 6.1: Bond graph example with causal strokes (from the reference [12])

Figure 6.1 shows the basic blocks for bond graph, where there is a stroke on the bond, called causal stroke. The stroke means at that place the subsystem receives an effort input. The meaning of causal strokes: (a) effort is output of A, input to B; flow is output of B, input to A; (b) effort is output of B, input to A; flow is output of A, input to B [12]. For further information about bond graph, please read the reference [12], which is a bond graph textbook with detailed explanations and practical examples.

Recently, bond graph just started to be widely applied to the modeling of parallel mechanisms ([10] and [28]). Scientists can simulate different domain systems with bond graph, as it can connect different sub-systems together with bond ports. In the bond graph modeling of the 3-RPR robot, the controller and the motor can be modelled and simulated in the same process. Furthermore, it generates dynamic performance results, while researchers provides the kinematic models of the mechanism.

6.2 A General Description for the Configuration

In the multi-body bond graph, three elements are fundamentally defined to assemble each link. According to Table 6.2, l_i, ρ_i and l_{ri} (i ranges from 1 to 3) form the L_i part in Figure 3.1. The linear actuators can be placed in L_i segments in the bond graph. Furthermore, the moving platform is indicated by one element with body-fixed coordinates. The overall configuration is shown in Figure 6.2. Since the relative motion between l_i and l_{ri} is a linear one, it is more reasonable to choose body-fixed coordinate frame bond graph element rather than global coordinate element.

Table 6.2: Explanations for l_i, ρ_i and l_{ri}

l_i	ρ_i	l_{ri}
		
Represent the cylinder of the linear actuator, which holds the rod inside of it.	Marked by black color in the figure. It is equal to the extended stroke length.	The rod of the lienar actuator, which moves out from the cylinder.

In Figure 6.2, the overall configuration for bond graph analysis is provided. It is similar to the Configuration 4 in Chapter 4. The assembled three elements l_i, ρ_i and l_{ri} are represented in the figure as well.

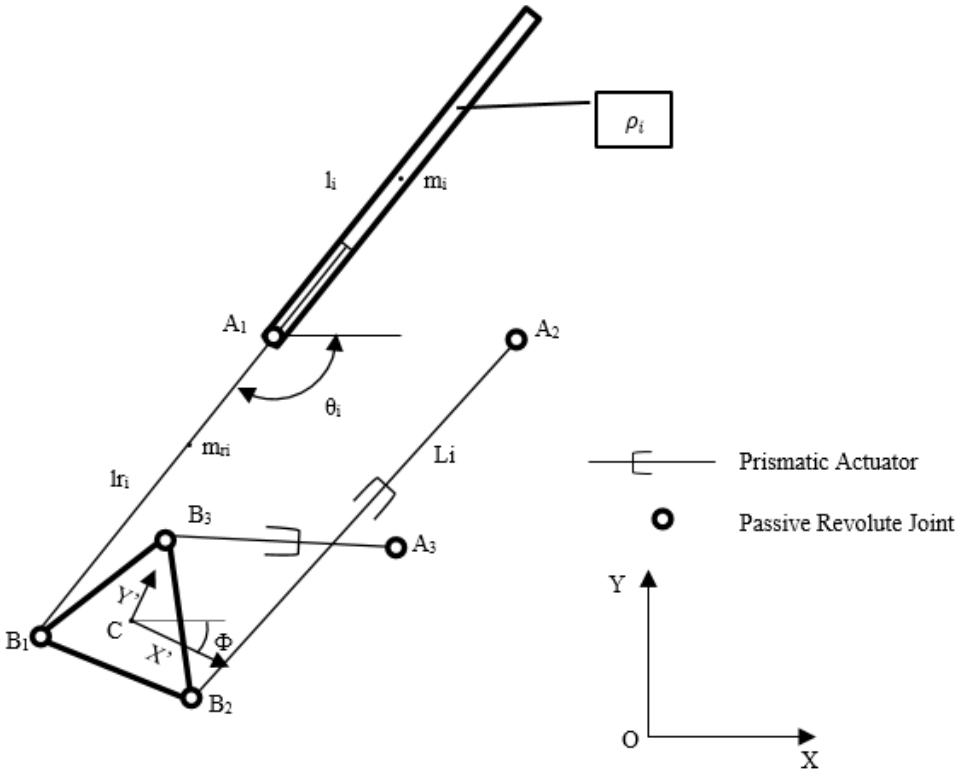

Figure 6.2: 3-RPR mechanism for bond graph

The length of ρ_i ranges from ρ_{imin} to ρ_{imax}, which are equivalent to L_{imin} and L_{imax} in Chapter 4. Because the length of l_i and l_{ri} are equal to each other (600 mm); as a consequence, each leg's minimum length (L_{imin}) is equal to $l_i+\rho_{imin}-l_{ri}$; and the maximum one (L_{imax}) is $l_i-l_{ri}+\rho_{imax}$. When connecting rigid body links together, one parasitic element is needed to eliminate derivative causality. It will be described in Section 6.3.

In terms of actuator segments, build three DC motor models which obtain voltage from the signals of three PID controllers respectively. In addition, three pairs of rack and pinion are represented by "transformers", which convert rotation outputs into translation outputs for actuated portions. According to the target end-effector pose, the inverse kinematic model provides target lengths for the three ρ_i parts, which are the positive signals to the PID controllers; on the other hand, the actual measured length values are the feedback signals to the PID controllers.

6.3 Development of Bond Graph Model

6.3.1 Body-fixed Coordinates

Define the coordinate frame rotating along with the rigid body as a body-fixed coordinate frame. The direction along each link is X_i', consisting a right-hand coordinate frame with another axis Y_i', which is perpendicular to it. The relationship between absolute coordinates (X_i,Y_i) and body-fixed coordinates (X_i', Y_i') is shown in equation 6.1.

$$\begin{bmatrix} X_i \\ Y_i \end{bmatrix} = \begin{bmatrix} \cos(\theta_i) & -\sin(\theta_i) \\ \sin(\theta_i) & \cos(\theta_i) \end{bmatrix} \begin{bmatrix} X_i' \\ Y_i' \end{bmatrix} \quad (6.1)$$

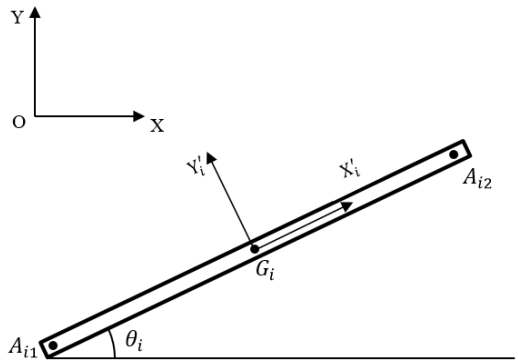

Figure 6.3: The L_i configuration in bond graph

"θ_i" represents the rigid body's orientation angle, which is explained in Chapter 4. In order to obtain a formula associated with relative linear velocity: $\dot{X}'_i$, $\dot{Y}'_i$ and angular velocity $\dot{\theta}_i$, differentiate equation 6.1 on both sides to obtain the equation 6.2.

$$\begin{bmatrix} V_{iX} \\ V_{iY} \end{bmatrix} = \begin{bmatrix} \cos(\theta_i) & -\sin(\theta_i) \\ \sin(\theta_i) & \cos(\theta_i) \end{bmatrix} \begin{bmatrix} \dot{X}'_i \\ \dot{Y}'_i \end{bmatrix} + \dot{\theta}_i * \begin{bmatrix} -\sin(\theta_i) & -\cos(\theta_i) \\ \cos(\theta_i) & -\sin(\theta_i) \end{bmatrix} \begin{bmatrix} X'_i \\ Y'_i \end{bmatrix} \quad (6.2)$$

From the equation above, it can be observed that the linear velocity of a general point in the global reference frame is not equal to the relevant linear velocity required by homogenous transforms. Define V'_{iX} and V'_{iY} as the expression of V_{iX} and V_{iY} in body based reference frame. The meaning of both could be written as the following equation:

$$\begin{bmatrix} V'_{iX} \\ V'_{iY} \end{bmatrix} = \begin{bmatrix} \cos(\theta_i) & \sin(\theta_i) \\ -\sin(\theta_i) & \cos(\theta_i) \end{bmatrix} \begin{bmatrix} V_{iX} \\ V_{iY} \end{bmatrix} \quad (6.3)$$

Afterwards, multiple equation 6.2 by the rotational matrix in equation 6.3 on both side, it could be rewritten as equation 6.4 below:

$$\begin{bmatrix} V'_{iX} \\ V'_{iY} \end{bmatrix} = \begin{bmatrix} 1 & 0 \\ 0 & 1 \end{bmatrix} \begin{bmatrix} \dot{X}'_i \\ \dot{Y}'_i \end{bmatrix} + \dot{\theta}_i * \begin{bmatrix} 0 & -1 \\ 1 & 0 \end{bmatrix} \begin{bmatrix} X'_i \\ Y'_i \end{bmatrix}$$

$$\begin{bmatrix} V'_{iX} \\ V'_{iY} \end{bmatrix} = \begin{bmatrix} \dot{X}'_i \\ \dot{Y}'_i \end{bmatrix} + \dot{\theta}_i \times \begin{bmatrix} X'_i \\ Y'_i \end{bmatrix} \tag{6.4}$$

According to the equation above, bond graph model could be built based on body fixed coordinate. The figure below shows a general configuration of link l_i. The original point of reference frame is the link center, G_i. The definition of A_{i1} and A_{i2} are described in the "Nomenclature" section. In l_{ri} link, "A" and "G_i" will be replaced with "B" and "G_{ii}". The relationship between linear velocity and angular velocity are shown in Table 6.3:

Table 6.3: Velocity relationship

Link	**Angular Velocity**	**Center of Mass**	**First Point**	**Second Point**
l_i	$\dot{\theta}_i$	G_i	A_{i1}	A_{i2}
	$\begin{bmatrix} V'_{GiX} \\ V'_{GiY} \end{bmatrix} = \begin{bmatrix} \dot{G}'_{iX} \\ \dot{G}'_{iY} \end{bmatrix} + \dot{\theta}_i \times \begin{bmatrix} G'_{iX} \\ G'_{iY} \end{bmatrix}$ $d \begin{bmatrix} m_i V'_{GiX} \\ m_i V'_{GiY} \end{bmatrix} / dt = \begin{bmatrix} m_i \ddot{G}'_{iX} \\ m_i \ddot{G}'_{iY} \end{bmatrix} + \dot{\theta}_i \times \begin{bmatrix} m_i \dot{G}'_{iX} \\ m_i \dot{G}'_{iY} \end{bmatrix}$ $\begin{bmatrix} V'_{Ai1X} \\ V'_{Ai2X} \\ V'_{Ai1Y} \\ V'_{Ai2Y} \end{bmatrix} = \begin{bmatrix} V'_{GiX} \\ V'_{GiX} \\ V'_{GiY} - \dot{\theta}_i * l_i/2 \\ V'_{GiY} + \dot{\theta}_i * l_i/2 \end{bmatrix}$			

Link	Angular Velocity	Center of Mass	First Point	Second Point
$\mathbf{l_{ri}}$	$\dot{\theta}_i$	G_{ii}	B_{i1}	B_{i2}
	$\begin{bmatrix} V'_{GiiX} \\ V'_{GiiY} \end{bmatrix} = \begin{bmatrix} \dot{G}'_{iiX} \\ \dot{G}'_{iiY} \end{bmatrix} + \dot{\theta}_i \times \begin{bmatrix} G'_{iiX} \\ G'_{iiY} \end{bmatrix}$ $d \begin{bmatrix} m_{ii} V'_{GiiX} \\ m_{ii} V'_{GiiY} \end{bmatrix} / dt = \begin{bmatrix} m_{ii}\, \ddot{G}'_{iiX} \\ m_{ii}\, \ddot{G}'_{iiY} \end{bmatrix} + \dot{\theta}_i \times \begin{bmatrix} m_{ii}\, \dot{G}'_{iX} \\ m_{ii}\, \dot{G}'_{iY} \end{bmatrix}$ $\begin{bmatrix} V'_{Bi1X} \\ V'_{Bi2X} \\ V'_{Bi1Y} \\ V'_{Bi2Y} \end{bmatrix} = \begin{bmatrix} V'_{GiiX} \\ V'_{GiiX} \\ V'_{GiiY} - \dot{\theta}_i * l_{ri}/2 \\ V'_{GiiY} + \dot{\theta}_i * l_{ri}/2 \end{bmatrix}$			

According to the equations in Table 6.3, develop the bond graph model with body fixed coordinates. There are six links to be generated in the system. In Figure 6.4, the Link l_3 modeling configuration is demonstrated, where the first point is A_{31} and the second one is A_{32}. The second point is fixed with the global fixed point A_3. And there are masses mx and my in X' and Y' directions to generate inertia loads for the rigid body. And "J3" generates the rotational load. The detailed description to bond graph elements is shown in Table 6.4.

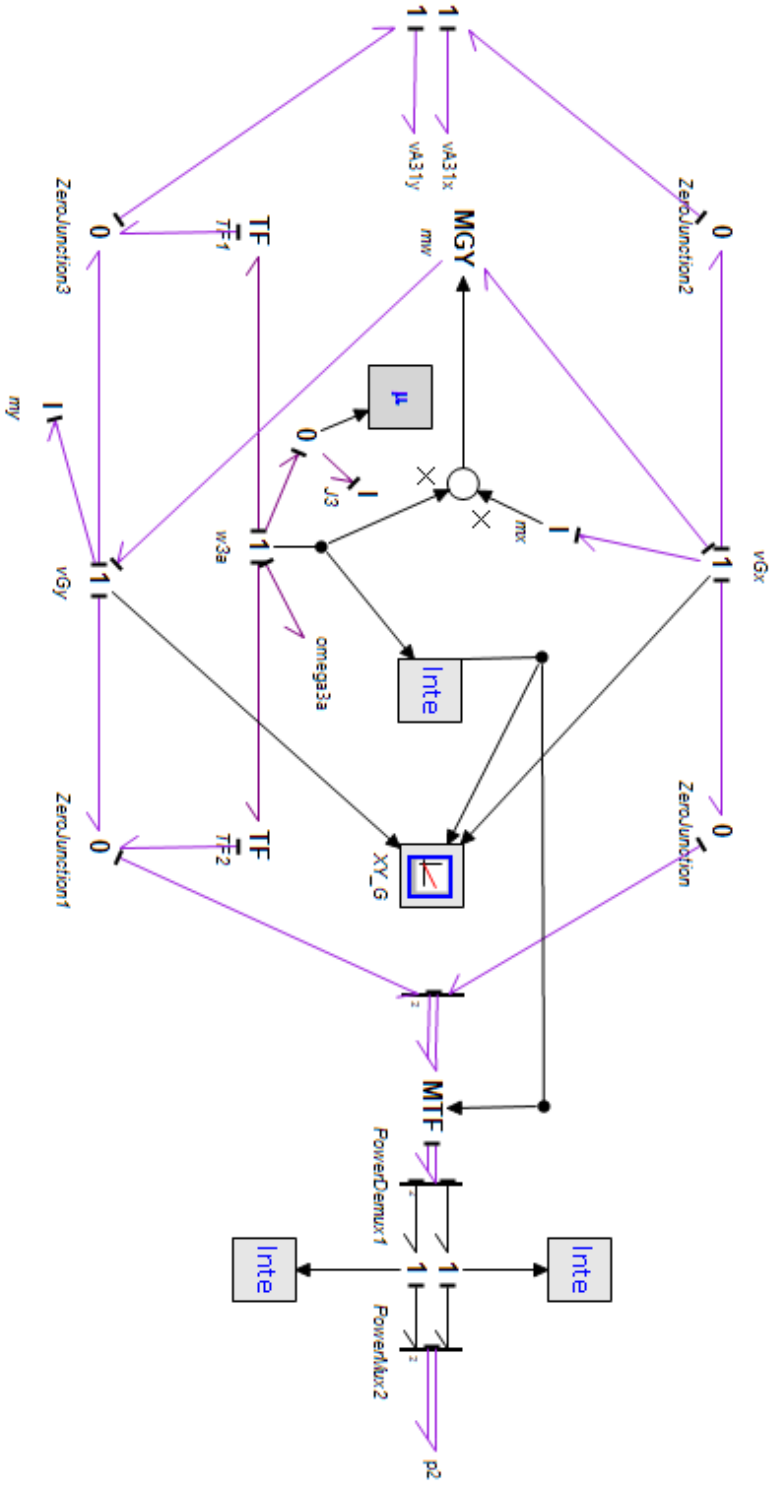

Figure 6.4: Bond graph for L_3

Table 6.4: Explanation of TF, MTF, GY, MGY Elements

Name	Category	Images	Equations	Explanation
Transformer	Effort-In Causality	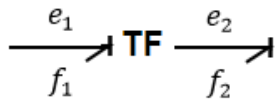	$f_1 = (1/n)f_2$ $e_2 = (1/n)e_1$	(1/n) is the constant value in "TF"
	Effort-Out Causality	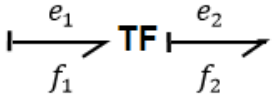	$f_2 = (n)f_1$ $e_1 = (n)e_2$	(n) is the constant value in "TF"
Gyrator	Effort-In Causality	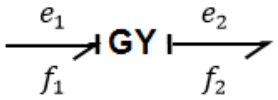	$f_1 = (1/r)e_2$ $f_2 = (1/r)e_1$	(1/r) is the constant value in "GY"
	Effort-Out Causality	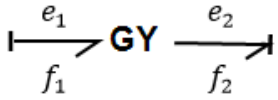	$e_2 = (r)f_1$ $e_1 = (r)f_2$	(r) is the constant value in "GY"
Modulated Transformer	Effort-In Causality	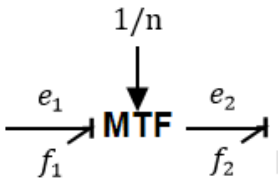	$f_1 = (1/n)f_2$ $e_2 = (1/n)e_1$	(1/n) is the variable in "MTF", defined by outside signal
	Effort-Out Causality	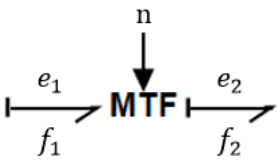	$f_2 = (n)f_1$ $e_1 = (n)e_2$	(n) is the variable in "MTF", defined by outside signal
Modulated Gyrator	Effort-In Causality	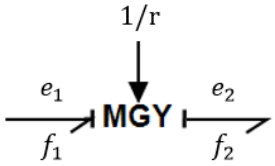	$f_1 = (1/r)e_2$ $f_2 = (1/r)e_1$	(1/r) is the variable in "MGY", defined by outside signal
	Effort-Out Causality	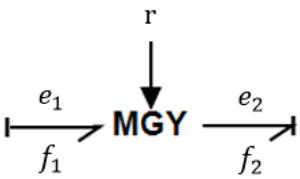	$e_2 = (r)f_1$ $e_1 = (r)f_2$	(r) is the variable in "MGY", defined by outside signal

In Figure 6.4, the right part indicates the velocity and position of A_3 with absolute coordinates. The outputs of integration segments represent the position; in addition, the two-dimensional output is the velocity of point A_3, defined by a flow source in the system, which is equal to 0 constantly. The modulated transformer in "MTF" segment is the inverse matrix in equation 6.3, which is defined by the orientation of link l_3 (output of the angular velocity's integration). The "TF" segment transfers the angular velocity of each link into the linear velocity at the endpoints.

In the left part, there are 2 velocity outputs, which are linear velocities of point A_{31} in 2 dimensions, with body-fixed coordinates. In the "XY_G" segment, the position and the orientation of the center point are defined in link l_3, generating the data required for 3D Animation model in 20-Sim.

In the middle part, the modulated gyrator "MGY" represents the second equation in Table 6.3, which is determinant by the rotational velocity and mass. "I" represents inertia, in the translation system, it would be mass; in rotational system, and it is rotational inertia.

6.3.2 Actuated Parts (ρ_i)

From Figure 6.1, it can be observed that there is no difference in angular velocity between 1_i and l_{ri} (i ranges from 1 to 3) segments. Relative velocity between A_{i1} and B_{i1} in Y_i' direction is related to the length of ρ_i. According the information above and equations in Table 6.3, develop the bond graph model below:

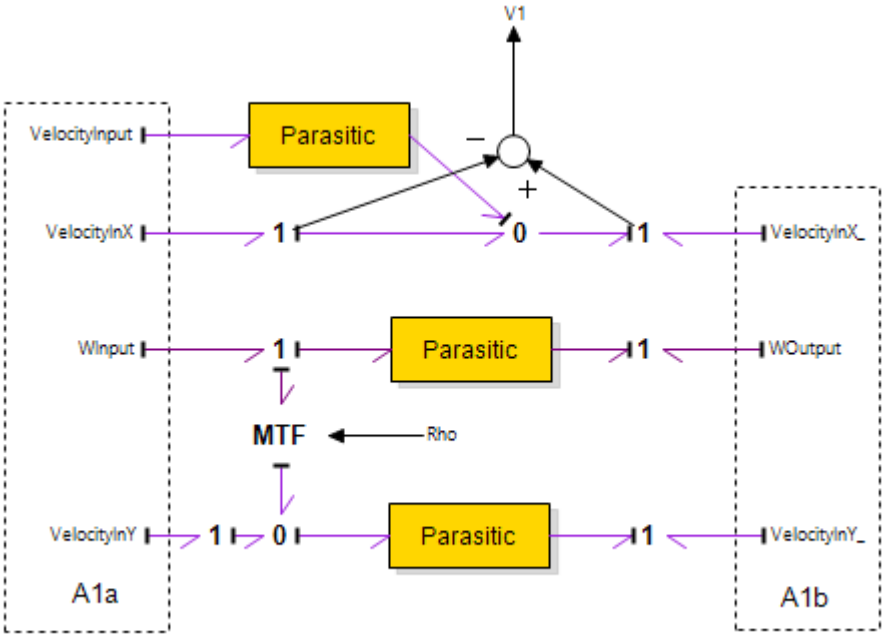

Figure 6.5: Bond graph for actuated part (ρ_i)

Modulated transformer "MTF" obtains the actuated leg length as the "n" variable in Table 6.4. The velocity in Y' direction on the right hand side (A1b) in Figure 6.5 is equal to the one on left hand side (A1a) plus the angular velocity multiple by the actuated length ρ_i. The two links l_i and l_{ri} have the same angular velocity. Furthermore, the velocity in X' direction is equal to the velocity of the rod, which is shown as "VelocityInput" in the figure.

6.3.3 Parasitic Elements

The parasitic elements are applied to model any joint in bond graph. Derivative causality causes the bond graph result to be implicit, which is a situation that should be avoided during bond graph modeling [12]. In order to eliminate derivative causality, parasitic segments are applied to flow outputs in the bond graph system. It could be considered as

one potential energy storage device and one energy consume device with high parameter values, working in parallel on each port.

As two rigid bodies are assumed to connect rigidly, the C and R values are very high in the bond graph model. The model is shown in Table 6.5, where 2 kinds of parasitic elements are demonstrated, both of which are dimensionless.

Table 6.5: Parasitic elements

Parasitic Elements	
One dimension	**Two dimensions**
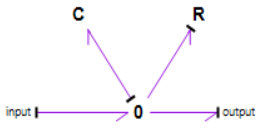	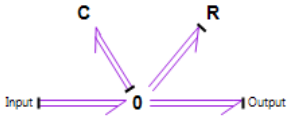

The value of C is 10^{-8}, on the other hand, R value is 2000. The left one has one input and one output, while the right one has a two-by-one vector as input, and a same size vector as output. As the units of them change in different systems but the values remain equal, all of the C and R parameters in parasitic elements are defined by global parameters in the "constant" block.

6.3.4 DC Motors and PID Control

Since the 3-RPR PPM has 3 degree of freedoms (DOF), three motors are required to position the robot end-effector and generate its motion. The robot controller is constituted by three PID controllers.

In Figure 6.6, there are one set point signal and one feedback signal as inputs of each PID controller. The target lengths for each ρ_i part is the positive signal for each PID controller; on the other hand, the actual measured length value is the negative signal to each PID controller. "MSe" represents the modulated voltage input for DC Motor, the value of which is defined by the PID controller. The maximum and minimum outputs from "MSe" is limited by a limiter block in PID segment.

In the DC Motor box, there are one modulated effort source "MSe", one inductance, one resistance and one DC motor connected serially in the left part. The input of this part is the voltage coming from each PID controller, and the output is the current into the DC motor. After that, the gyrator "GY" converts electric current into the torque applied to the rotating shaft. There are a rotational inertia and a rotating friction element consist the motor's mechanical part. The output of the motor is its rotational velocity.

In the "Rack & Pinion Transformer" box, there is a mechanical transformer converting angular velocity into linear velocity, which is the output of the linear actuator. The rack and pinion mechanism provides linear velocity to the system. All the parameters are shown in Table 6.7.

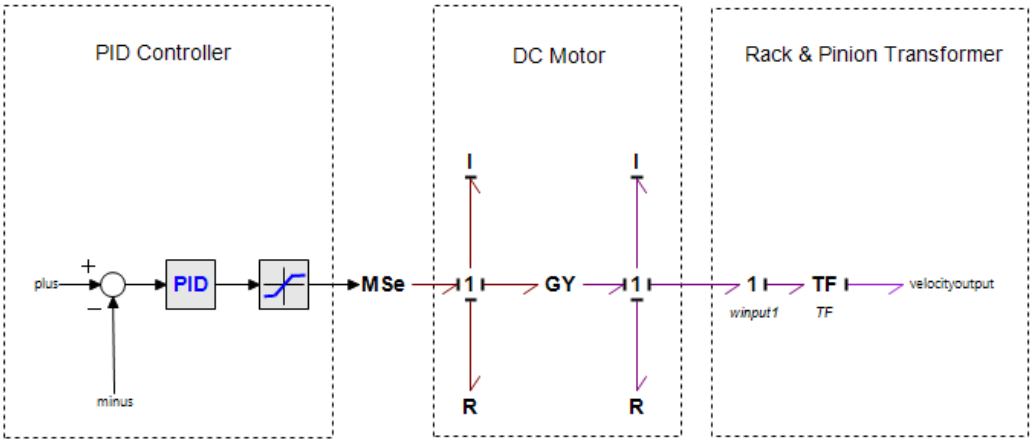

Figure 6.6: DC motor, PID controller and transformer

Table 6.6: Explanation of Figure 6.6

Figure 6.6 Portion	Equivalent Graph
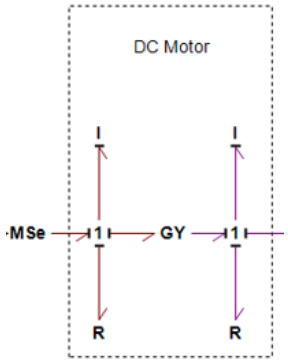	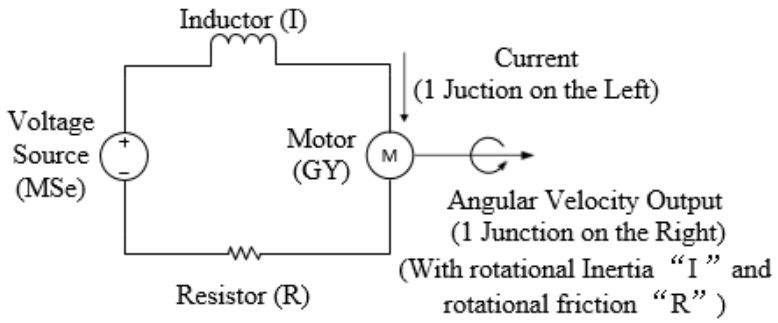
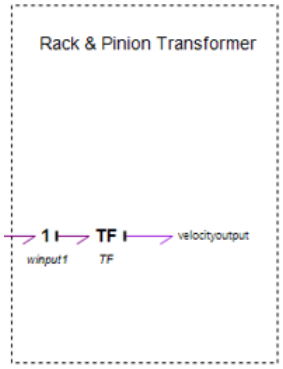	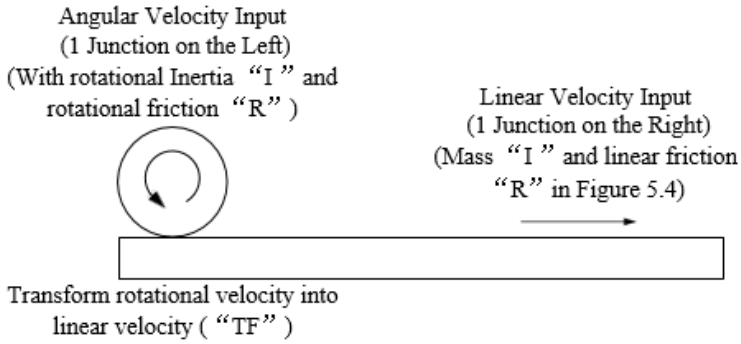

The gyrator in the first row of Table 6.6 is equivalent to the one in the fourth row of Table 6.4, where f_1 is the current, e_1 is the voltage applied on the motor, f_2 is the rotational velocity output and e_2 is the torque output. The relationship among these four variables is shown in Table 6.4 as well.

When I calculate the torque (e2) from the current (f1), the gyrator constant "GY" is the torque constant. On the other hand, when I calculate the voltage (v1) from the rotational velocity (f2), the gyrator constant becomes the back-EMF constant. As it is the practice, the torque and back-EMF constants are set at the same value. As a result, the unit of the gyrator in Table 6.7 is not available. The gyrator constant can be changed in the appropriate block for all equations. The purpose of this thesis is to validate the bond graph in the field of dynamic analysis.

The transformer in the second line of Table 6.6 is equivalent to the one in the second row of Table 6.4, where f_1 is the rotational velocity input, e_1 is the torque applied on the pinion, f_2 is the linear velocity output and e_2 is the force output. The relationship among these four variables is shown in Table 6.4 as well.

Table 6.7: Parameter values

Parameters				
Segment		**Name**	**Value**	**Unit**
PID	**PID**	Kp	30	None
		Td	20	None
		Ti	80	None
	Limit	Max	12	V
		Min	-12	V
DC Motor	**Electric**	I	0.251	mH
		R	0.574	Ω
	Gyrator	GY	145	N/A
	Mechanical	I	1450	g.cm2
		R	86	μN.m.s/rad
TF	**Transform**	TF	0.05	m/rad

6.3.5 Overall Bond Graph

The bond graph system is shown in Figure 6.7, in which with detailed description. In the "Original" segment, initial values for different elements could be set, according to which, all passive joints' initial values can be calculated. In the "Parasitic Damping" segment, the values of C and R are set up for parasitic elements, which is described in Section 6.3.3.

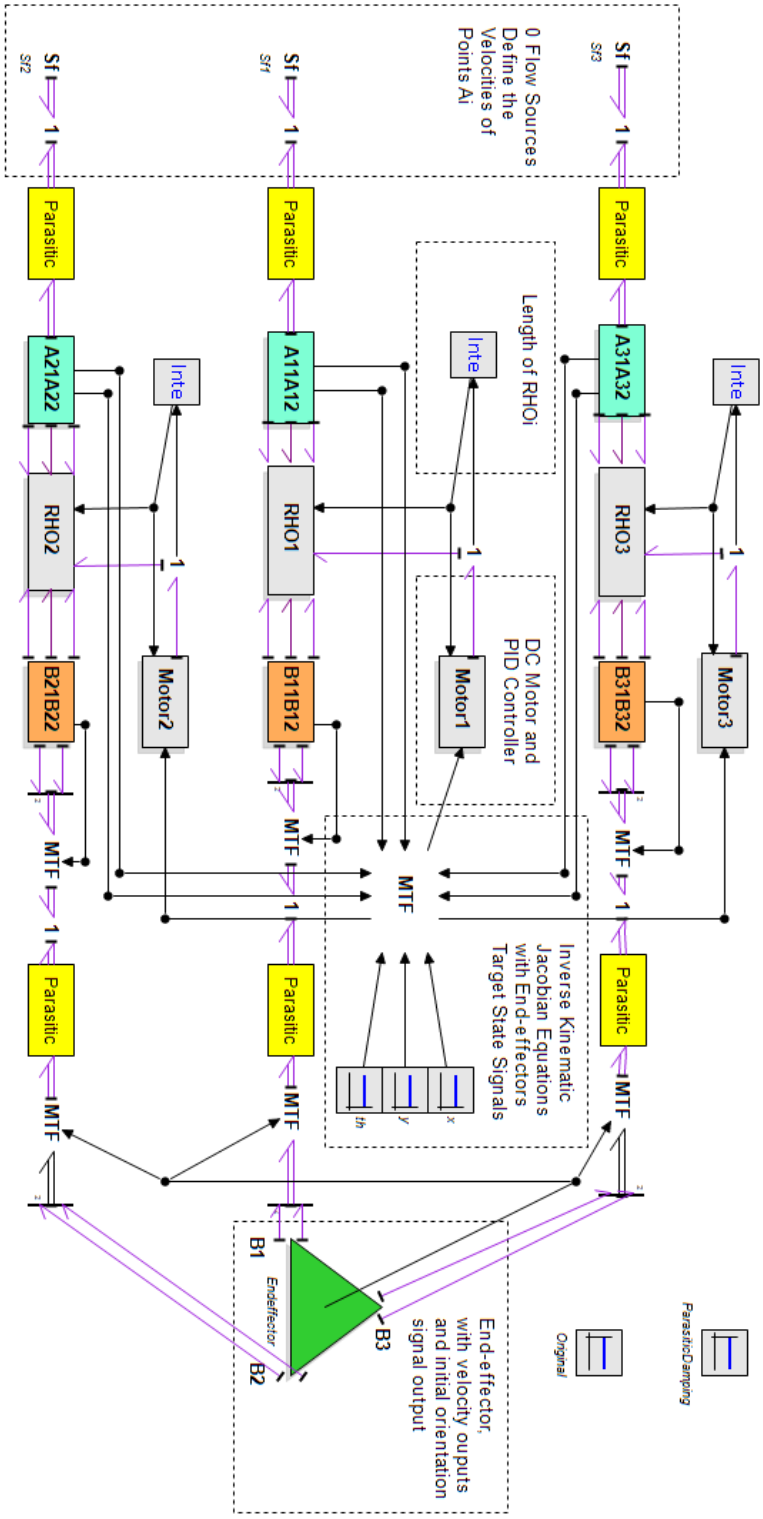

Figure 6.7: Overall bond graph

6.4 Initial Values for Kinematics Calculations

In order to simulate the movement in 20-sim, it is needed to set up initial values for every element. However, it is time consuming to calculate all passive initial values manually. For instance, the initial length of ρ_i is related to 8 parameters: moving platform's side length, initial position and orientation; length of l_i; length of l_{ri}; and the position of points A_i. It is significantly reasonable to calculate it with kinematic equations automatically. As a result, clarified kinematic relationship is essential for the dynamics simulation. The passive initial values which need calculation are as follow: the initial position and orientation of link l_i (G_{ix}, G_{iy} and $\mathrm{Oriegangle}_i$) the initial length of ρ_i; the initial position of link l_{ri} (G_{iix}, G_{iiy}).

6.4.1 Inverse Kinematic Equations

The "MTF" shown in the "Inverse Jacobian Equations" box of Figure 6.7, obtains moving platform's target position and orientation as inputs, calculating the target lengths for 3 ρ_i elements. In the 20-Sim code, use "endx", "endy", and "endo" representing initial state for moving platform (initial X position, initial Y position and initial orientation). On the other hand, use "x", "y", and "th" representing the target X position, Y position and orientation.

As the procedure in Chapter 4, calculate the position of B_i firstly; then obtain the length of ρ_i, which is equivalent to the Equation 4.10. From the Equation 4.10, the target lengths of ρi elements can be obtained with "x", "y", and "th". If change "x", "y", and "th" to "endx", "endy", and "endo", the initial length in each actuated segment can be got.

6.4.2 Initial Orientation of Each Link (th_i)

From Figure 6.1, it can be observed that the orientations of link l_i and l_{ri} are equal to each other. In order to avoid using 0 values while obtaining the angle through inverse trigonometric function, use "atan2" function to obtain the orientation of each link. For instance, the atan2 code in L_1 is used to get the initial orientation th1:

$$th_1 = atan2((\mathrm{B_{1y}} - \mathrm{A_{1y}}), (\mathrm{B_{1x}} - \mathrm{A_{1x}})) \tag{6.5}$$

The Equation 6.5 is based on the Equation 4.11 in Chapter 4. $\mathrm{B_{1y}}$ and $\mathrm{B_{1x}}$ come from the moving platform initial state: "endx", "endy", and "endo".

6.4.3 Initial Position of Each Link's Central Point

Use the symbols representing the initial positions for link l_i and l_{ri}: initial center point position of link l_i (G_{iX}, G_{iY}) and initial center point position of link l_{ri} (G_{iiX}, G_{iiY}), where i ranges from 1 to 3. The calculation is shown in Equation 6.6:

$$\begin{bmatrix} \mathrm{G_{iX}} \\ \mathrm{G_{iY}} \\ \mathrm{G_{iiX}} \\ \mathrm{G_{iiY}} \end{bmatrix} = \begin{bmatrix} \mathrm{A_{ix}} \\ \mathrm{A_{iy}} \\ \mathrm{B_{ix}} \\ \mathrm{B_{iy}} \end{bmatrix} + \begin{bmatrix} \cos(\mathrm{th}_i) * \mathrm{l_i}/2 \\ \sin(\mathrm{th}_i) * \mathrm{l_i}/2 \\ -\cos(\mathrm{th}_i) * \mathrm{l_{ri}}/2 \\ -\sin(\mathrm{th}_i) * \mathrm{l_{ri}}/2 \end{bmatrix} \tag{6.6}$$

All the initial parameters are needed to put into the bond graph before simulation are listed in Table 6.8 below. With the previous modeling, the initial state of the robot's end-effector can be changed within the workspace.

Table 6.8: Initial Parameters for Simulation

Initial Values				
Segment		**Name**	**Value**	**Unit**
Length		l_i	0.6	m
		l_{ri}	0.6	m
Ai	**A1**	A_{1X}	-0.15	m
		A_{1Y}	0.0866	m
	A2	A_{2X}	0.15	m
		A_{2Y}	0.0866	m
	A3	A_{3X}	0	m
		A_{3Y}	-0.1732	m
Initial Values				
Segment		**Name**	**Value**	**Unit**
Moving platform	**L_{MP}**	LMP	0.2	m
	Position	Endx	-0.15	m
		Endy	-0.15	m
	Orientation	Endo	0	rad
Target		x	-0.2	m
		y	-0.15	m
		th	0.2	rad

6.5 Bond Graph Simulation

After importing the required equations into the different bond graph blocks, the movement of the moving platform can be simulated. In the simulation, the motion of the robot end-effector center C in the local reference frame is concerned. The result is in the form of the animation.

- The initial parameters in Table 6.7 and 6.8 are introduced into the system, including the moving platform's side length L_{MP}. The Ai values can be changed in this reconfigurable manipulator from one task to another. But they will not be changed during one task.
- The required parameters are plotted in specific windows. There is no limitation to the number of variables in each window, as well as the number of windows.
- The simulation is launched.

Table 6.9: 3D animation result

Simulation Result	
Initial	**End**
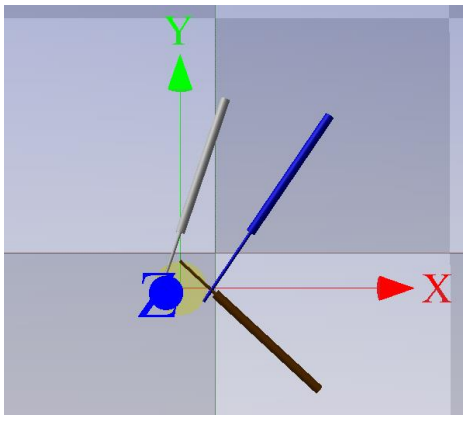	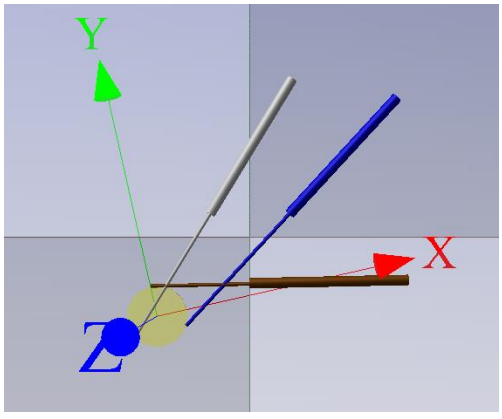

Using the 2D Animation figures in Table 6.9, it can be verified and confirmed that the model is valid for the 3-RPR manipulator. Moreover, it can be verified that the moving platform can move from the starting position to the target orientation.

6.6 Bond Graph Result

Any control algorithm can be successfully applied in the bond graph model.

In this study, there is one PID controller for each actuator with encoder at the leg level. However, they are not used in conjunction with a path controller, which is normally implemented in a real robot application. For the sake of the demonstration, I conducted that uncomplicated approach to show that control algorithm can be implemented in Bond Graph.

As a result, three plots are generated to check the dynamic performance and model validation. From Table 6.10, it can be observed that the moving platform can reach the target state even with these basic PID loops. Moreover, the control error levels can be plotted as illustrated in Table 6.12. The right column of Table 6.10 represents the input signals of three PID controllers at the joint level, where the target length shows the plus signal and the real length indicates the minus signal. It can be observed that three PID control loops reach the target position and orientation almost at the same time.

Table 6.10: Moving platform and link kinematic data during simulation

Moving Platform	Link Length
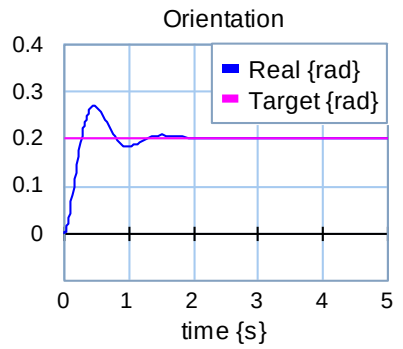	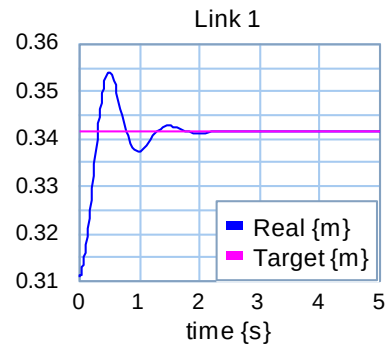
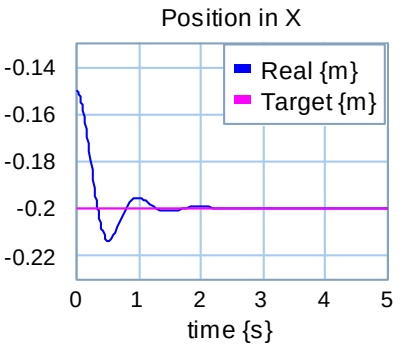	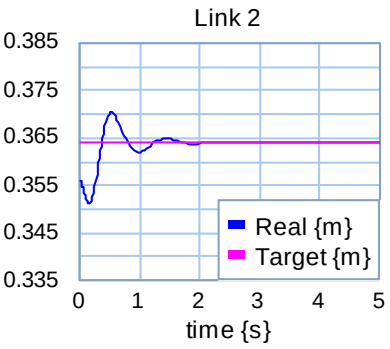
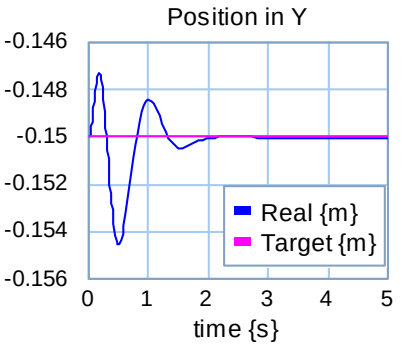	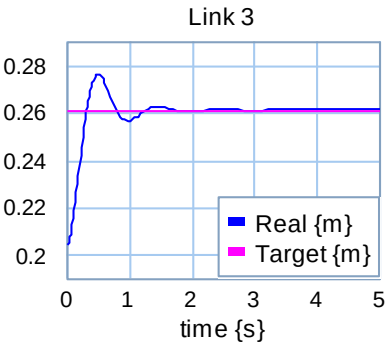

Table 6.11 provides the dynamic performance in plots: force applied to each link and the output torque of each motor. In the table, values of linear force range from -3.10 to 8.84N, on the other hand, values of passive torque range from -0.13 to 0.20 Nm.

Table 6.11: Dynamic data

Force in Links	Torque Output of Motors
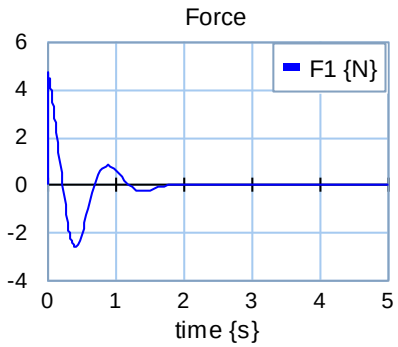	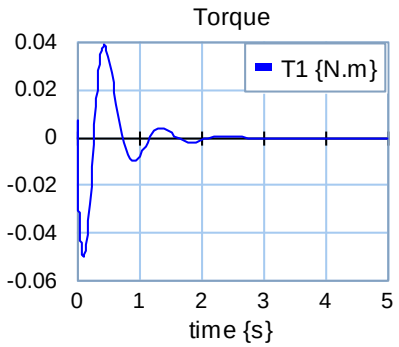
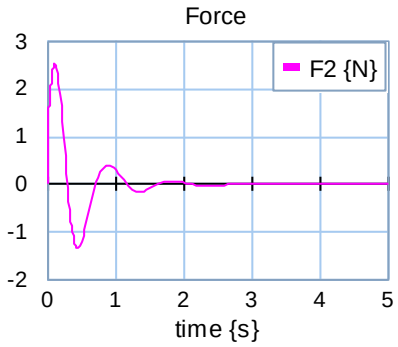	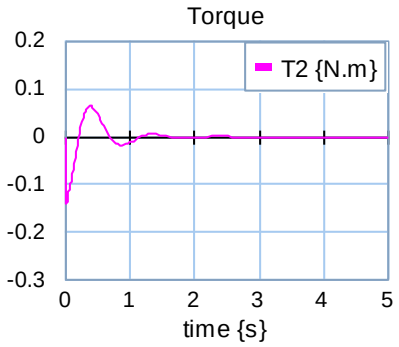
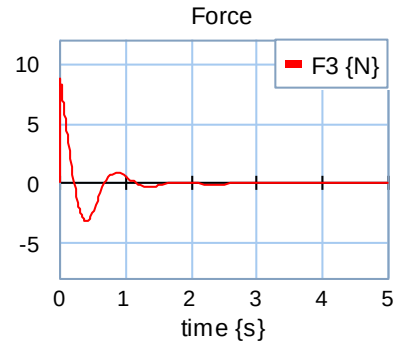	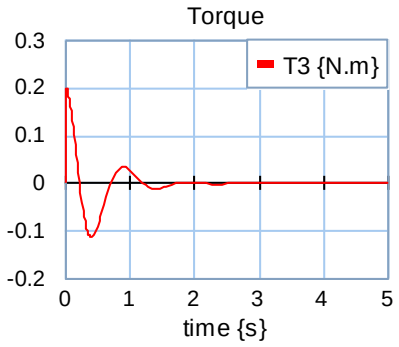

Table 6.12: Error analysis

	Moving Platform			Link		
	Orientation (rad)	**X (m)**	**Y (m)**	**ρ_1 (m)**	**ρ_2 (m)**	**ρ_3 (m)**
Initial	0	-0.15	-0.15	0.3109	0.3556	0.2043
End	0.2032	-0.1995	-0.1500	0.3416	0.3642	0.2614
Target	0.2	-0.2	-0.15	0.3415	0.3641	0.2613
Error	0.0032	0.0005	0.0000	0.0001	0.0001	0.0001
%	1.6%	3.3%	0.00%	0.03%	0.02%	0.05%

6.7 Virtual Work Principle

The general expression of the virtual work principle could be written as following:

$$\boldsymbol{\delta}_{\boldsymbol{q}}^{\boldsymbol{T}}\boldsymbol{\tau} + \boldsymbol{\delta}_{\boldsymbol{x_p}}^{\boldsymbol{T}}\hat{\mathbf{F}}_{\boldsymbol{p}} + \sum_i \boldsymbol{\delta}_{\boldsymbol{x_i}}^{\boldsymbol{T}}\hat{\mathbf{F}}_{\boldsymbol{i}} = 0 \tag{6.7}$$

Where "δ" represents the virtual displacements for each joint. In the inverse kinematic problem, the movement of the moving platform defines the virtual displacements of each joint. A six-dimensional wrench $\hat{\mathbf{F}}_{\boldsymbol{i}}$ is used to indicate the sum of applied force and inertia momentum about the center of mass in link i. For this planar robot, the first, the second and the sixth column will be applied to the Equation 6.7 in the end.

$$\hat{\mathbf{F}}_{\boldsymbol{i}} = \begin{bmatrix} \hat{\boldsymbol{f}}_{\boldsymbol{i}} \\ \hat{\boldsymbol{n}}_{\boldsymbol{i}} \end{bmatrix} \tag{6.8}$$

The detailed description for the $\hat{\boldsymbol{f}}_{\boldsymbol{i}}$, $\hat{\boldsymbol{n}}_{\boldsymbol{i}}$ and other variables can be found in the "Nomenclature" section. From that equation, generate a wrench for the moving platform:

$$\hat{\mathbf{F}}_{\boldsymbol{p}} = \begin{bmatrix} \hat{\boldsymbol{f}}_{\boldsymbol{p}} \\ \hat{\boldsymbol{n}}_{\boldsymbol{p}} \end{bmatrix} \tag{6.9}$$

Firstly, define the actuated joints displacements according to the inverse Jacobian matrix and velocity of the end-effector.

$$\boldsymbol{\delta_q} = J_p \boldsymbol{\delta}_{\boldsymbol{x_p}} \tag{6.10}$$

Secondly, displacement of any joint could be obtained with a similar method:

$$\boldsymbol{\delta}_{\boldsymbol{x_i}} = J_i \boldsymbol{\delta}_{\boldsymbol{x_p}} \tag{6.11}$$

In the end, substitute equations 6.10 and 6.11 into equation 6.7 to get the equation which describes the 3 RPR PPM dynamics:

$$J_p^T \boldsymbol{\tau} + \hat{\mathbf{F}}_{\boldsymbol{p}} + \sum_i J_i^T \, \hat{\mathbf{F}}_{\boldsymbol{i}} = 0 \tag{6.12}$$

6.7.1 Link Jacobian Matrix

Firstly, generate the Jacobian matrix for point B_i. Convert equation 5.14 into the matrix form to obtain the equation 6.13, where i ranges from 1 to 3.:

$$\boldsymbol{v_{bi}} = J_{bi} \dot{\boldsymbol{x}}_{\boldsymbol{p}} \tag{6.13}$$

The Jacobian matrix J_{bi} could be written in the following form:

$$J_{bi} = \begin{bmatrix} 1 & 0 & 0 & 0 & b_{iz} & -b_{iy} \\ 0 & 1 & 0 & -b_{iz} & 0 & b_{ix} \\ 0 & 0 & 1 & b_{iy} & -b_{ix} & 0 \end{bmatrix} \tag{6.14}$$

Then substitute equations 5.16 and 6.14 into equation 6.13. The equation 6.13 could be rewritten as equation 6.15:

$$^{i}\boldsymbol{v_{bi}} = {}^{i}J_{bi}\dot{\boldsymbol{x}}_{\boldsymbol{p}} = \begin{bmatrix} {}^{i}J_{bix} \\ {}^{i}J_{biy} \\ {}^{i}J_{biz} \end{bmatrix}\dot{\boldsymbol{x}}_{\boldsymbol{p}} \tag{6.15}$$

Where ${}^{i}J_{bi} = {}^{i}\mathrm{R_O}\ {}^{i}J_{bi}$. The variables in the matrix above are recorded as below:

$$\begin{cases} {}^{i}J_{bix} = [0 \quad 0 \quad -1 \quad -b_{iy} \quad b_{ix} \quad 0] \\ {}^{i}J_{biy} = [-\sin\theta_i \quad \cos\theta_i \quad 0 \quad -b_{iz}\cos\theta_i \quad -b_{iz}\sin\theta_i \quad b_{ix}\cos\theta_i + b_{iy}\sin\theta_i] \\ {}^{i}J_{biz} = [\cos\theta_i \quad \sin\theta_i \quad 0 \quad -b_{iz}\sin\theta_i \quad b_{iz}\cos\theta_i \quad b_{ix}\sin\theta_i - b_{iy}\cos\theta_i] \end{cases}$$

Because $\dot{L}_i = {}^{i}v_{biz}$ and $\dot{\boldsymbol{q}} = J_p\dot{\boldsymbol{x}}_{\boldsymbol{p}}$, the inverse Jacobian matrix J_p could be obtained below:

$$J_p = \begin{bmatrix} {}^{1}J_{b1z} \\ {}^{2}J_{b2z} \\ {}^{3}J_{b3z} \end{bmatrix} \tag{6.16}$$

Using the same method, rewriting the equations 5.18, 5.19 and 5.20 as following:

$$^{i}\boldsymbol{\omega_i} = \frac{1}{L_i}\begin{bmatrix} -\ {}^{i}J_{biy} \\ {}^{i}J_{bix} \\ 0 \end{bmatrix}\dot{\boldsymbol{x}}_{\boldsymbol{p}} \tag{6.17}$$

Once the angular velocity found, differentiate both sides of equations 5.12 and 5.13 to obtain the mass center velocity. The expressions are shown in equations 6.18 and 6.19.

$$^{i}\boldsymbol{v_{1i}} = -\frac{e_{i1}}{L_i}\begin{bmatrix} {}^{i}J_{bix} \\ {}^{i}J_{biy} \\ 0 \end{bmatrix}\dot{\boldsymbol{x}}_{\boldsymbol{p}} \tag{6.18}$$

$$ {}^{i}\boldsymbol{v}_{\mathbf{ri}} = \frac{1}{L_i}\begin{bmatrix} (L_i - e_{i2})\ {}^{i}J_{bix} \\ (L_i - e_{i2})\ {}^{i}J_{biy} \\ L_i\ {}^{i}J_{biz} \end{bmatrix}\dot{\boldsymbol{x}}_{\boldsymbol{p}} \tag{6.19} $$

Then combine equations 6.17, 6.18 and 6.19 to obtain the link Jacobian matrices, which are corresponding to the center of every two parts l_i and l_{ri}:

$$ {}^{i}\dot{\boldsymbol{x}}_{\mathbf{1}\boldsymbol{i}} = \begin{bmatrix} {}^{i}\boldsymbol{v}_{\mathbf{1}\boldsymbol{i}} \\ {}^{i}\boldsymbol{\omega}_{\boldsymbol{i}} \end{bmatrix} = {}^{i}J_{1i}\dot{\boldsymbol{x}}_{\boldsymbol{p}} \tag{6.20} $$

$$ {}^{i}\dot{\boldsymbol{x}}_{\boldsymbol{ri}} = \begin{bmatrix} {}^{i}\boldsymbol{v}_{\boldsymbol{ri}} \\ {}^{i}\boldsymbol{\omega}_{\boldsymbol{i}} \end{bmatrix} = {}^{i}J_{ri}\dot{\boldsymbol{x}}_{\boldsymbol{p}} \tag{6.21} $$

From the two equations above, it can be obtained the linear velocity and angular velocity of each part in one link. Furthermore, the link Jacobian matrix will contribute to the virtual displacement calculation in the next section.

$$ {}^{i}J_{1i} = \frac{1}{L_i}\begin{bmatrix} -e_{i1}\ {}^{i}J_{bix} \\ -e_{i1}\ {}^{i}J_{biy} \\ 0 \\ -\ {}^{i}J_{biy} \\ {}^{i}J_{bix} \\ 0 \end{bmatrix} \tag{6.22} $$

$$ {}^{i}J_{\mathrm{r}i} = \frac{1}{L_i}\begin{bmatrix} (L_i - e_{i2})\ {}^{i}J_{bix} \\ (L_i - e_{i2})\ {}^{i}J_{biy} \\ L_i\ {}^{i}J_{biz} \\ -\ {}^{i}J_{biy} \\ {}^{i}J_{bix} \\ 0 \end{bmatrix} \tag{6.23} $$

6.7.2 Inertia and Applied Wrenches

Once the Jacobian matrix is determined, the inertia and applied force are required to express Equation 6.12. Similarly to the six-dimensional vector $\boldsymbol{x_i}$, introduce the inertia and applied wrench vector in the virtual work principle equation. Firstly, assume that there is no force or torque applied to the moving platform. The only generated force is the inertia force exerted on the mass center. The inertia and applied wrench of the moving platform is indicated below:

$$\hat{\mathbf{F}}_{\boldsymbol{p}} = \begin{bmatrix} \hat{\mathbf{f}}_{\boldsymbol{p}} \\ \hat{\mathbf{n}}_{\boldsymbol{p}} \end{bmatrix} = \begin{bmatrix} m_p \boldsymbol{g} - m_p \dot{\boldsymbol{v}}_{\boldsymbol{p}} \\ -\,{}^{O}I_p \dot{\boldsymbol{\omega}}_{\boldsymbol{p}} - \boldsymbol{\omega}_{\boldsymbol{p}} \times \left({}^{O}I_p \boldsymbol{\omega}_{\boldsymbol{p}} \right) \end{bmatrix} \tag{6.24}$$

Where $\boldsymbol{g}$ is the gravity acceleration vector:$[0 \quad 0 \quad -9.81]^T$and ${}^{O}I_p = {}^{O}R_B \, {}^{B}I_p \, {}^{B}R_O$. The matrix ${}^{B}I_p$ is a diagonal matrix, which contains the rotational inertia along the axis within the reference frame B, the moving platform reference.

Similarly, generate the applied wrench for each part in link i:

$${}^{\boldsymbol{i}}\hat{\mathbf{F}}_{\mathbf{1}\boldsymbol{i}} = \begin{bmatrix} {}^{\boldsymbol{i}}\hat{\mathbf{f}}_{\mathbf{1}\boldsymbol{i}} \\ {}^{\boldsymbol{i}}\hat{\mathbf{n}}_{\mathbf{1}\boldsymbol{i}} \end{bmatrix} = \begin{bmatrix} m_{1i} \, {}^{i}R_O \boldsymbol{g} - m_{1i} \, {}^{i}\dot{\boldsymbol{v}}_{\mathbf{1}\boldsymbol{i}} \\ -\,{}^{i}I_{1i} \, {}^{i}\dot{\boldsymbol{\omega}}_{\boldsymbol{i}} - {}^{\boldsymbol{i}}\boldsymbol{\omega}_{\boldsymbol{i}} \times \left({}^{i}I_{1i} \, {}^{\boldsymbol{i}}\boldsymbol{\omega}_{\boldsymbol{i}} \right) \end{bmatrix} \tag{6.25}$$

$${}^{\boldsymbol{i}}\hat{\mathbf{F}}_{\boldsymbol{ri}} = \begin{bmatrix} {}^{\boldsymbol{i}}\hat{\mathbf{f}}_{\boldsymbol{ri}} \\ {}^{\boldsymbol{i}}\hat{\mathbf{n}}_{\boldsymbol{ri}} \end{bmatrix} = \begin{bmatrix} m_{ri} \, {}^{i}R_O \boldsymbol{g} - m_{ri} \, {}^{i}\dot{\boldsymbol{v}}_{\boldsymbol{ri}} \\ -\,{}^{i}I_{ri} \, {}^{i}\dot{\boldsymbol{\omega}}_{\boldsymbol{i}} - {}^{\boldsymbol{i}}\boldsymbol{\omega}_{\boldsymbol{i}} \times \left({}^{i}I_{ri} \, {}^{\boldsymbol{i}}\boldsymbol{\omega}_{\boldsymbol{i}} \right) \end{bmatrix} \tag{6.26}$$

Then substitute equations 6.24, 6.25 and 6.26 into equation 6.12 to obtain the overall virtual work equation below:

$$J_p^T \boldsymbol{\tau} + \hat{\mathbf{F}}_{\boldsymbol{p}} + \sum_{i=1}^{3} \left({}^{i}J_{1i}^T \, {}^{\boldsymbol{i}}\hat{\mathbf{F}}_{\mathbf{1}\boldsymbol{i}} + {}^{i}J_{ri}^T \, {}^{\boldsymbol{i}}\hat{\mathbf{F}}_{\boldsymbol{ri}} \right) = 0 \tag{6.27}$$

Compared with the Newton-Euler procedure, it is more efficient to use the virtual work principle as the joint constraint forces and moments are removed.

In this chapter, two dynamic analysis methods have been conducted: the bond graph approach, and the virtual work principle. The results from bond graph need to be verified with a dynamics method. In Chapter 6, there will be a comparison between the dynamic analysis results from bond graph on the 20-Sim program and virtual work principle on Matlab. Firstly compare the inverse kinematic results, which comprise lengths, velocity and acceleration of each link. Finally, evaluate the exerted actuator forces using both methods.

Chapter 7

Comparison between Bond Graph and Virtual Work Results

As two methods of dynamic analysis have been demonstrated, it would be essential to compare results from both approaches. In this chapter, the results will be assessed in four aspects: the leg length, linear velocity, linear acceleration and the inverse dynamic forces results in each joint from both methods. After the comparison, it can be observed that the results from bond graph and virtual work are almost as the same as each other.

7.1 Description of the Model for Comparison

As the simulation validation will be checked in this chapter, which is based on the position, velocity and acceleration of the moving platform, it is needed to use a different bond graph model for comparison. It is like an open loop control model. Define the movement path of the moving platform. Then check the response in each joint.

Firstly, use a “0 Joint” to represent the force in each joint, the flow of which comes from the velocity difference between l_i and l_{ri}. Compared with Figure 6.4, the actuated joint bond graph model is a bit different, which is shown in Figure 7.1 below.

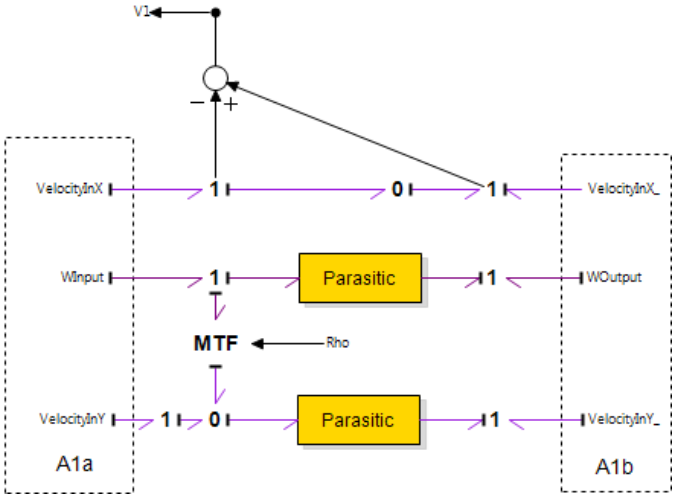

Figure 7.1: Actuated joint in the bond graph model for comparison

Define the orientation of the moving platform is constantly equal to zero during the simulation. The X position and Y position path are defined by Equation 7.1 and 7.2 below. They are two sine plots with time variable "t" as the input variable.

$$\mathrm{X}(t) = -0.25 + 0.05 * \sin(\pi * t) \tag{7.1}$$

$$\mathrm{Y}(t) = -0.15 + 0.05 * \sin(\pi * t) \tag{7.2}$$

The overall bond graph for dynamic comparison is shown in Figure 7.2 below; apply 2 position signals and differentiate them for moving platform's flow source. Within the Figure 7.1, differentiate the position formula 7.1 and 7.2 to obtain the linear velocity and acceleration of the moving platform. Then use "Parasitic Elements" in Table 6.2 to convert flow source into effort source.

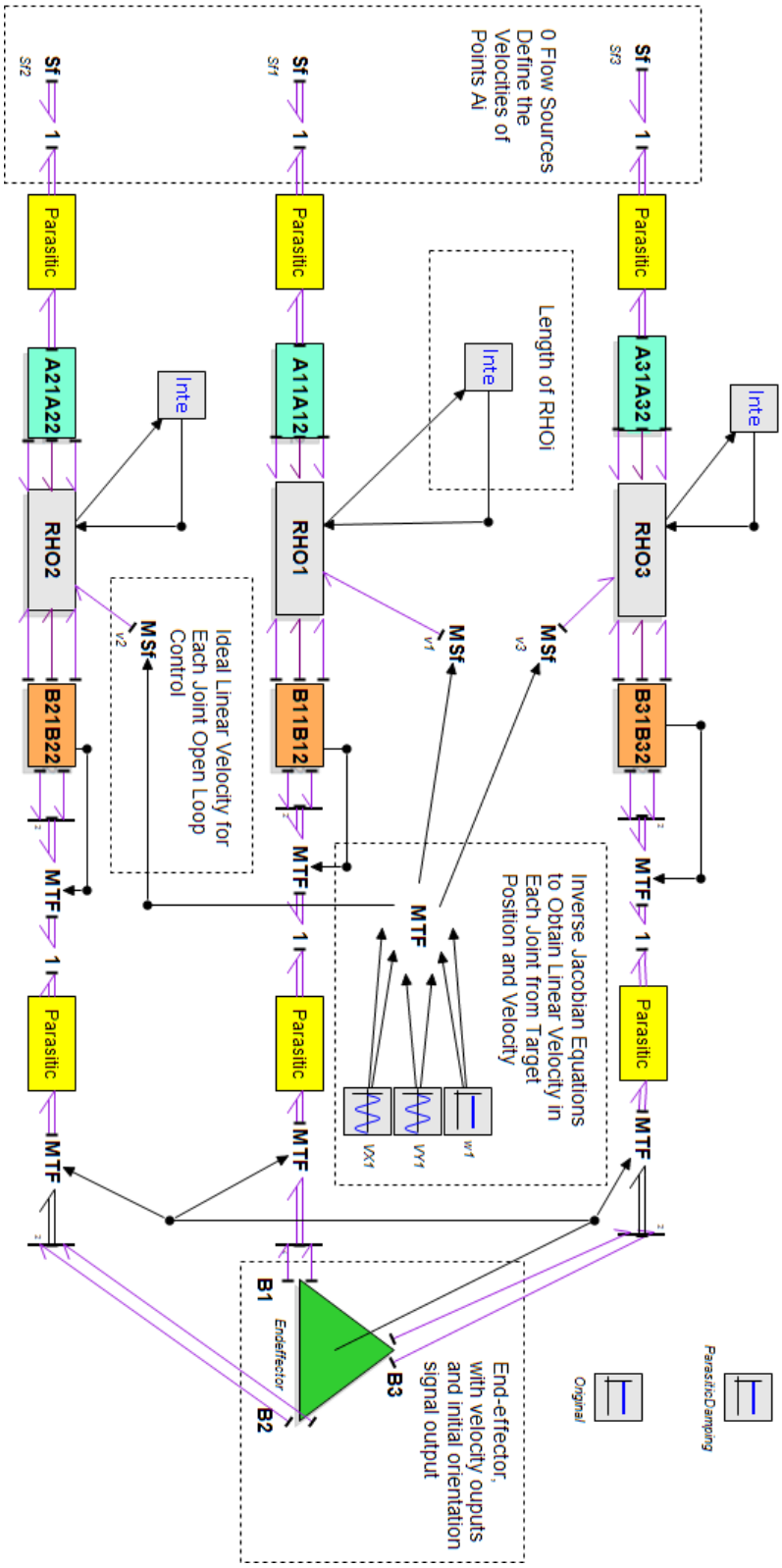

Figure 7.2: Overall bond graph system

Besides the parameters in Table 6.8, the other parameters used in the Bond Graph model are illustrated in Table 7.1. Consider each leg as a cylinder. According to the leg lengths and mass of each link, calculate the rotational inertia about the mass center.

Table 7.1: Inertia Parameters

Name	**L_i**		**L_{ri}**		**Moving Platform**	
Item	**Mass**	**Rotational Inertia**	**Mass**	**Rotational Inertia**	**Mass**	**Rotational Inertia**
Value	1	30038.01	1	30038.01	1.69935	11458.26
Unit	kg	$kg.mm^2$	kg	$kg.mm^2$	kg	$kg.mm^2$

The trajectory is shown in Figure 7.2. In the sections 7.2 to 7.5, a comparison between Bond Graph and virtual work results will be made according the movement.

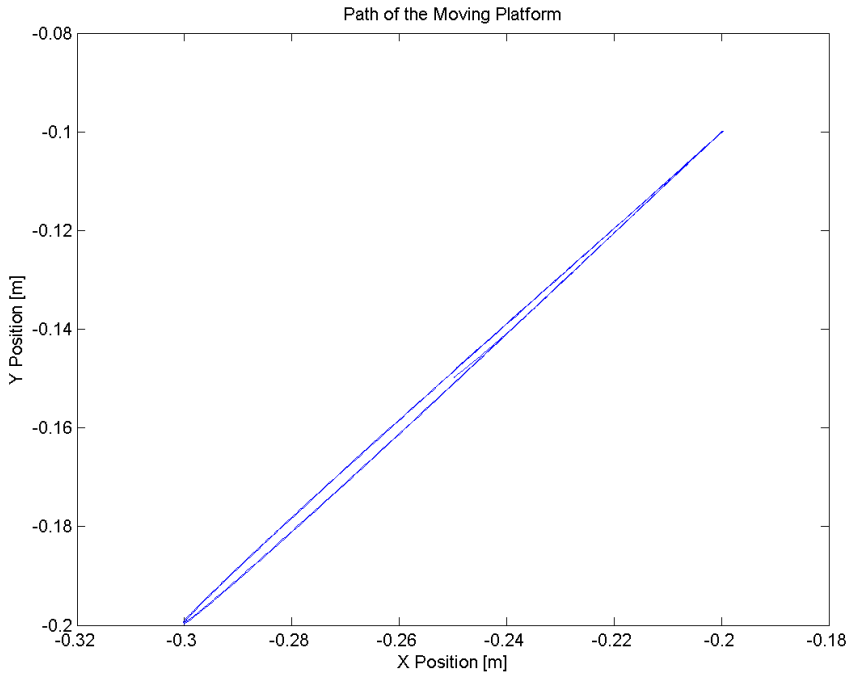

Figure 7.3: Moving platform trajectory

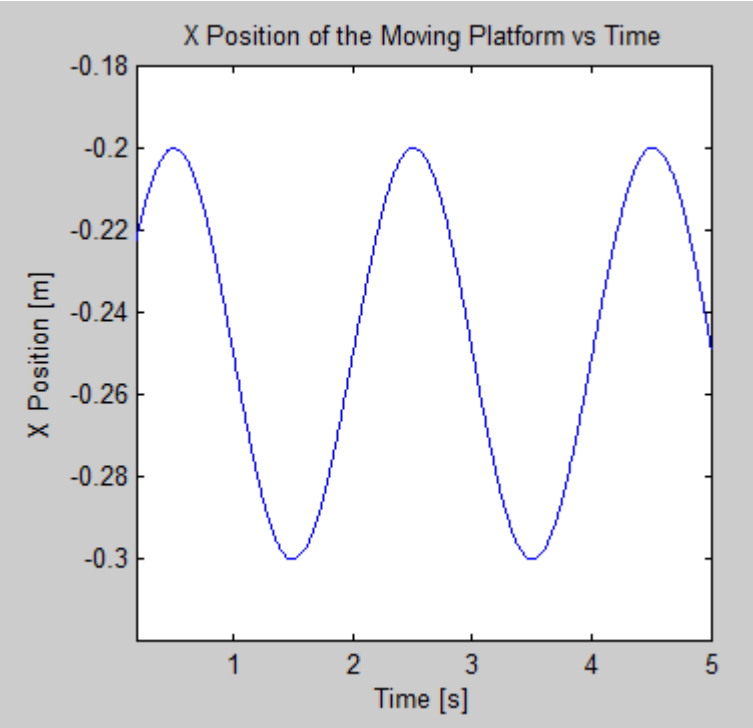

Figure 7.4: Moving platform position in X direction versus time

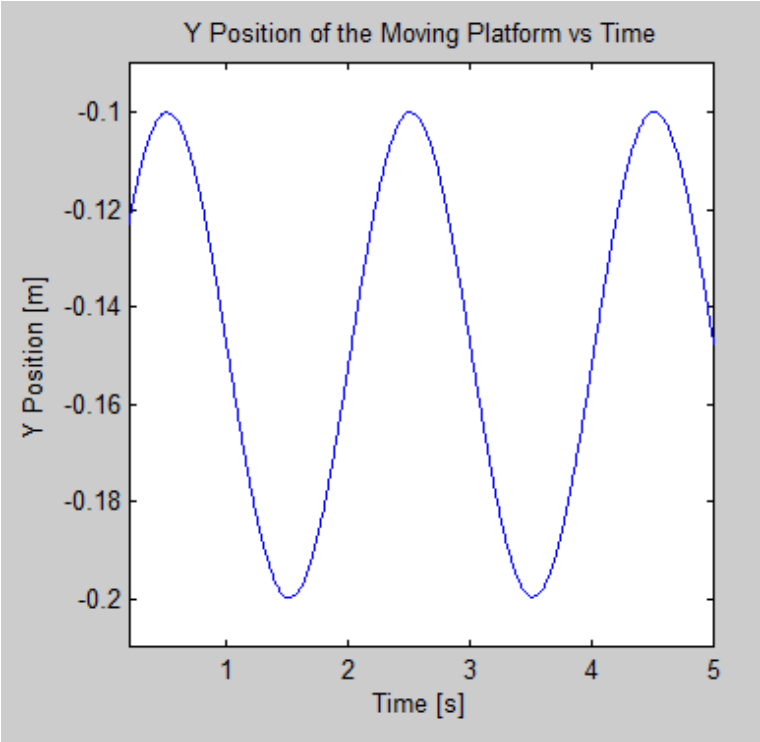

Figure 7.5: Moving platform position in Y direction versus time

7.2 Zero Order Results Comparison

The purpose of this comparison is to compare the leg length results in each joint A_iB_i from both methods. It can be considered as a zero order comparison. Firstly, use the Equations 7.1 and 7.2 as the input variable functions. Then plot the result from bond graph and the result from the kinematic equations of the virtual work in the same plot, which are Figure 7.5 to 7.7. From the three figures, it can be observed that the results are very close to each other.

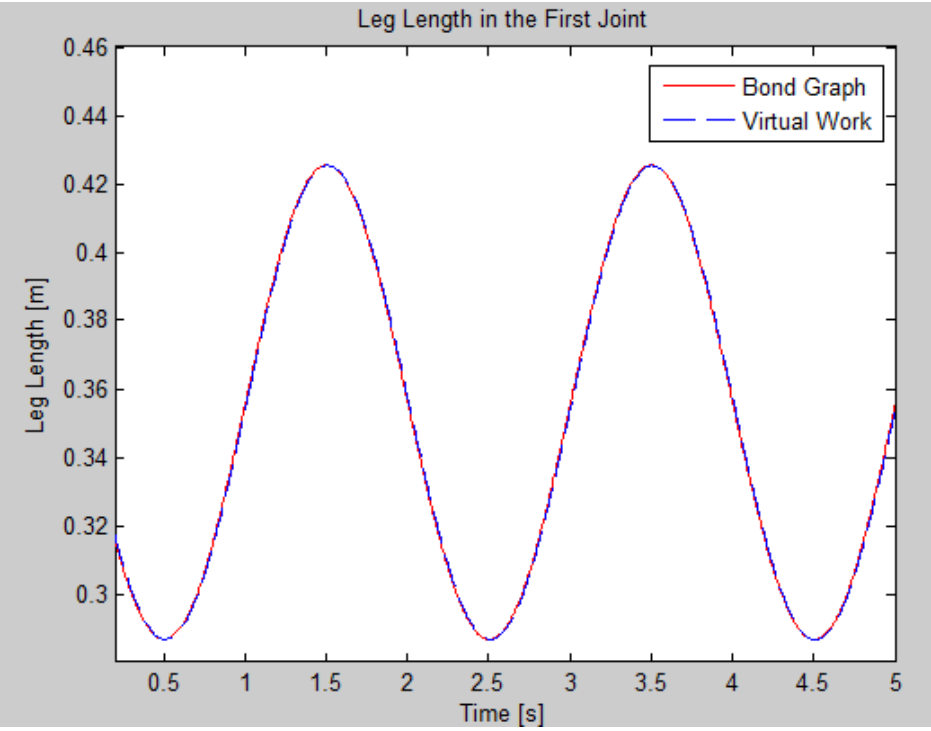

Figure 7.6: The comparison result of the leg length in the first joint

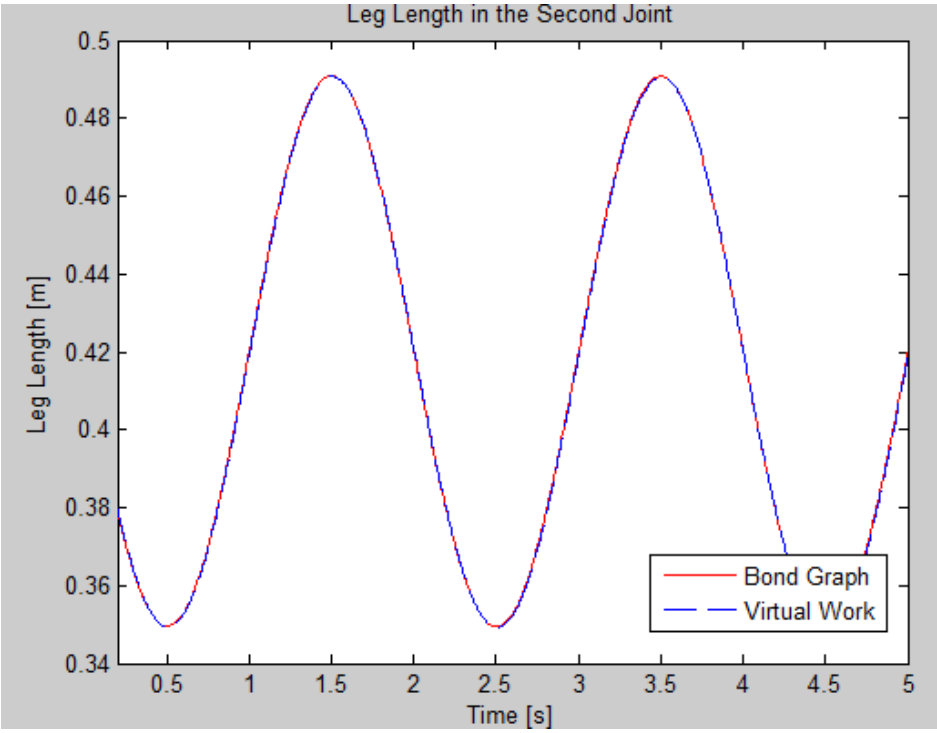

Figure 7.7: The comparison result of the leg length in the second joint

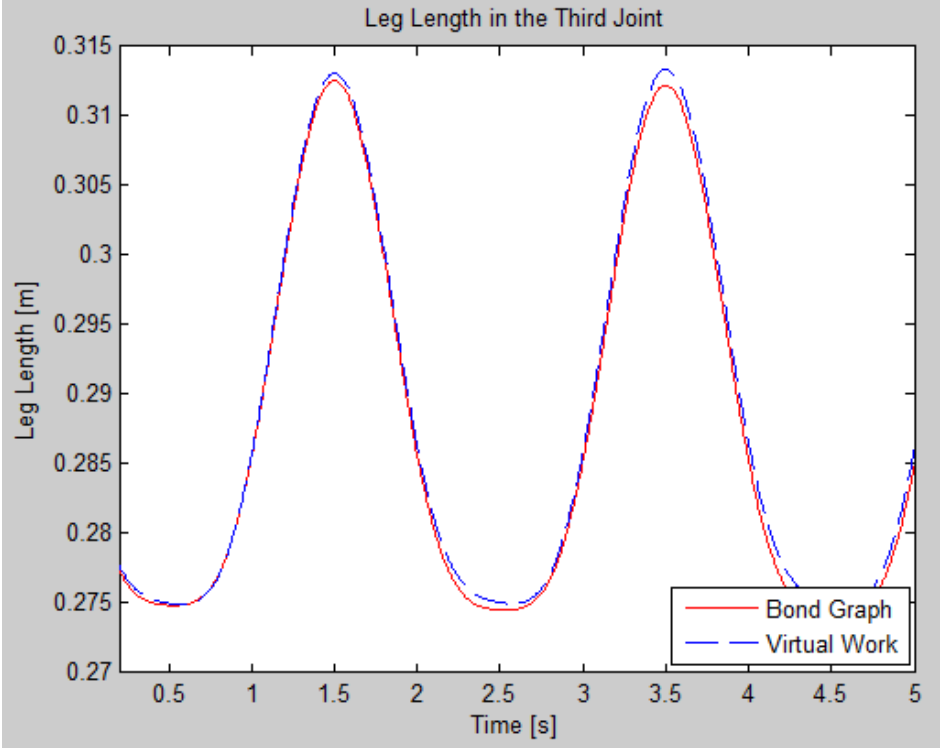

Figure 7.8: The comparison result of the leg length in the third joint

One step of the simulation is selected to put into Table 7.2 and 7.3 to give a numerical observation on the result.

Table 7.2: The input of zero order comparison

	Name	Virtual Work	Bond Graph
Input	**X**	-0.199860767 m	-0.199860767 m
	Y	-0.099947122 m	-0.099947122 m
	Φ	0.002107154 rad	0.002107154 rad

Table 7.3: The output of zero order comparison

	Name	Virtual Work Result	Bond Graph Result	Difference in Percentage
Output	**L_1**	0.309994594 m	0.308894878 m	0.35%
	L_2	0.372398991 m	0.371985265 m	0.11%
	L_3	0.276864985 m	0.27653423 m	0.12%

From the error analysis in Table 7.3, it can be observed that the error of bond graph is below 1% when calculating the zero order variables in the model. The result also matches the plots in Figures 7.6 to 7.8. From the result in Table 7.2 and 7.3, it can be seen in bond graph simulation, the leg lengths are very close to the virtual work results.

7.3 First Order Results Comparison

The purpose of this comparison is to compare the linear velocity results in each joint A_iB_i from both methods. It can be considered as a first order comparison. Firstly, use the position,

orientation, linear velocity and angular velocity of the moving platform as the input variables.

Then plot the result from bond graph and the result from the kinematic equations of the virtual work in the same plot, which are Figure 7.9 to 7.11. From the three figures, it can be observed that the results are very close to each other. One step of the simulation is selected to put into Table 7.4 and 7.5 to give a numerical observation on the result.

Table 7.4: The input of first order comparison

	Name	Virtual Work	Bond Graph
Input	**X**	-0.201162493 m	-0.201162493 m
	Y	-0.101246694 m	-0.101246694 m
	Φ	0.000315659 rad	0.000315659 rad
	$\dot{X}$	-0.036003875 m	-0.036003875 m
	$\dot{Y}$	-0.035723392 m	-0.035723392 m
	$\dot{\Phi}$	-0.021096238 rad/s	-0.021096238 rad/s

Table 7.5: The output of first order comparison

	Name	Virtual Work Result	Bond Graph Result	Difference in Percentage
Output	**$\dot{L}_1$**	-0.162204534 m/s	-0.159282211 m/s	1.80%
	$\dot{L}_2$	-0.163456366 m/s	-0.162241199 m/s	0.74%
	$\dot{L}_3$	-0.017791517 m/s	-0.017974343 m/s	1.03%

From the error analysis in Table 7.5, it can be observed that the error of bond graph is below 1% when calculating the first order variables in the model. The result also matches the plots in Figures 7.9 to 7.11. From the result, it can be seen in bond graph simulation, the results in each joint are very close to the virtual work results.

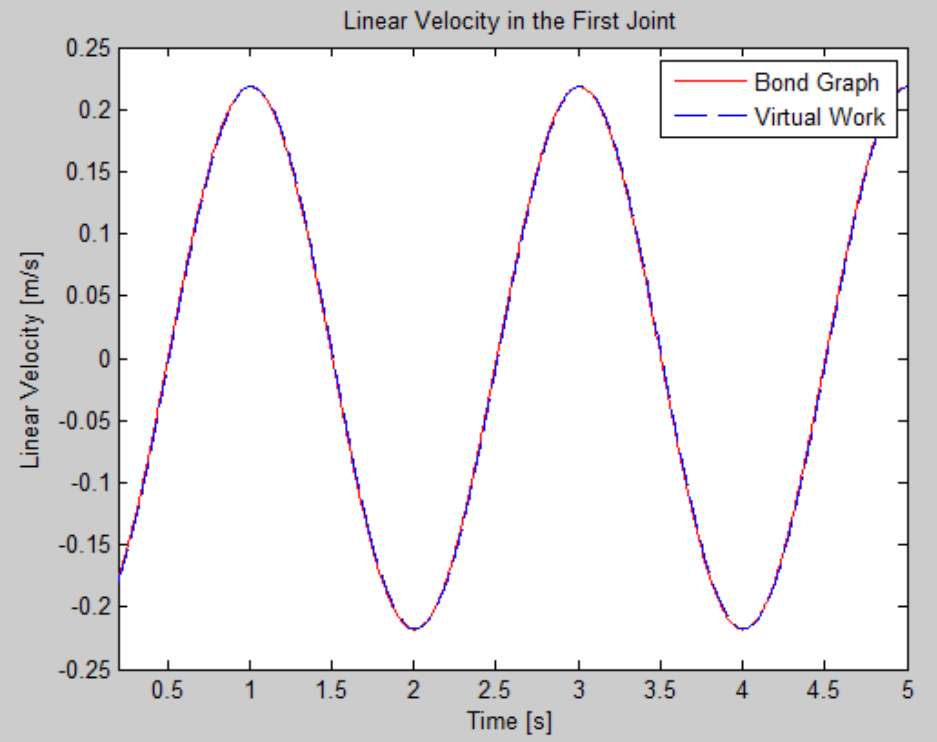

Figure 7.9: The comparison result of the velocity in the first joint

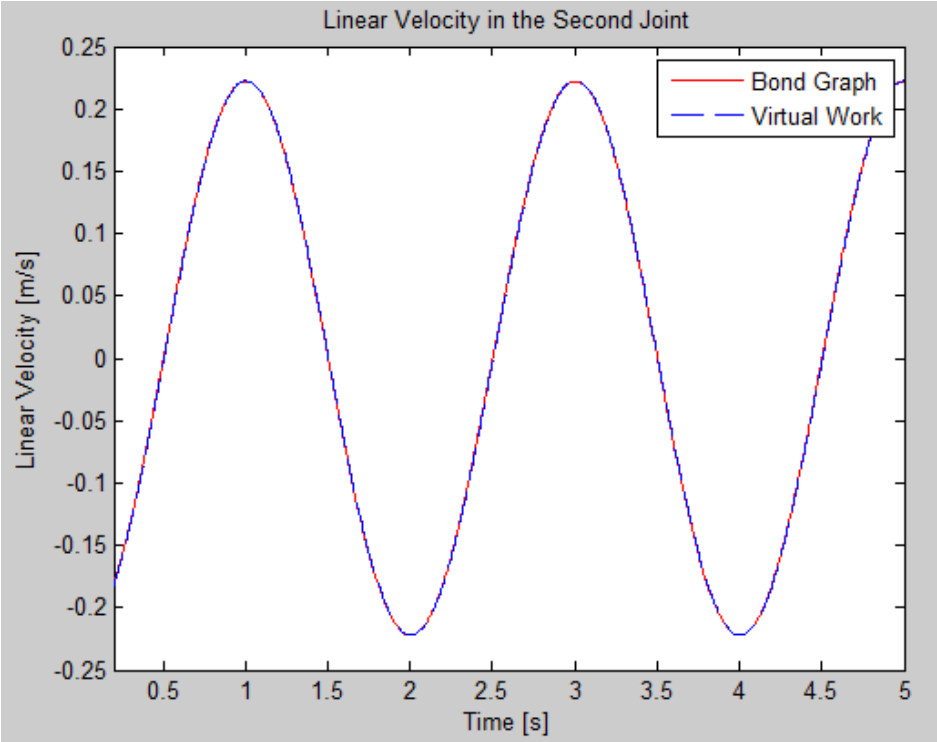

Figure 7.10: The comparison result of the velocity in the second joint

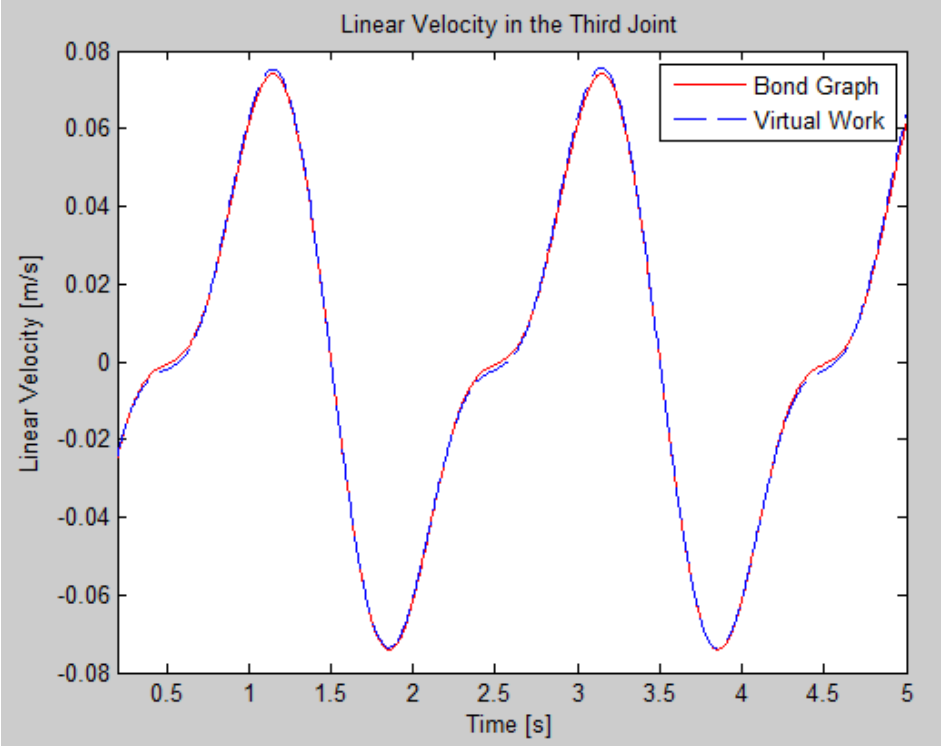

Figure 7.11: The comparison result of the velocity in the third joint

7.4 Second Order Results Comparison

The purpose of this comparison is to compare the linear acceleration results in each joint A_iB_i from both methods. It can be considered as a second order comparison. Firstly, use the position, orientation, linear velocity, angular velocity, linear acceleration and angular acceleration of the moving platform as the input variables.

Then plot the result from bond graph and the result from the kinematic equations of the virtual work in the same plot, which are Figure 7.11 to 7.13. From the three figures, it can be observed that the results are very close to each other. One step of the simulation is selected to put into Table 7.6 and 7.7 to give a numerical observation on the result.

Table 7.6: The input of second order comparison

	Name	Virtual Work	Bond Graph
Input	**X**	-0.211977034 m	-0.211977034 m
	Y	-0.111838589 m	-0.111838589 m
	Φ	-0.002510585 rad	-0.002510585 rad
	$\dot{X}$	-0.10379449 m/s	-0.10379449 m/s
	$\dot{Y}$	-0.100859661 m/s	-0.100859661 m/s
	$\dot{\Phi}$	-0.015443591 rad/s	-0.015443591 rad/s
	$\ddot{X}$	-0.387045453 m/s^2	-0.387045453 m/s^2
	$\ddot{Y}$	-0.366039409 m/s^2	-0.366039409 m/s^2
	$\ddot{\Phi}$	0.049577108 rad/s^2	0.049577108 rad/s^2

Table 7.7: The output of second order comparison

	Name	Virtual Work Result	Bond Graph Result	Difference in Percentage
Output	$\ddot{L}_1$	0.678478249 m/s^2	0.67814669 m/s^2	0.05%
	$\ddot{L}_2$	0.696504281 m/s^2	0.696886251 m/s^2	0.05%
	$\ddot{L}_3$	0.019889875 m/s^2	0.020457352 m/s^2	2.85%

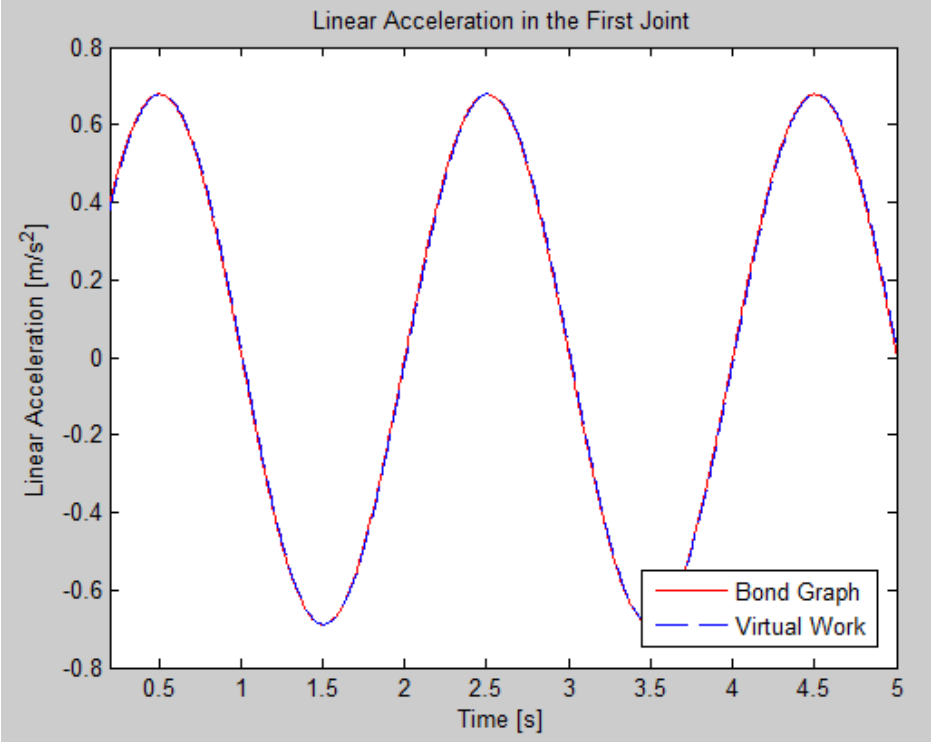

Figure 7.12: The comparison result of the acceleration in the first joint

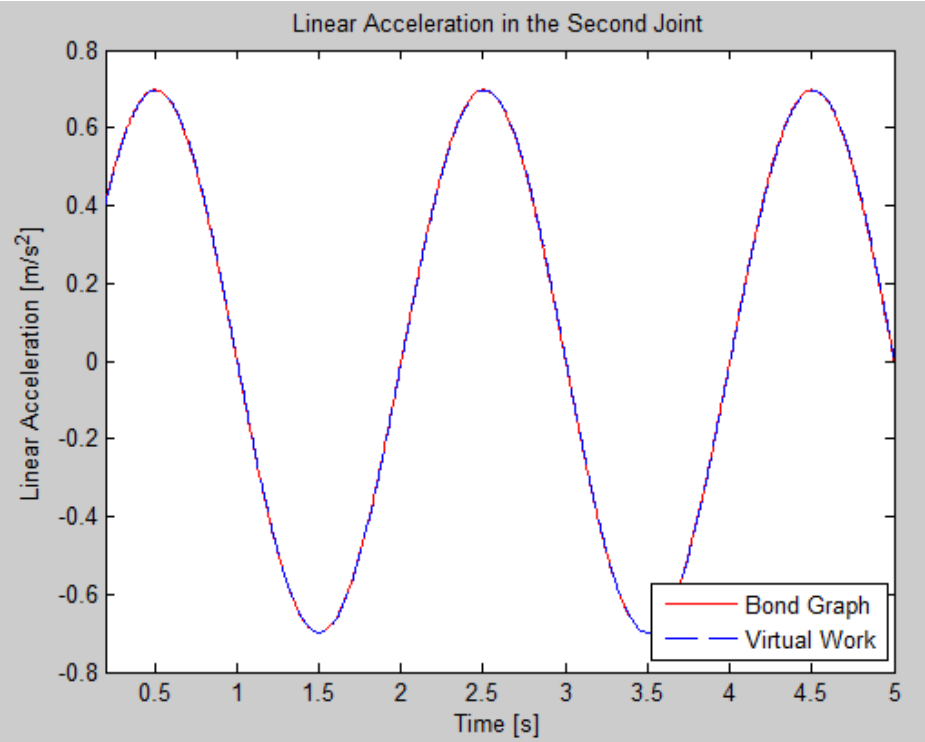

Figure 7.13: The comparison result of the acceleration in the second joint

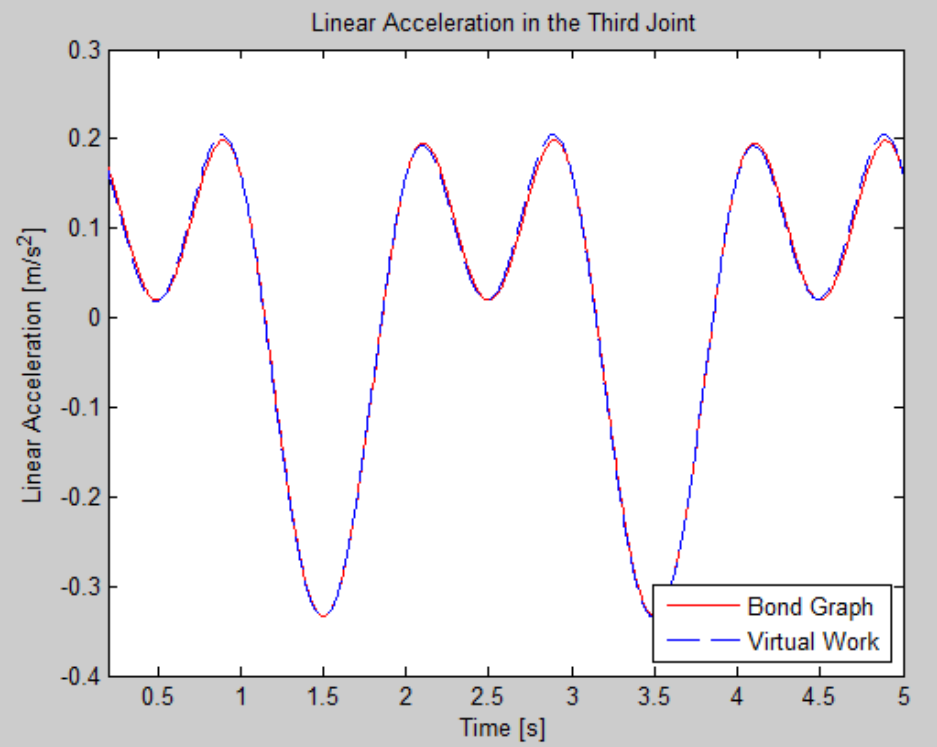

Figure 7.14: The comparison result of the acceleration in the third joint

From the error analysis in Table 7.7, it can be observed that the error of bond graph is below 1% when calculating the second order variables in the model. The result also matches the plots in Figures 7.12 to 7.14. From the result, it can be seen that the results in each joint from bond graph simulation are very close to the virtual work results.

7.5 Inverse Dynamic Comparison

In this section, the response force in each joint A_iB_i will be simulated. This is also the purpose of the virtual work principle, which is to calculate the inverse dynamic force according to the position, orientation, linear velocity, angular velocity, linear acceleration and angular acceleration of the moving platform.

Firstly use these variables as the inputs. Then compare the response force results from both methods. Then plot the result from bond graph and the result from the kinematic equations of the virtual work in the same plot, which are Figure 7.14 to 7.16.

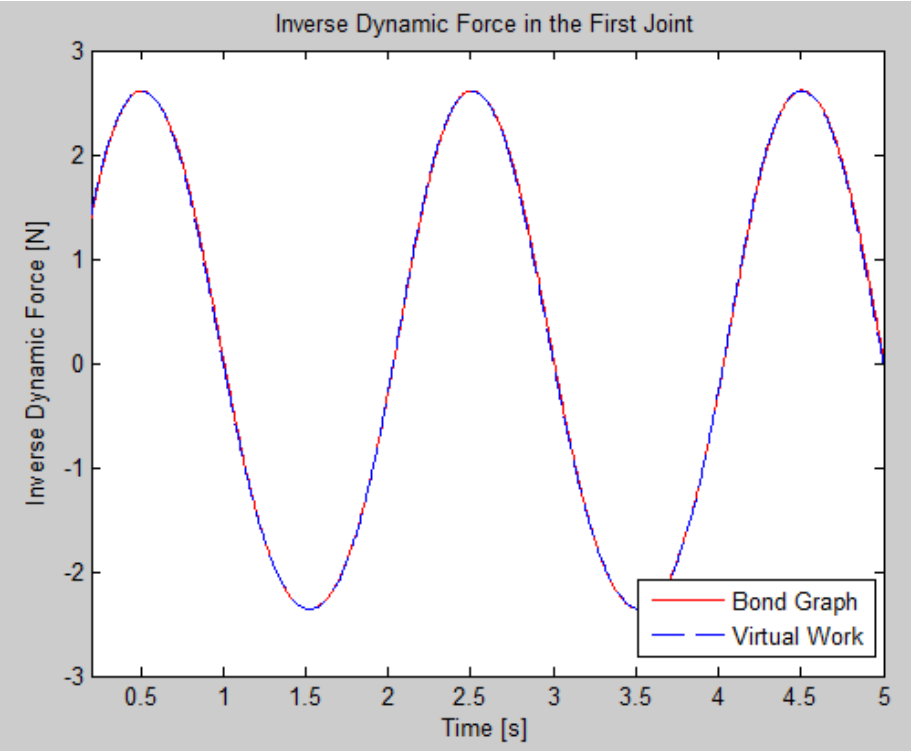

Figure 7.15: The comparison result of the inverse dynamic force in the first joint

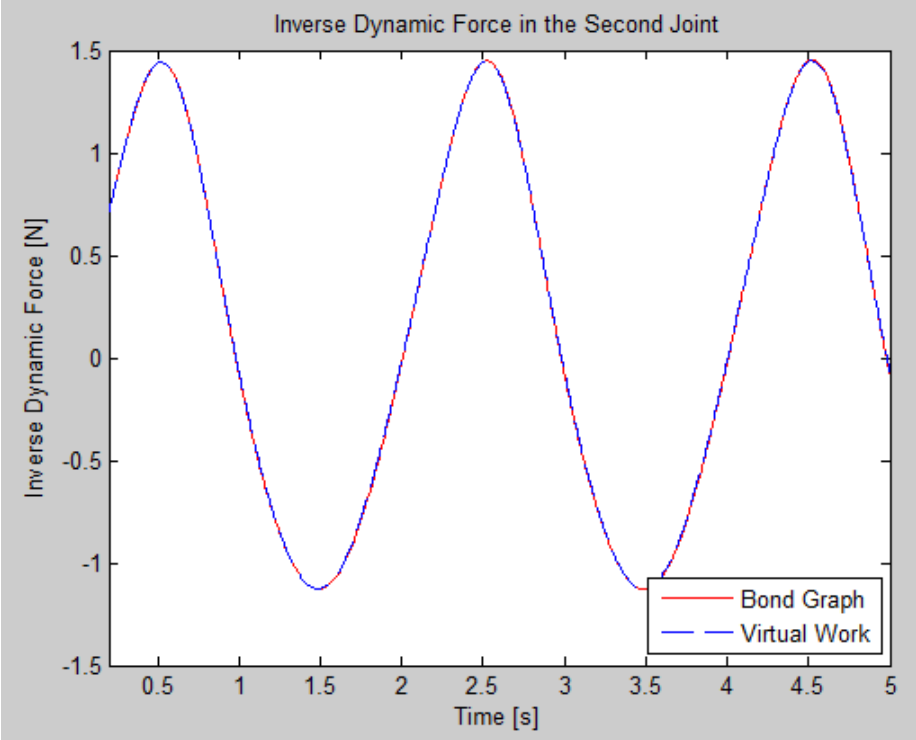

Figure 7.16: The comparison result of the inverse dynamic force in the second joint

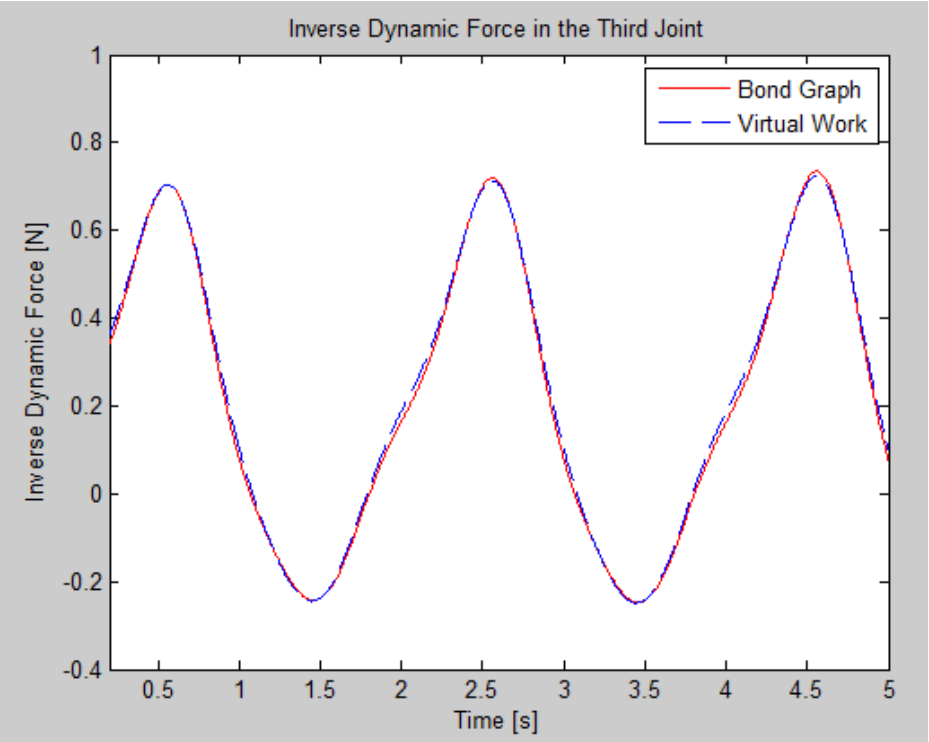

Figure 7.17: The comparison result of the inverse dynamic force in the third joint

Table 7.8: The input of inverse dynamic comparison

	Name	Virtual Work	Bond Graph
Input	**X**	-0.229339592 m	-0.229339592 m
	Y	-0.128625426 m	-0.128625426 m
	Φ	-0.004101348 rad	-0.004101348 rad
	$\dot{X}$	-0.145572075 m/s	-0.145572075 m/s
	$\dot{Y}$	-0.140400016 m/s	-0.140400016 m/s
	$\dot{\Phi}$	-0.007380645 rad/s	-0.007380645 rad/s
	$\ddot{X}$	-0.211556099 m/s^2	-0.211556099 m/s^2
	$\ddot{Y}$	-0.203258063 m/s^2	-0.203258063 m/s^2
	$\ddot{\Phi}$	0.066492619 rad/s^2	0.066492619 rad/s^2

Table 7.9: The output of inverse dynamic comparison

	Name	Virtual Work Result	Bond Graph Result	Difference in Percentage
Output	$\mathbf{F_1}$	2.610272368 N	2.610617157 N	0.01%
	$\mathbf{F_2}$	1.440588406 N	1.440333384 N	0.02%
	$\mathbf{F_3}$	0.693698204 N	0.693054774 N	0.09%

From the error analysis in Table 7.9, it can be observed that the error of bond graph is below 1% when calculating the inverse dynamic variables in the model. The result also matches the plots in Figures 7.15 to 7.17. From the result in Table 7.9, it can be seen, the results in each joint from bond graph simulation are very close to the virtual work results.

7.6 Conclusion

In this chapter, the comparison between the results from bond graph and virtual work has been conducted. After obtaining the position, velocity, acceleration and force outputs from both approaches, compare these data to observe how much the difference would be. It can be observed that bond graph could generate a reasonable result within each field.

Chapter 8

Robot Hardware Design for Construction

In this chapter, the design of 3-RPR PPM will be introduced, comprising the mechanical design and electrical hardware selection. Each manipulator component is analyzed and dimensioned.

The aim of this design step is to construct the robotic components and proceed with robot assembly. There are three sections in this chapter: the mechanical hardware design, the assembly design and the electrical hardware selection.

8.1 Mechanical Hardware Design

8.1.1 The Frame Design

The frame was designed to allow for the reconfiguration, where the revolute joints can be positioned and repositioned. The frame design is shown in Figure 8.1. use “T-Slotted Structural Aluminum Profiles” from Mini-Tec Framing System LLC. The part NO. is 20.1033.

The material of the framing bar is 6063-0 aluminum, of which the yield strength is 55.15 MPa. According to the weight of all the parts and the actuated force in each actuator, conduct the static analysis to the long bar. The frame is strong enough to support the whole system. The detailed description of the bending moment will be shown in the Section 8.1.2.

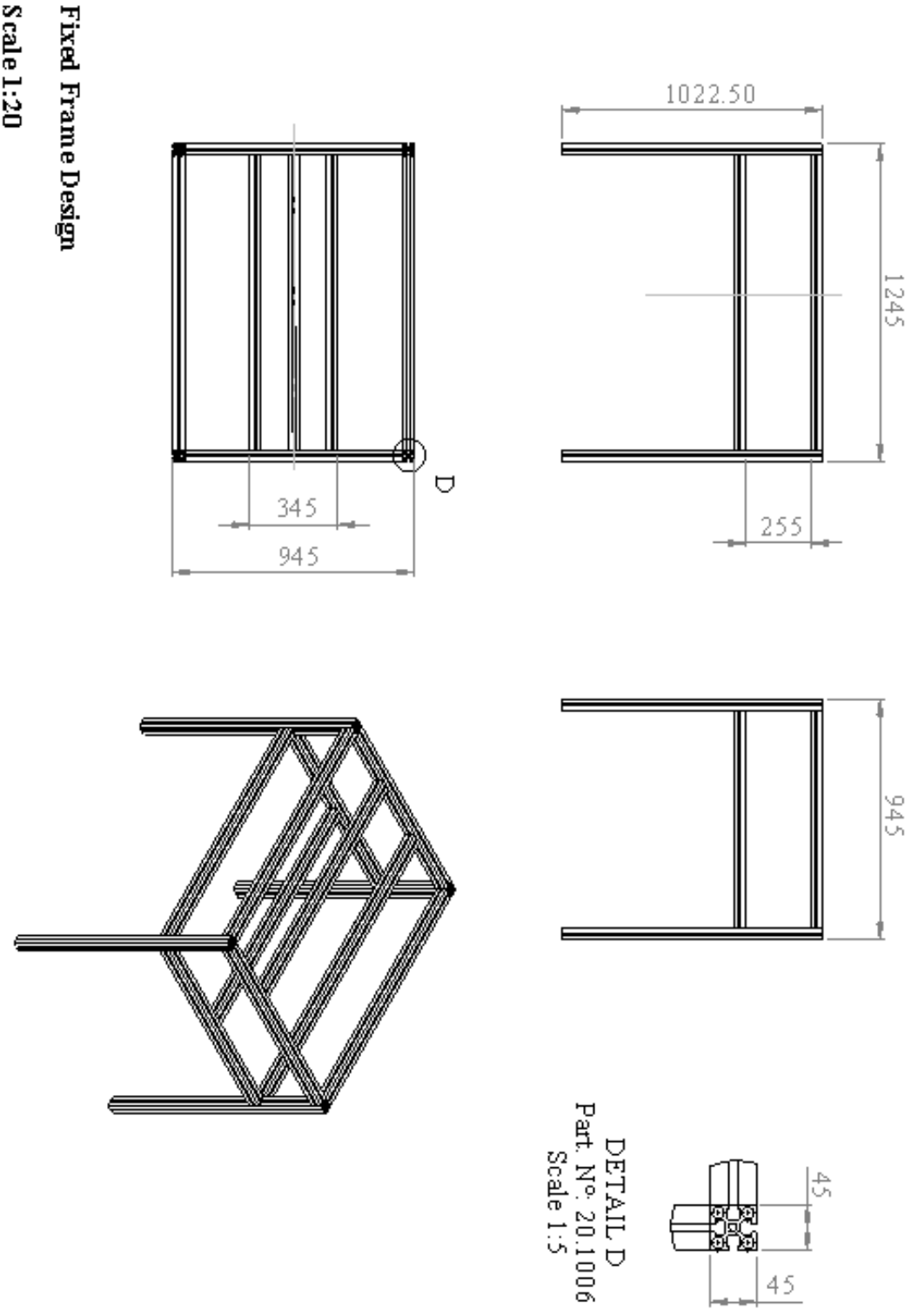

Figure 8.1: Fixed frame drawing

The static analysis result is shown in Figure 8.2. It can be observed that the frame is strong enough. The highest stress is 19.09 MPa, which is smaller than the yield strength.

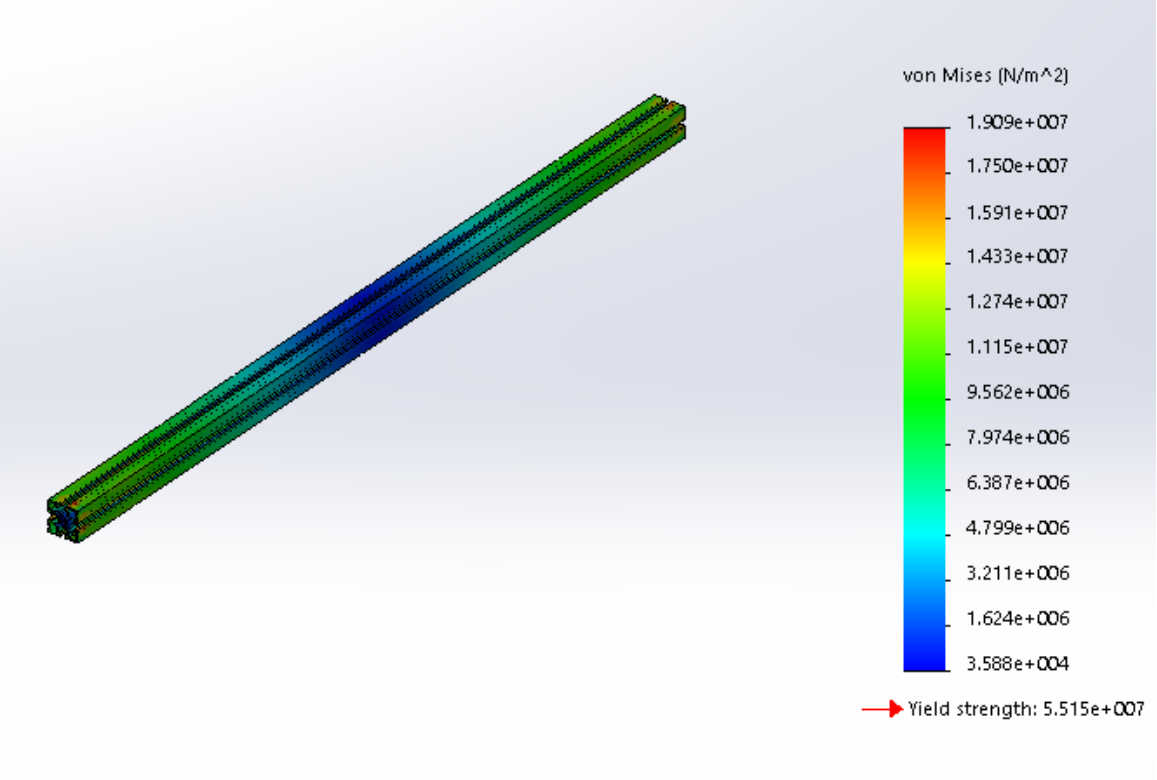

Figure 8.2: Frame static analysis result

8.1.2 The Fixed Joint Design

The shaft of the fixed base joint is named “Shaft” in Figure 8.3 overcoming the bending moment and horizontal force from the actuator. It is essential to calculate the highest bending moment and shear force distributed on the shaft. From that result, it can be obtained that the maximum stress and calculate the minimum allowable diameter of the shaft. It will be shown in this section as well. The other critical part is the clamp connecting the linear actuator to the fixed joint. The verification of its thickness will be shown in the section 8.1.5.

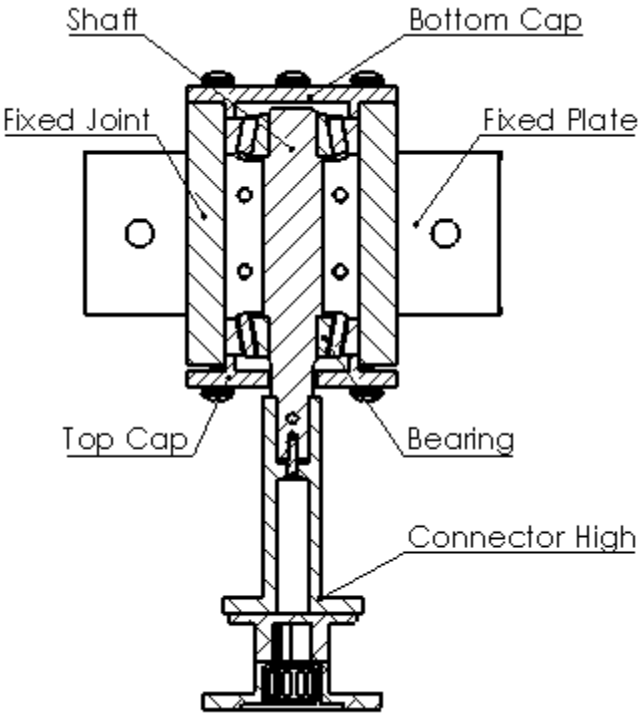

Figure 8.3: Fixed joint assembly

Firstly, generate the sketch for static analysis. According to the mass of moving platform: 3 kg and the mass of the linear actuator: 4kg, there will be a 17.37 Nm bending moment applied on the part when the linear actuator is fully extended, the center of which is 63 mm from the top of shaft (Please check the table 8.1 and Figure 8.4). Additionally, there is a maximum 100 N force horizontally applied on the same point. The sketch graph is shown in Figure 8.4.

Table 8.1: Bending Moment Calculation

Mass of Motor: 2 kg	**Mass of Rod: 1 kg**	**Mass of Cylinder: 1 kg**
Bending Moment Value when the Moving Platform is in the Closest Position to the Fixed Joint		
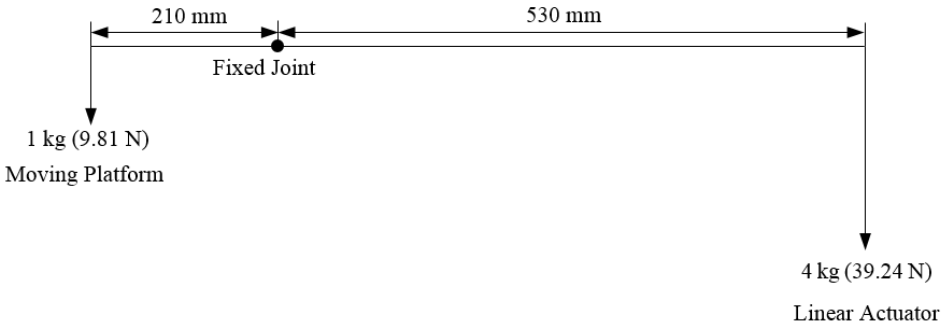		M = 17.27 Nm
Bending Moment Value when the Moving Platform is in the furthest position to the Fixed Joint		
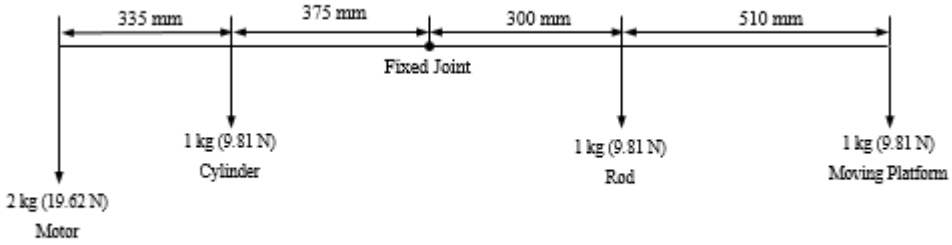		M = 5.24 Nm

From the bending moment calculation shown in Table 8.1, it can be observed that the shaft will overcome more bending moment when the moving platform gets closer to the fixed joint. The highest bending moment occurs when the distance between two parts is the lowest. Figure 8.9 is the sketch of the highest external forces and bending moment applied on the shaft. The calculation is achieved when the end-effector penalizing the system with

a larger moment. In terms of the fixed joint bearings, 15 mm diameter thrust bearing is selected for supporting the manipulator in the middle, because this kind of bearing could overcome more force than the regular ones. There is a certain distance, 65 mm, between the two bearings on the shaft. The center of two bearings is where the forces F1 and F2 applied. Choose this distance as the two bearings can overcome the bending moment.

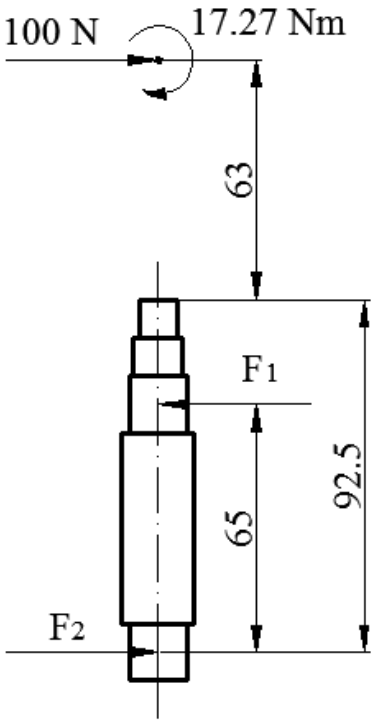

Figure 8.4: Sketch of the force and bending moment applied on the shaft

From the equations 8.1 and 8.2, obtain the values of F_1 and F_2 in Figure 8.9.

$$100 * (63 + 92.5) * 10^{-3} + 17.27 - F_1 * 65 * 10^{-3} = 0 \quad (8.1)$$

$$100 * (63 + 92.5 - 65) * 10^{-3} + 17.27 - F_2 * 65 * 10^{-3} = 0 \quad (8.2)$$

$$F_1 = 504.92\ N;\ F_2 = 404.92\ N$$

According to the force values, generate the bending moment distribution diagram in Figure 8.5. It can be seen that the bending moment increases along the shaft downwards and reaches the highest value at the point F_1, which is 26.32 Nm.

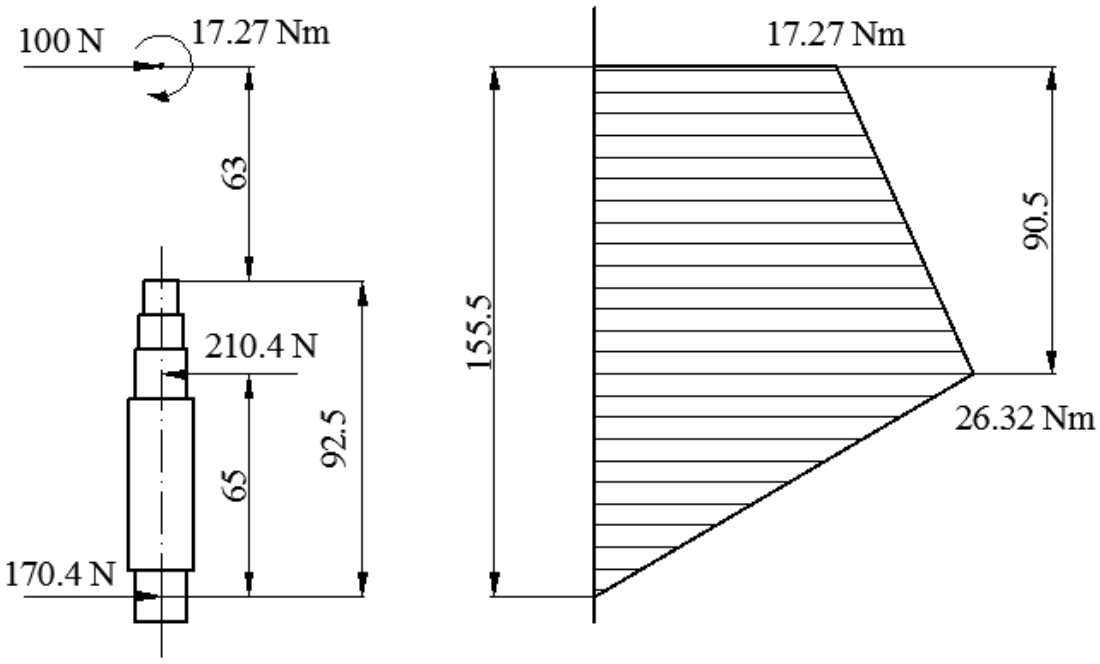

Figure 8.5: Bending moment distribution diagram

From the static analysis result above, it is observed that the position of F_1 is the section with the highest loading applied, where it is needed to calculate the minimum allowable diameter for the shaft. From the same bending moment and external forces applied to the shaft, the minimum allowable thickness for the clamps attached to the linear actuator will be calculated next.

Use equivalent bending moment equations to obtain the highest stress applied on the shaft, which is the most important part in the object. Three shafts overcome the highest stress

from bending in the mechanical system. From that stress value, calculate the minimum diameter of each shaft and choose the appropriate diameter size.

According to reference [34], applied the equivalent bending moment equation to obtain the minimum allowable shaft diameter. The maximum bending moment on the shaft is 26.32 Nm and the maximum torque applied on it is 2 Nm. From the Equation 8.3, the equivalent bending moment is 26.36 Nm.

$$M_e = \frac{1}{2}\left(M + \sqrt{M^2 + T^2}\right) \tag{8.3}$$
$$M_e = 26.36\ Nm$$

According to reference [43], the permissible tensile stress may be taken as 60% of the elastic limit in tension (σ_{el}), but not more than 36% of the ultimate tensile strength (σ_u). In other words the permissible tensile stress comes from equation 8.4, which is selected as the lowest value.

$$[\sigma] = \min[0.6 * \sigma_{el},\ 0.36 * \sigma_u] \tag{8.4}$$
$$[\sigma] = 210\ \text{MPa}$$

Furthermore, the diameter of shaft should meet the requirement in equation 8.5:

$$\text{d} \geq \sqrt[3]{(32 * M_e)/(\pi * [\sigma])} \tag{8.5}$$
$$\text{d} \geq 10.9\ \text{mm}$$

According to the result in equities, set the diameter of the shaft at the F_1 as 15 mm, with a safety margin of 50%.

Use Solidworks the Simulation toolbox to observe what the maximum displacement and stress are on the shaft, when the bending moment, external force and torque are applied. The maximum displacement will be 0.16 mm; in addition, the highest stress will be 134.3 MPa. These confirm that our mechanical design has met the strength requirement. The Solidworks simulation results are shown in Figure 8.6 and 8.7.

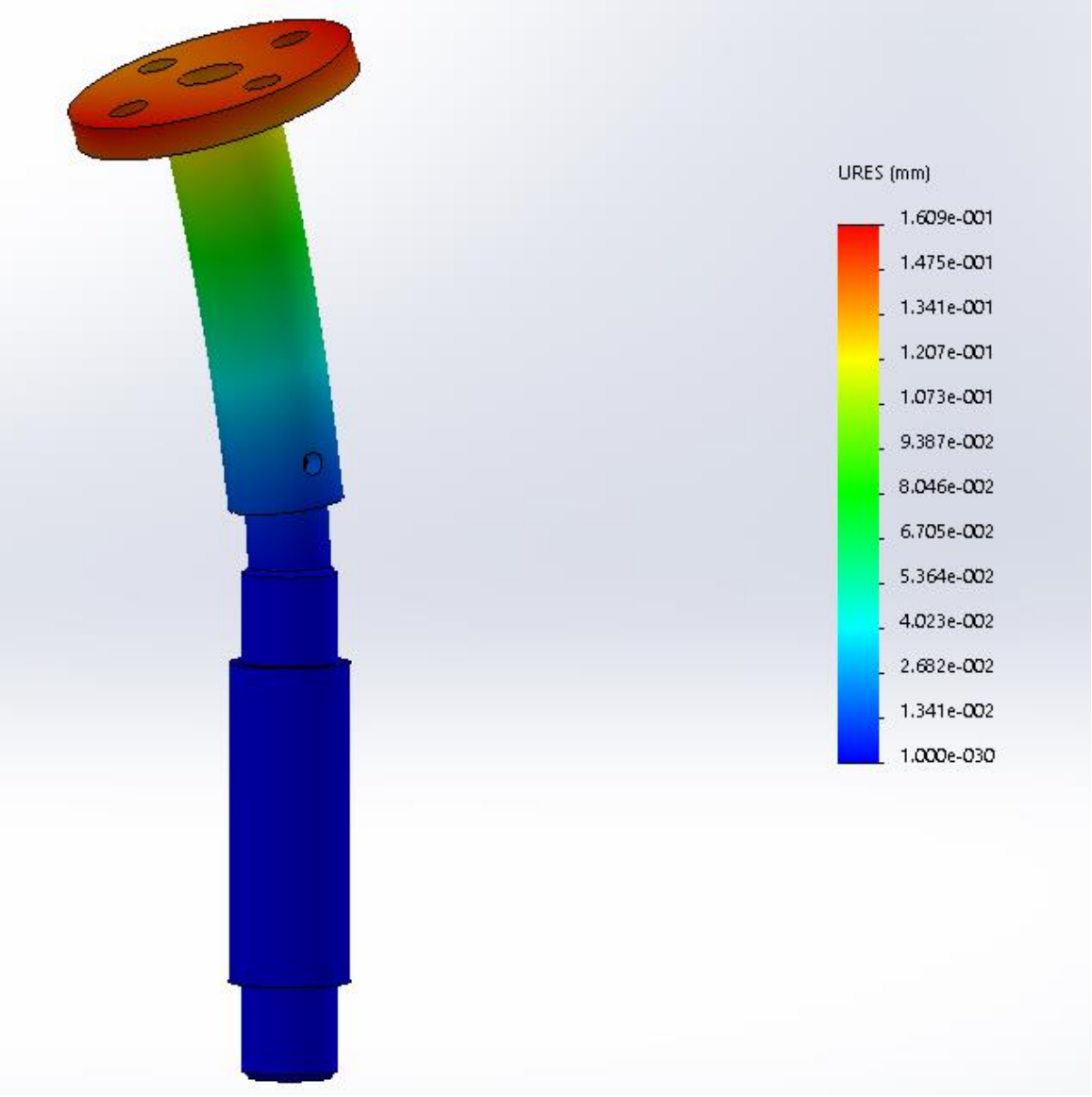

Figure 8.6: Displacement distribution due to external loads

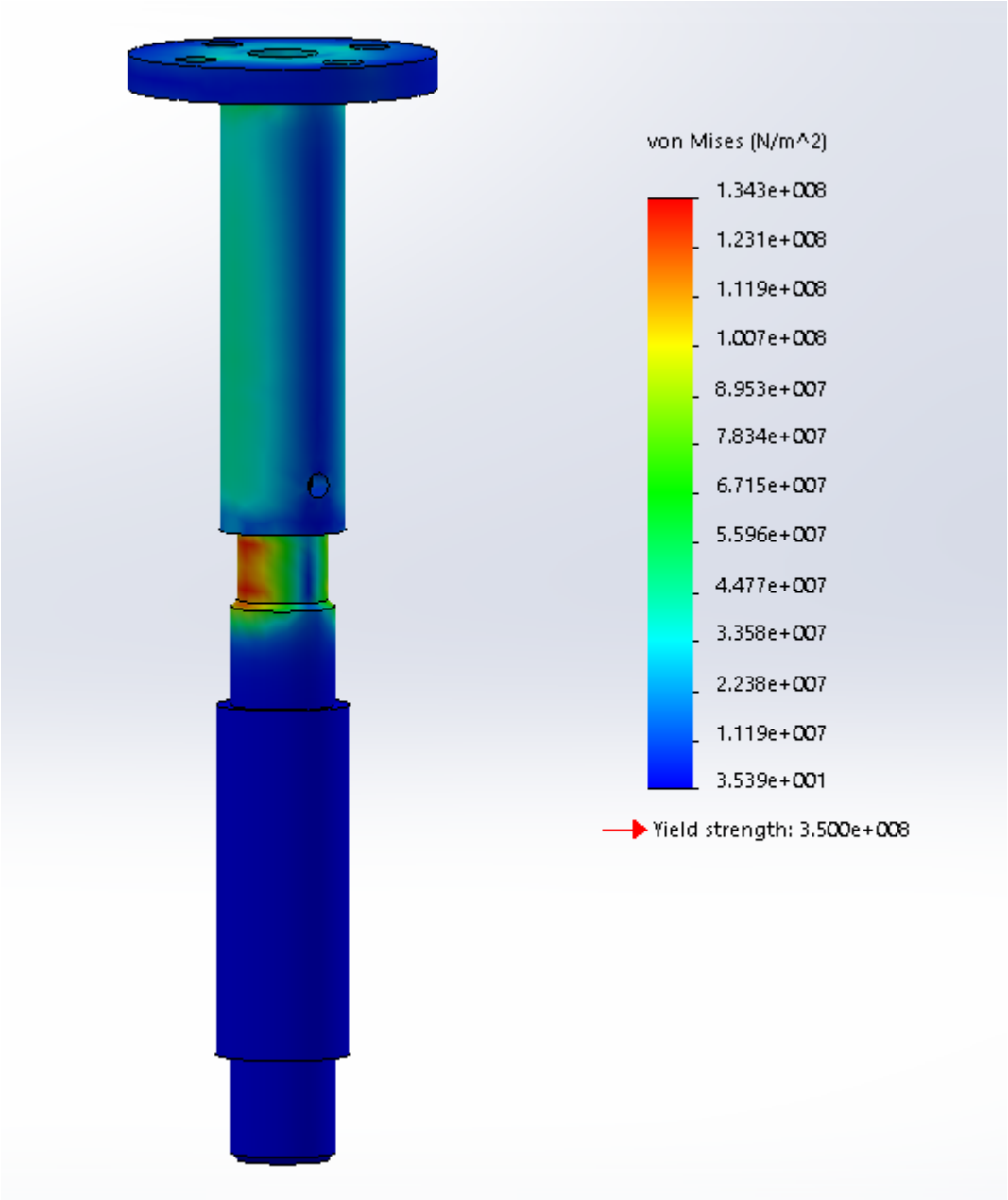

Figure 8.7: Stress distribution due to external load

From Figure 8.7, it can be seen that the highest stress applied on the shaft is 134.3 MPa, which is less than the permissible tensile stress 210 MPa.

8.1.3 The Moving Platform Design

The shape of the moving platform is an equilateral triangle. There are three sets of four M3 screws for the platform revolute joints assembly. As these thread holes going through the platform, the revolute joints can be located on the top of the platform or beneath the platform. With this design, the “cross-leg” configuration could be applied to the moving platform without collision between two linear actuators. The assembly drawing will be shown in the section 8.2. The moving platform drawing is shown in the Figure 8.8.

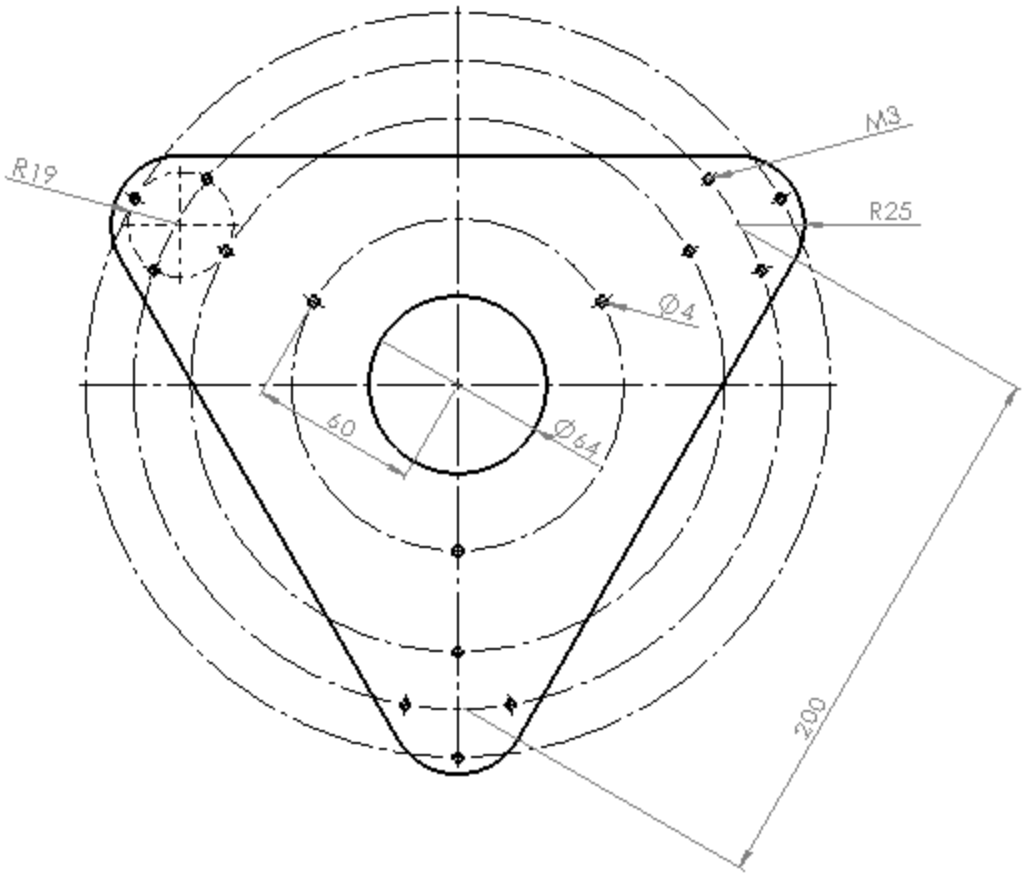

Figure 8.8: Moving platform design

The thickness of the moving platform is 20 mm. Choose this thickness according to the attached parts for further application.

8.1.4 The Moving Platform Revolute Joint Design

On the platform, there are three revolute joints which are fixed by 4 M3 screws respectively. The distance between every two revolute joints is 200 mm long. This comes from the kinematic improvement section of Chapter 4. The assembly drawing of the moving platform revolute joint is shown in Figure 8.9.

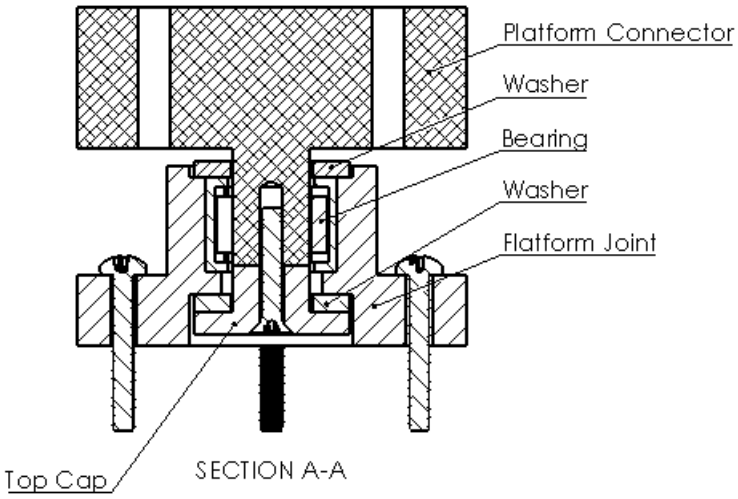

Figure 8.9: The assembly of moving platform revolute joint

In terms of the revolute joint bearings in the assembly, choose three needle bearings, allowing more precision and smaller fit. The diameter of the inner circle is 10 mm. This kind of bearing could tolerate more bending moment compared to a classic ball bearing.

It can be observed that the most dangerous part is the “Platform Connector”, which is fit to the needle bearing. The reason is that the shaft part is used to overcome the bending moment coming from the platform weight. The bending moment is 1.15 Nm. The static analysis result is shown in Figure 8.10. The highest stress, 35 MPa, is smaller than the yield stress.

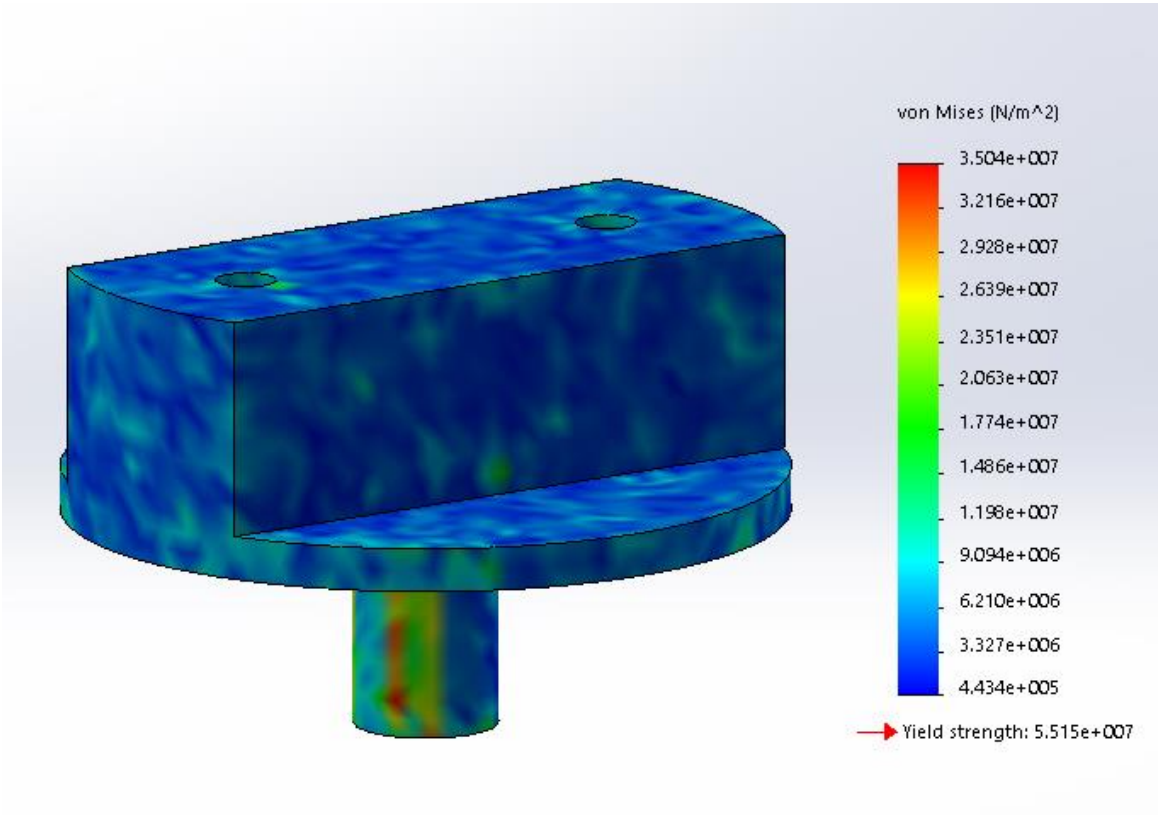

Figure 8.10: Static analysis result of the platform connector

8.1.5 The Clamp Design

There are three sets of two clamps for each linear actuator. The clamps are used to fix the linear actuator and potentiometer to the fixed revolute joints. According to reference [43], the friction coefficient between steel and aluminum is 0.6. In order to obtain a 100 N linear force, the clamp will have to tolerate a 166.67 N compression force.

Furthermore, the linear actuator and potentiometer will have gravity forces applying to the clamp as well, which is equal to 40 N approximately. Choose the thickness of clamp as 2 mm, the material is steel. The drawing of the clamp is shown in the Figure 8.11 below:

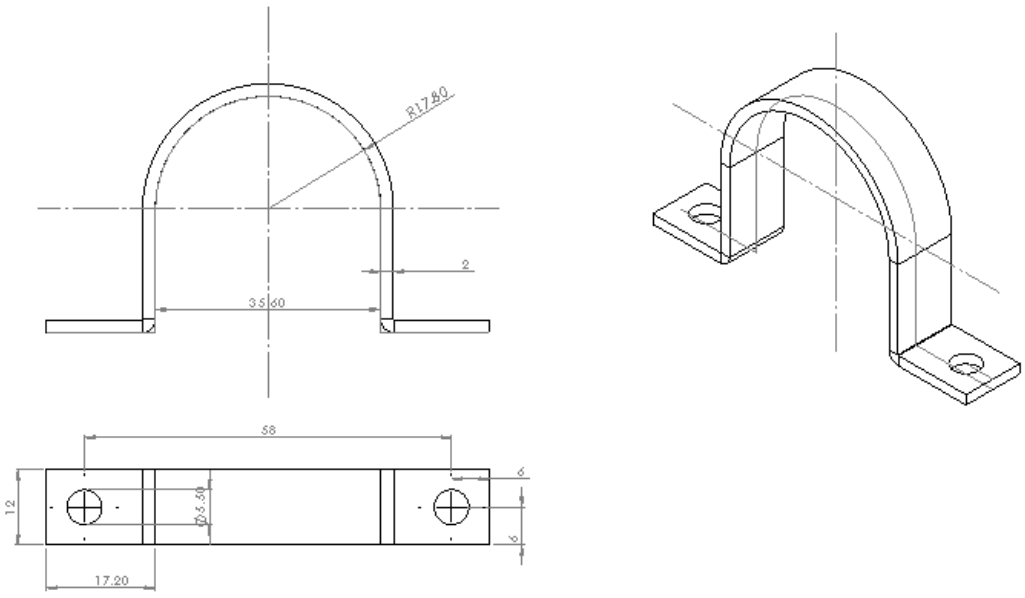

Figure 8.11: Clamp drawing

Apply 17.27 Nm bending moment on the clamps and connecting bracket. The stress analysis result is shown below. From the Figure 8.12, it could be seen that there are some points with stress concentration. The highest stress is 52.11 MPa, which is smaller than the permissible tensile stress: 210 MPa.

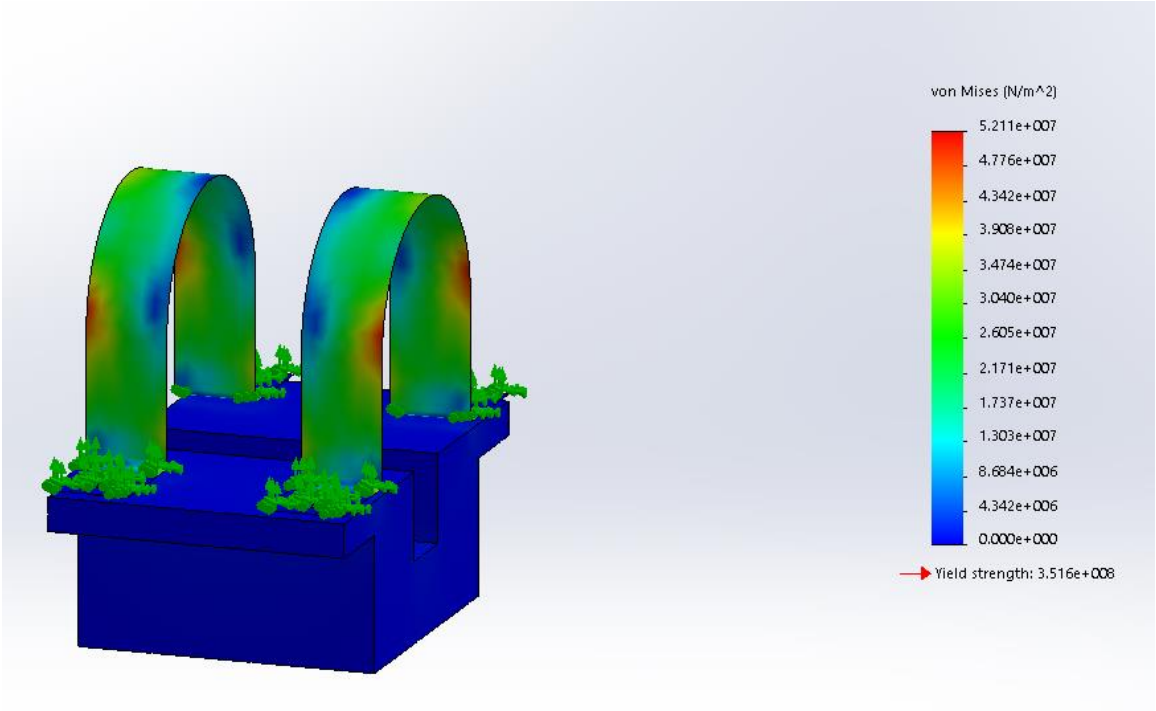

Figure 8.12: Stress Analysis when Closest

Then use Solidworks to generate the deformation result. The highest value is 0.035 mm at the edge of the clamp. From the Figure 8.13 and Figure 8.14, to determine the vertical position change of the joint Bi.

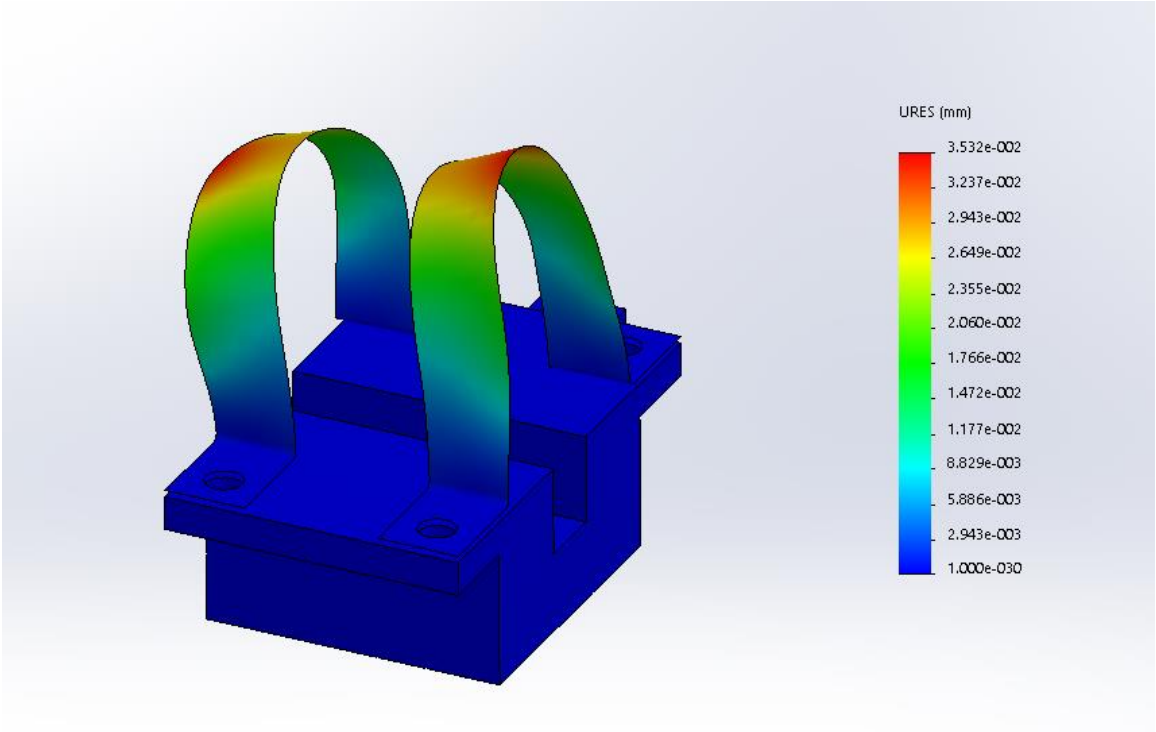

Figure 8.13: Displacement Analysis when Closest

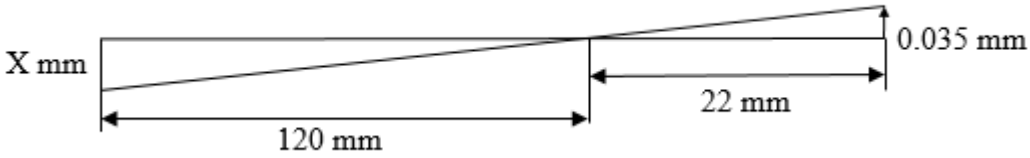

Figure 8.14: Displacement of Bi Assumption when Closest

From the Figure 8.14, it could be seen that the vertical displacement is 0.035*120/22 = 0.19 mm, when the moving platform is in the closest position to the fixed joint.

Secondly, apply 5.25 Nm bending moment (when the platform is in the furthest position to the fixed joint) on the clamps and connecting bracket. The stress analysis result is shown

in Figure 8.15. From the image, it could be seen that there are some stress concentration points. The highest stress is 15.84 MPa, which is smaller than the yield strength: 210 MPa.

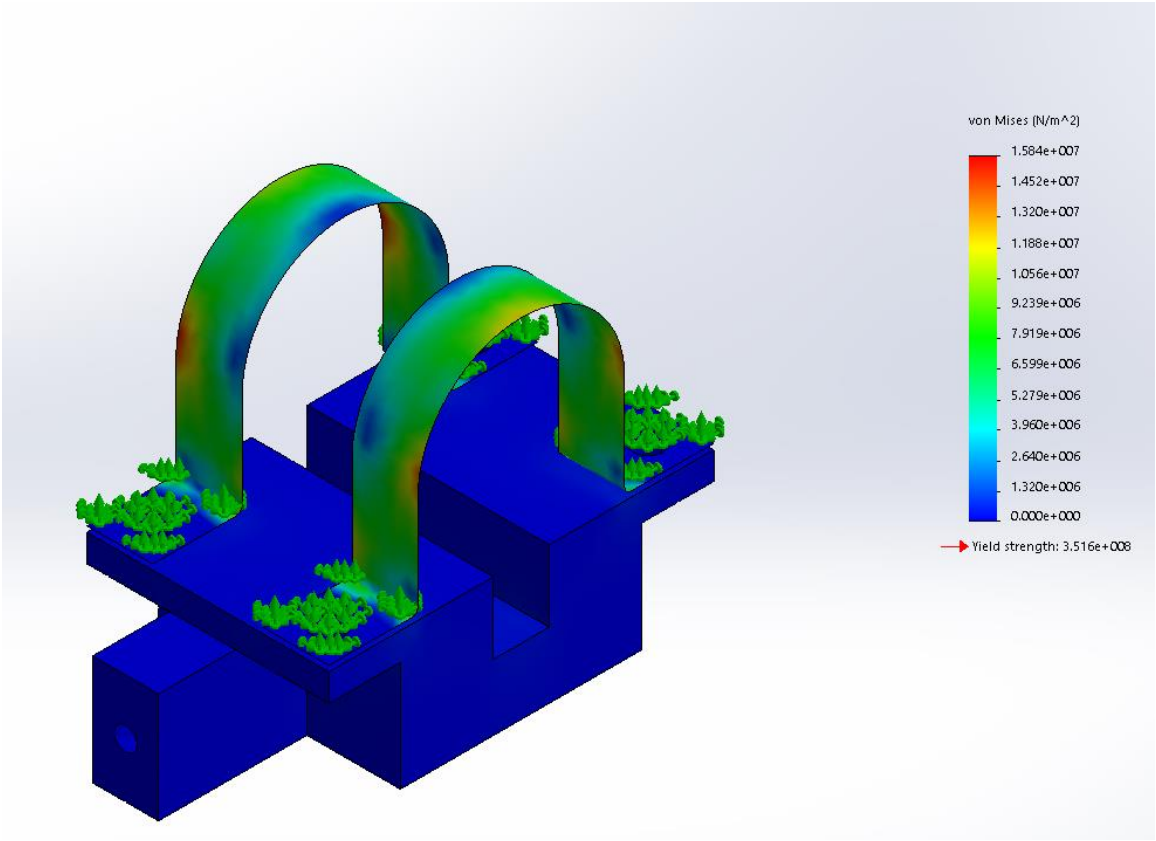

Figure 8.15: Stress Analysis when Furthest

Then use Solidworks to generate the deformation result. The highest value is 0.011 mm at the edge of the clamp. From the Figure 8.16 and 8.17, determine the position change of joint Bi.

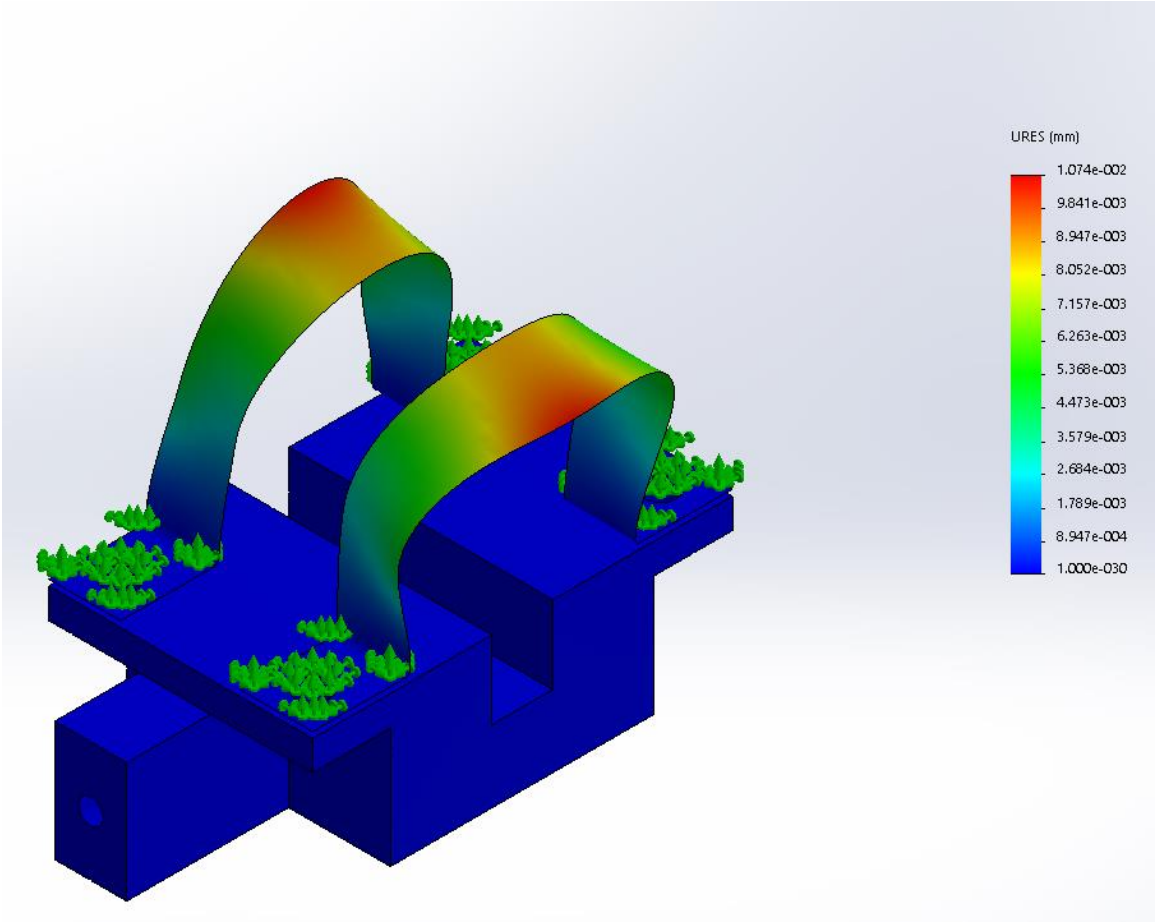

Figure 8.16: Displacement Analysis when Furthest

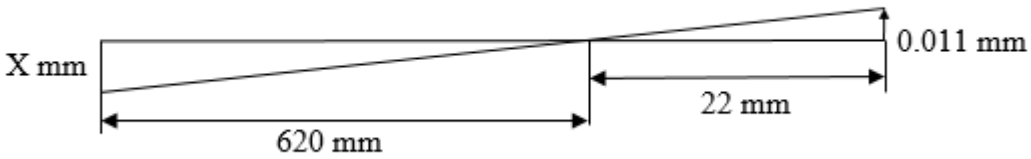

Figure 8.17: Displacement of Bi Assumption when Furthest

From Figure 8.17, it can be observed that the displacement is 0.011*620/22 = 0.31 mm, when the moving platform is the most close to fixed joints.

From the Figure 8.14 and 8.17, it could be seen that the difference between the highest displacement and lowest displacement is 0.12 mm, which is a relevant small value for the platform vertical deflection, as this manipulator will be used for pick and place applications.

According to the platform size, it could be seen that the difference between B1 and B2 would cause an angle displacement of platform. Assume that the B1 has the highest displacement; B2 and B3 have the lowest displacement. As a result, the angle error is equal to $6.928*10^{-4}$ rads when looking from the view in Figure 8.20, which is equal to 0.03969 degrees.

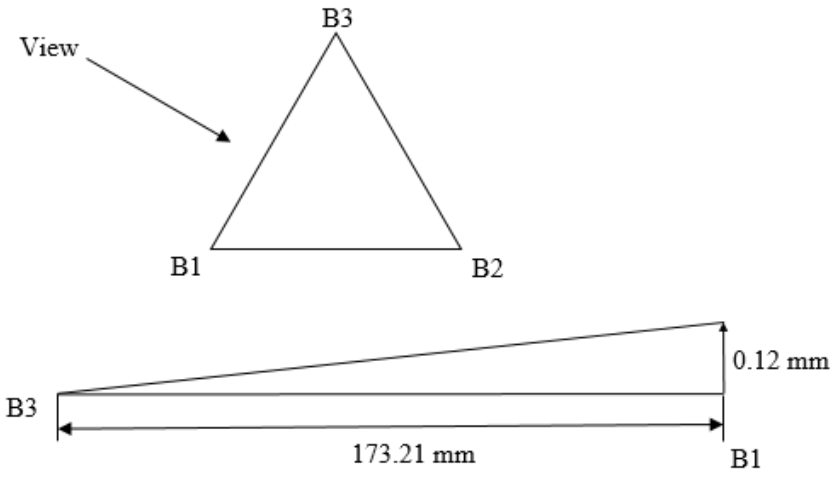

Figure 8.18: Angle error analysis

8.1.6 The Linear Actuator Attachment Design

According to our budget and the project requirements, the "FA-200-L-12-XX" Firgelli linear actuator is chosen. Its top speed is as slow as 0.8''/s (20.32 mm/s). The dynamic force limit is 200 lbs (890 N). Because it is not supplied with encoder or sensors, it is necessary to attach a linear potentiometer to obtain the stroke length signals. Firgelli 25 inches linear potentiometer is chosen as the stroke length sensor. The technical drawings of the linear actuator and potentiometer are shown in Figure 8.19 and 8.20. The figures come from the Firgelli official website.

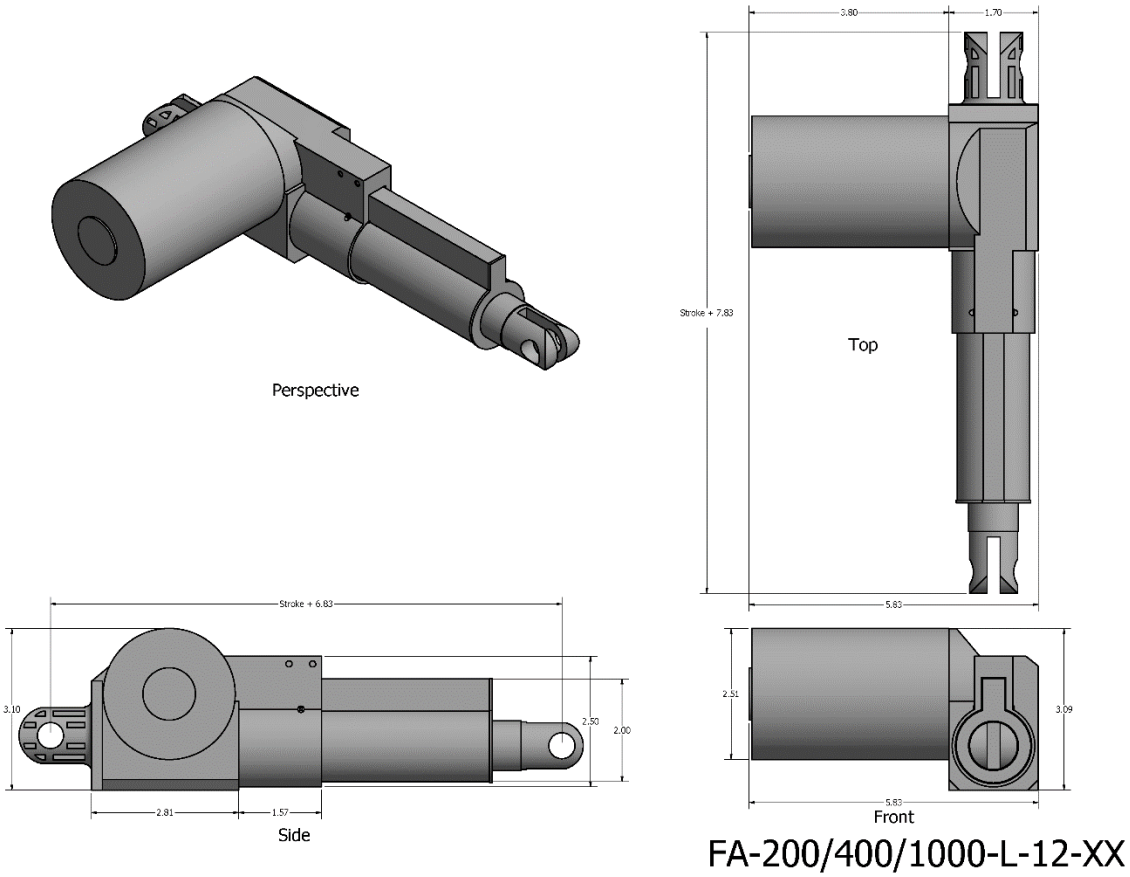

Figure 8.19: Linear actuator drawing (from Firgelli official website)

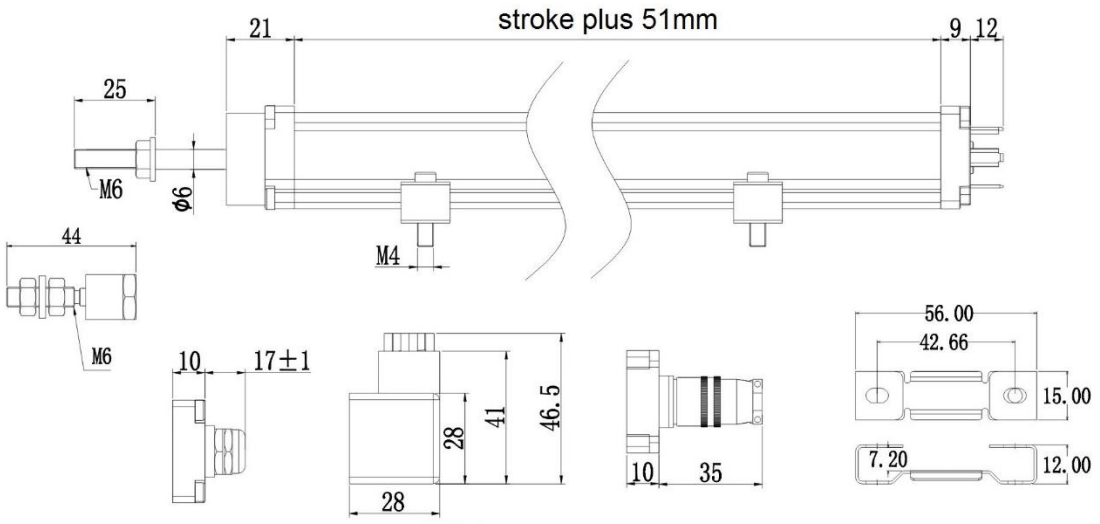

Figure 8.20: Linear potentiometer drawing (from Firgelli official website)

In order to make a connection of the classic prismatic linear actuator, the fixed joints have been designed in the section 8.1.2. The linear actuators will be attached to a bracket which has four M5 holes to fit the fixed joints. For the potentiometer, it is attached to the bracket and the end of linear actuator. There are four M5 flat head screws at the end of the potentiometer. As a result, the potentiometer could stay parallel with linear actuator after assembly.

The overall assembly of the linear actuator with potentiometer is shown below in Figure 8.21. The linear actuator is fixed to the bracket through two clamps from front. There are two reasons why apply this construction. One reason is related to the kinematic performance in Chapter 4: The manipulator would have better performance if the moving

platform were closer to the fixed joints Bi. With this assembly, the platform will counter the weight of the back motor (Table 8.1), which is the second reason.

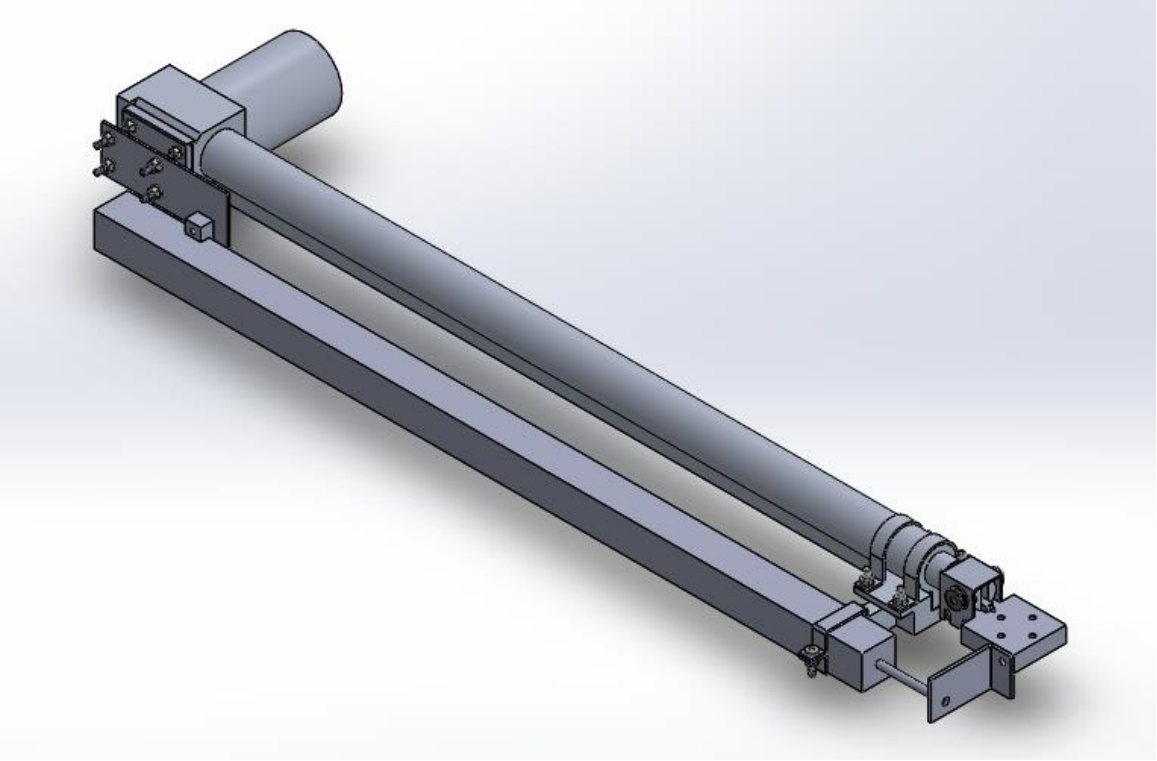

Figure 8.21: Overall assembly of linear actuator and potentiometer

8.1.7 Introduction to High Performance Linear Actuator

Another master student in our lab, Md Toufiqul Islam, has conducted a great work design a high performance linear actuator. It is called "X" actuator in this thesis. This actuator can reach an acceleration as high as 15 g (147.15 m/s^2).

One of our mechanical design goals is to assemble it to the same fixed revolute joint in Section 8.1.4. The actuator is shown in Figure 8.22 below.

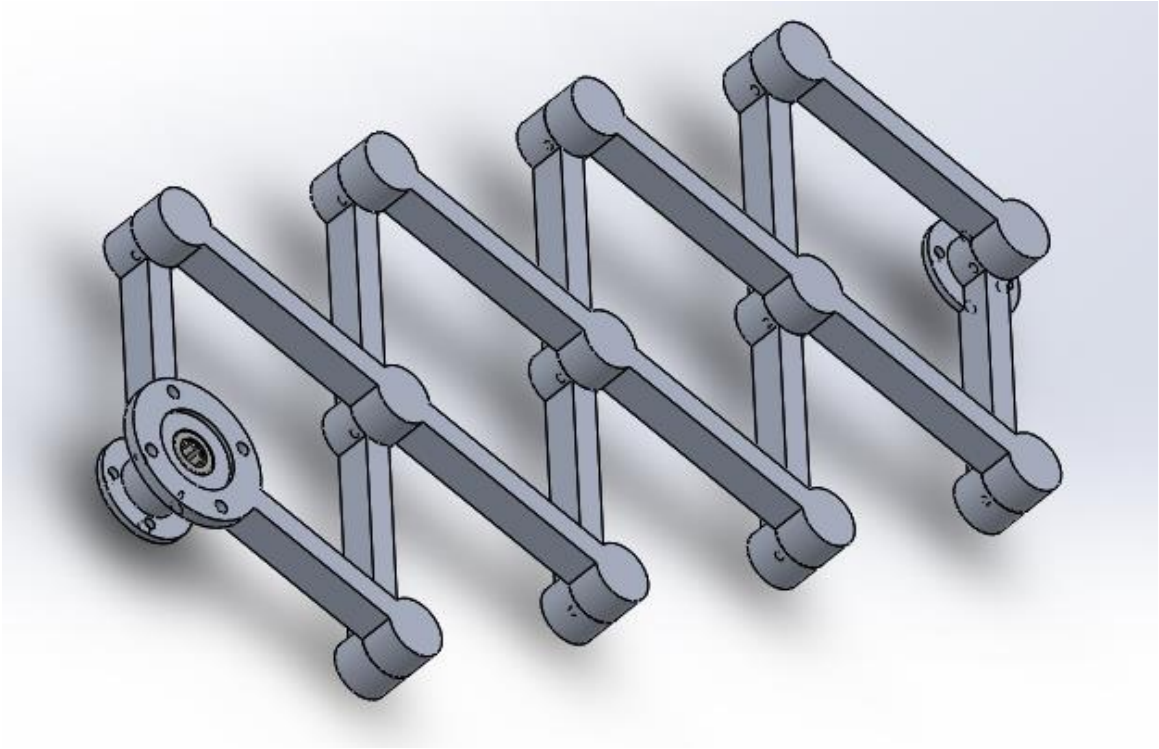

Figure 8.22: High performance linear actuator

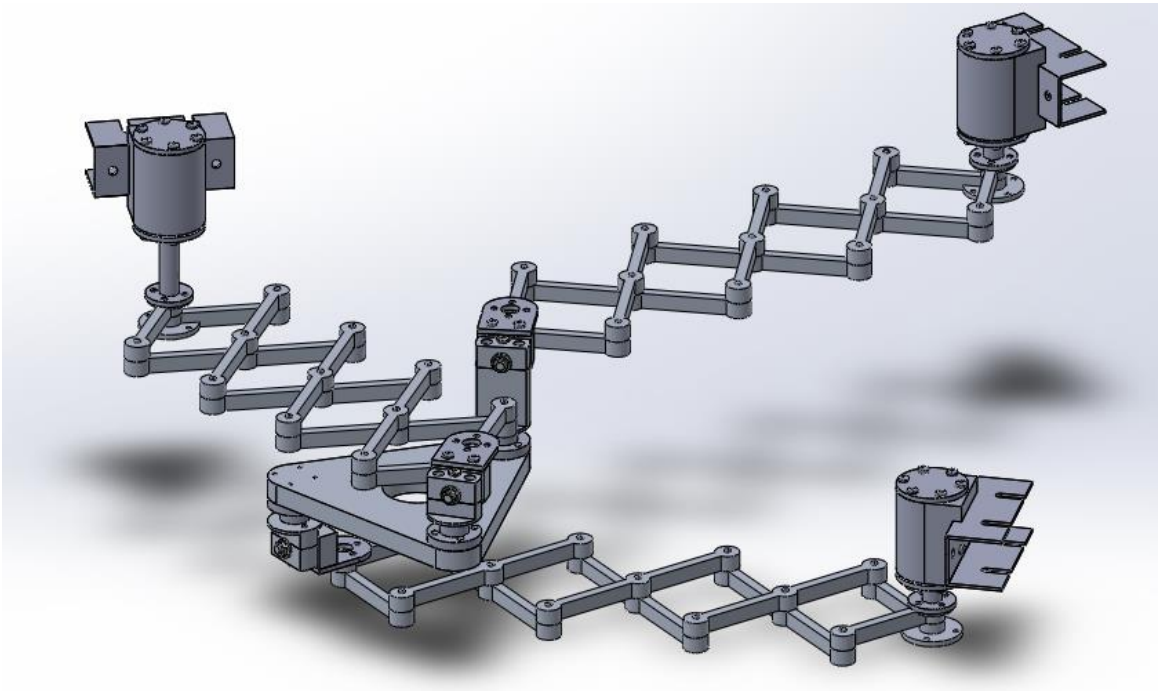

Figure 8.23: Overall assembly of the 3-RPR PPM with "X" actuator

The assembly drawing is shown in Figure 8.23. From the drawing, it can be observed that the “X” actuator can be fixed to the fixed revolute joint, as well as the moving platform. In Figure 8.24, the actuator is fixed to the joint through four M5 screws.

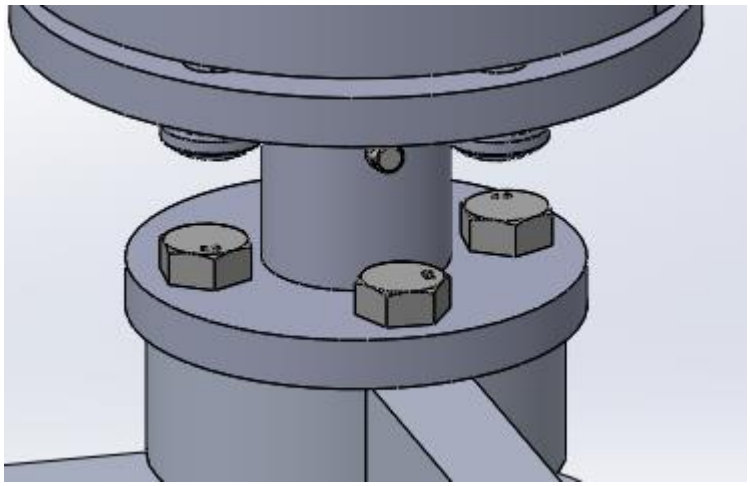

Figure 8.24: Connection between fixed revolute joint and “X” actuator

8.2 Mechanical Assembly

8.2.1 The Moving Platform Assembly

On the platform, there are three revolute joints which are fixed by 4 M3 screws respectively. One of them is located on the bottom side. The other 2 joints are fixed on the top of moving platform. The distance between every two revolute joints is 200 mm long. This comes from the kinematic improvement section of Chapter 4

With the joints distribution in Figure 8.25, the “cross-leg” configuration could be applied to the moving platform without collision between two linear actuators. The assembly drawing of the moving platform with three revolute joint is shown in Figure 8.25.

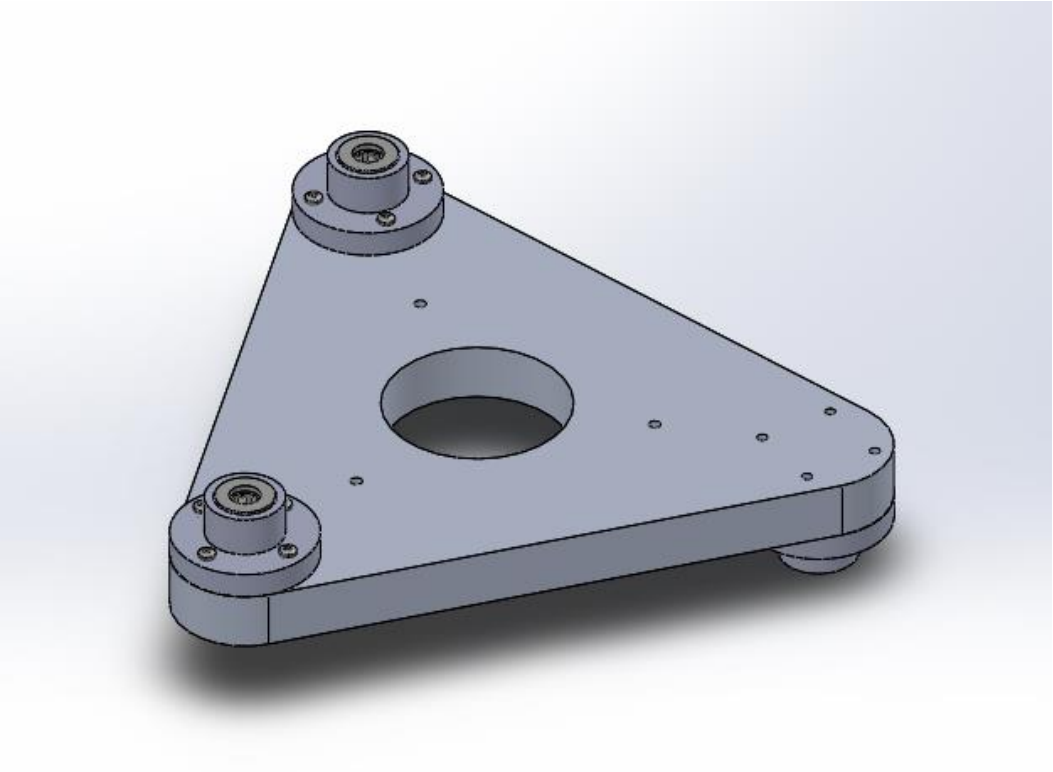

Figure 8.25: Moving platform assembly with joints

8.2.2 The Fixed Revolute Joints and Frame Assembly

The overall assembly of the fixed base joint is shown in Figure 8.26.

Use a plate to connect fixed joints to the frame. And the connection between the frame and the plate is shown in Figure 8.26. From the image, it can be observed that the fixed joints could be placed at different levels to meet different requirements. With these screws, the positions of three fixed joints can be modified on the frame as they can be slid around the frame.

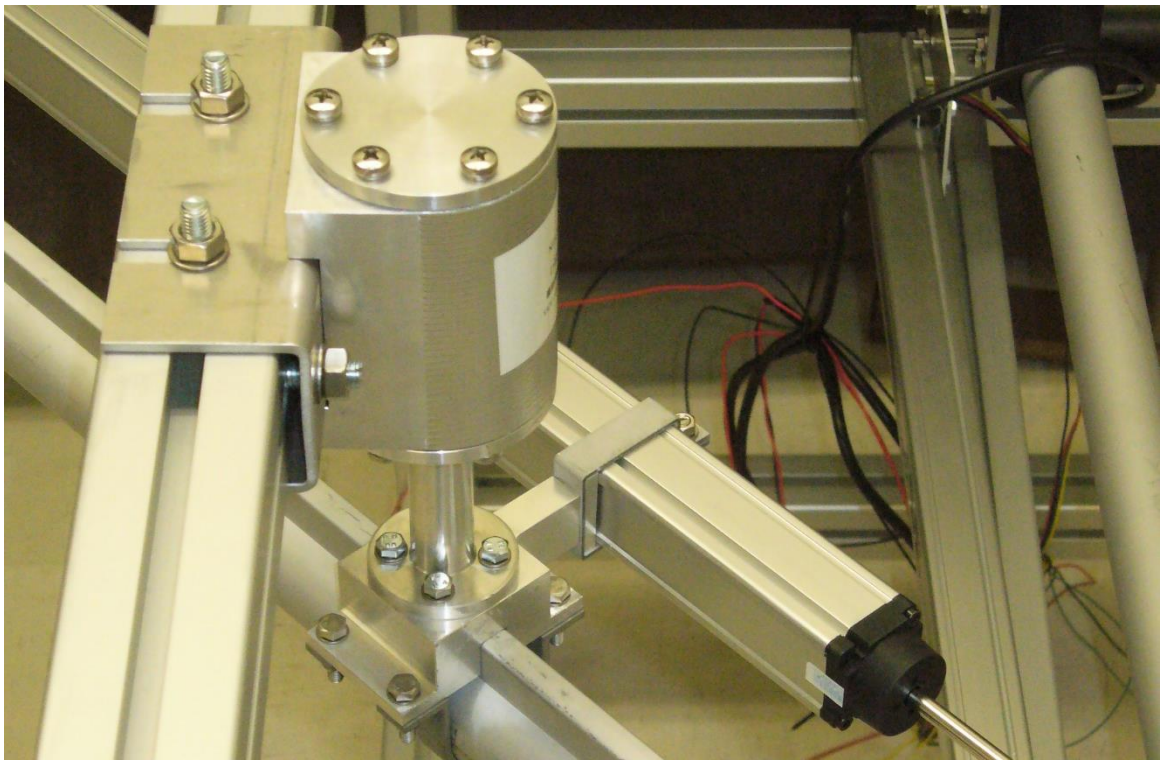

Figure 8.26: Plate and frame connection

8.2.3 The Linear Actuator and Potentiometer Assembly

Figure 8.27 shows the front connection between linear actuator and potentiometer.

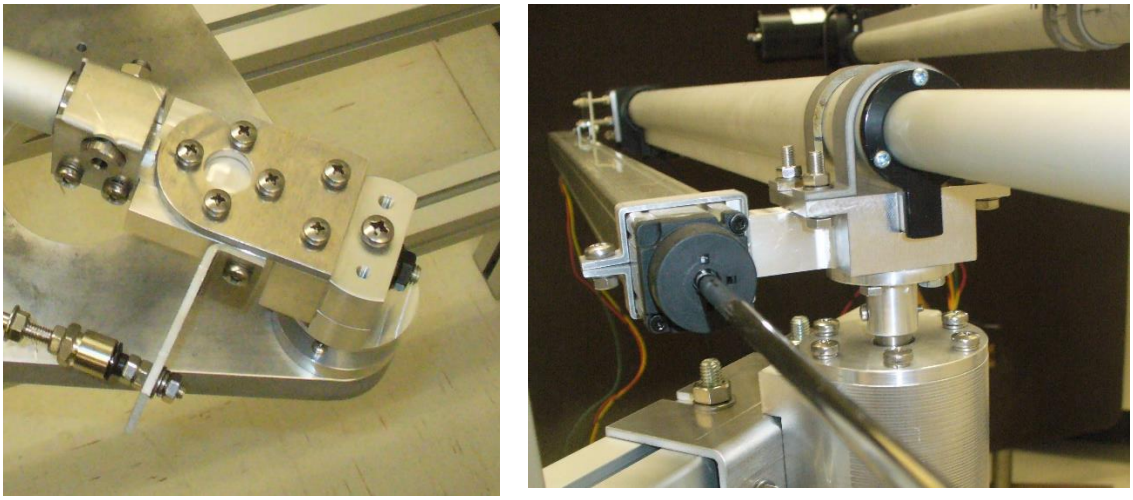

Figure 8.27: Front connection between linear actuator and potentiometer

The left image in Figure 8.27 is the connection among the linear actuator, the potentiometer and the revolute joint on the moving platform. In the right image, the linear actuator and the potentiometers are connected together by the bracket and the clamp.

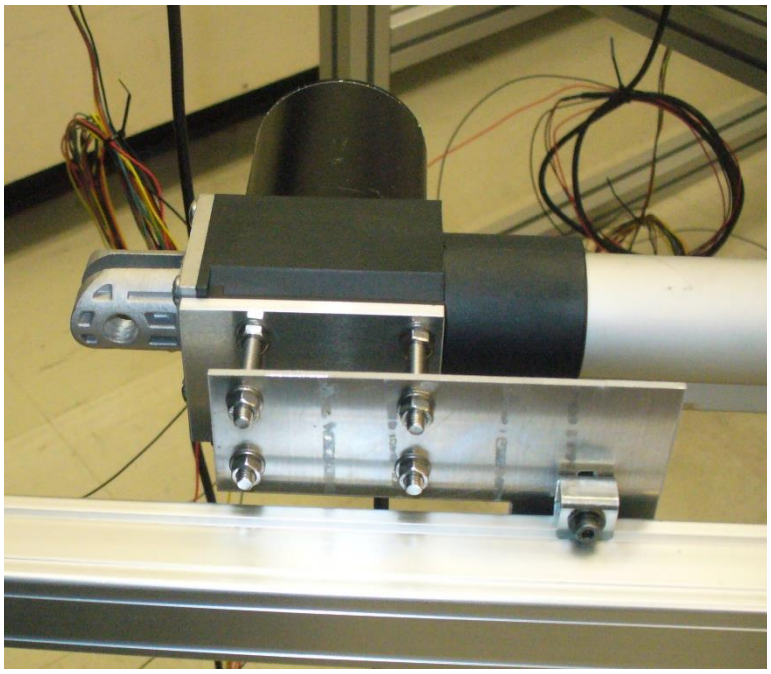

Figure 8.28: Back connection between linear actuator and potentiometer

Figure 8.28 shows the detailed assembly image of the back connection between the linear potentiometer and actuator. There are four M5 screws to adjust two parts in parallel. The clamp on the potentiometer could also adjust its position by moving it upwards or downwards. As a result, the potentiometer output voltage signal shows the actual extended actuator stroke length.

8.2.4 Overall Mechanical System Assembly

Figure 8.29: Overall Mechanical System

The overall robot assembly is shown in Figure 8.29, the three linear actuators distributed at three different levels, the links then can cross each other without collision. This corresponds to the “cross-leg” configuration in Chapter 4. With this layout, the manipulator can be made to be reconfigured more easily.

8.3 Electric Hardware Connection

In order to control the 3 RPR robot, it is important to select the controller and motor drivers. The electrical DC motors, need one 12 V power supply. The potentiometer signal voltage ranges from 0 to 1.8 V.

8.3.1 Beaglebone Single-board Computer

The Beaglebone Board is a low-power single-board computer produced by Texas Instruments in association with Digi-Key and Newark element14 which is also designed to run with open source software. In 2014, the Beaglebone Black Rev C was released, which the most advanced one is so far. It has one single 1 GHz processor and 4 G bytes of flash memory.

Figure 8.30 shows the diagram of the Beaglebone Black Cape Expansion Headers for one LCD touchable screen. The microprocessor board comprise two connector plates, named P8 and P9. For instance, “P8-32” is the NO. 32 port on the plate 8. It is a 1.8 voltage port for analog signal power supply. “P8-34” is the ground port corresponding to the “P8-32”.

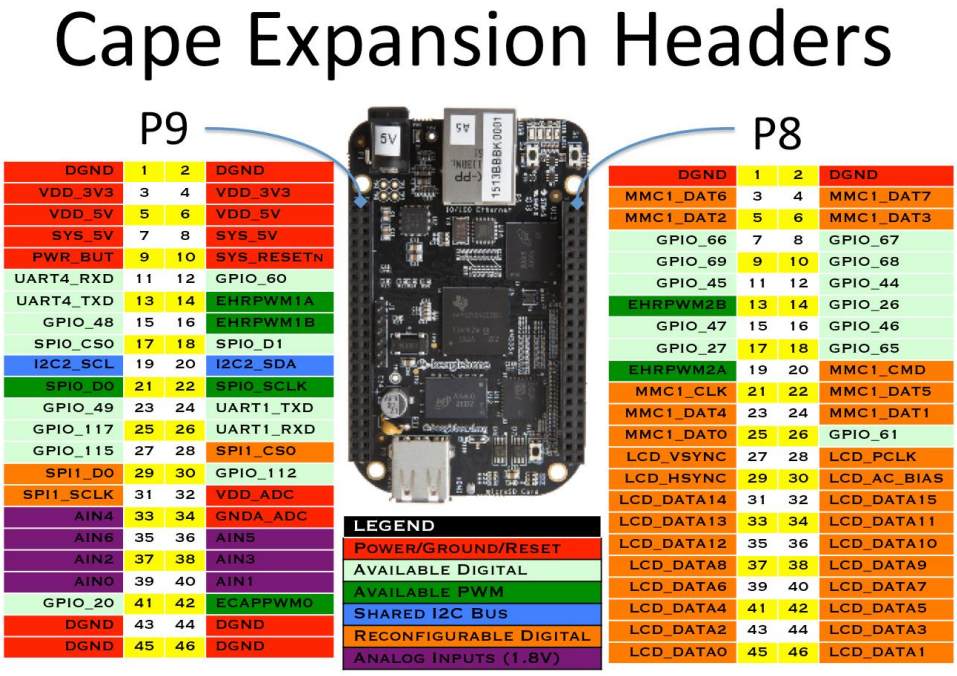

Figure 8.30: Beaglebone Black Cape Expansion Headers (from Beaglebone official website)

Figure 8.31 represents the connection for pulse-width modulators (PWM) amplifiers.

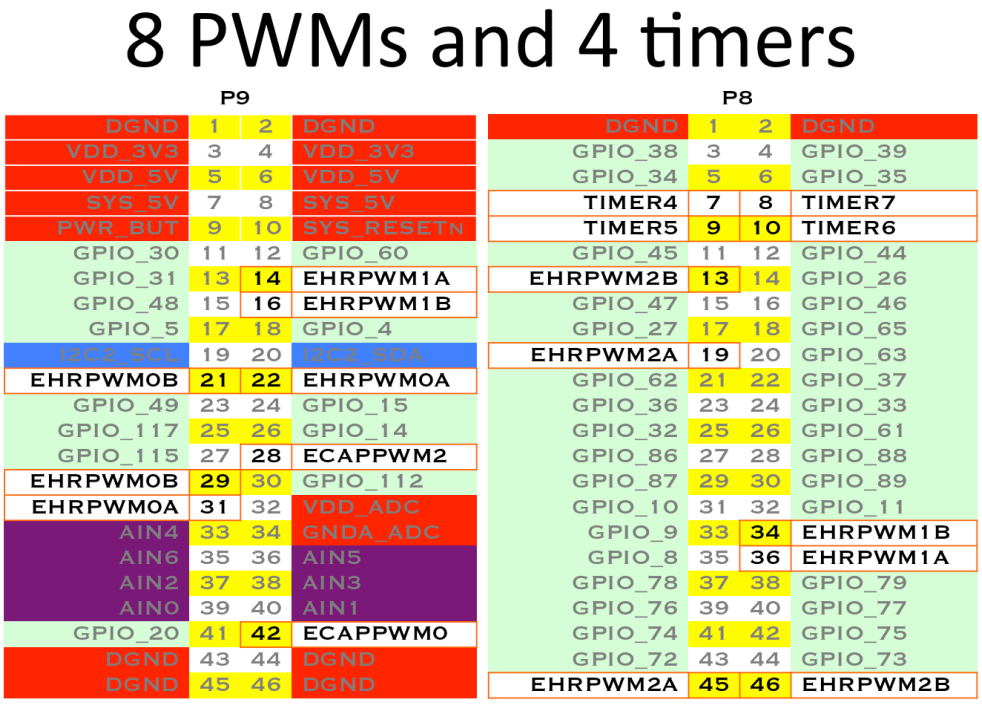

Figure 8.31: PWM control with 4 timers headers (from Beaglebone official website)

In Figure 8.31, there are up to 8 PWM outputs available on the board. In addition, seven analog inputs were used to connect the joint position sensors. The general purpose input and output (GPIO) headers could be used to obtain encoder signals as well when the "X" actuators are in use. The ports used to control the 3-RPR robot are illustrated in Table 8.2.

Table 8.2: Description of the headers to use

Header Name	Description	Voltage
P9-02	Digital Signal Ground	Ground
P9-11	Digital Signal from GPIO, controls the direction to extend	3.3 V
P9-12	Digital Signal from GPIO, controls the direction to extend	3.3 V
P9-13	Digital Signal from GPIO, controls the direction to extend	3.3 V
P9-14	PWM Control Signal	3.3 V
P9-16	PWM Control Signal	3.3 V
P9-21	PWM Control Signal	3.3 V
P9-32	Analog Signal Voltage Supply	1.8 V
P9-34	Analog Signal Ground	Ground
P9-33	Analog Input Signal, shows the actuator extended length	0~1.8 V
P9-35	Analog Input Signal, shows the actuator extended length	0~1.8 V
P9-36	Analog Input Signal, shows the actuator extended length	0~1.8 V

8.3.2 Potentiometer Connection

Use three Firgelli linear potentiometers to obtain the extended stroke lengths of the three linear actuators. After the two parts are assembled together, as shown in section 8.2.3, connect four headers of each potentiometer are connected to the Beaglebone board.

As shown in Figure 8.32, there is one 1 K resistor connected in series with one potentiometer. There are four wires coming from potentiometer which are in four different colors: red, blue, yellow and black.

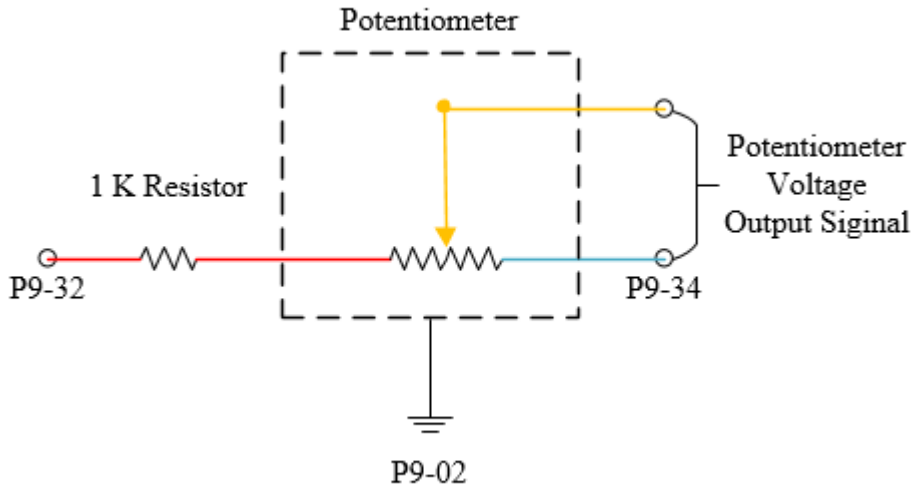

Figure 8.32: Potentiometer connection

The P9-32 header on the Beaglebone board gives 1.8 V power supply to the potentiometer. After one 1 K resistor, the connect goes into the potentiometer through the red wire. The output voltage signal is the voltage between the yellow wire and the blue wire. The black wire of the potentiometer is connected to the common ground port of the whole system, which is the header P9-02.

8.3.3 Motor Driver Board Connection

In order to drive an electrical motor with the 12 V DC power supply, it is needed to use a motor driver board to amplify control board digital signal output. In this case, use “Cytron

13A, 5-25V Single DC Motor Controller" to complete the PWM motor driver. The connection of the driver board is illustrated in Figure 8.33 below.

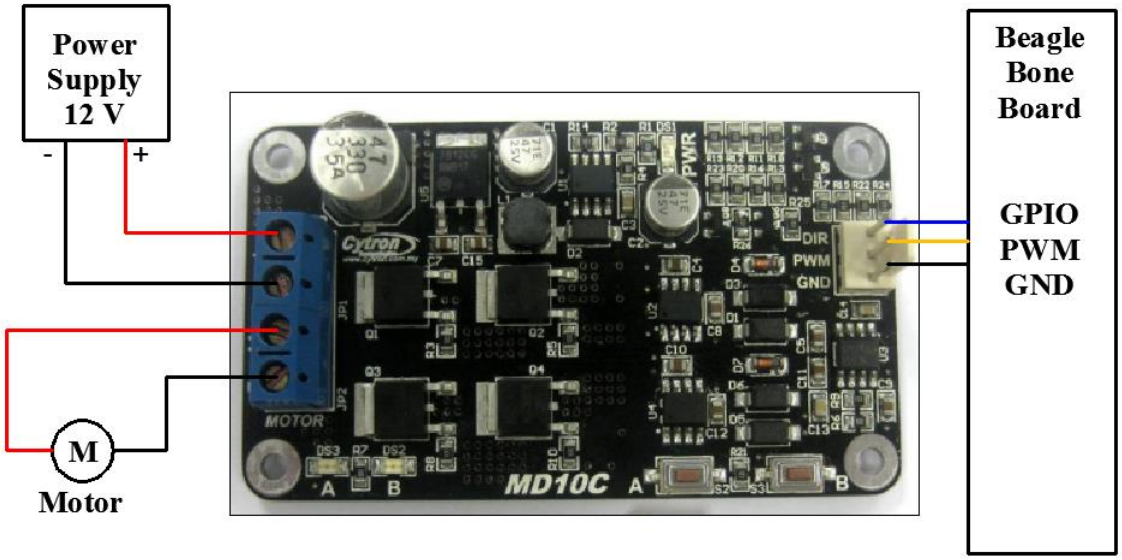

Figure 8.33: Motor driver board connection

There are two wires coming out from one linear actuator, which is the motor in Figure 8.33. When the red wire is connected to the positive signal of power supply and the black one connected to the ground, the linear actuator will extend. On the right hand side of graph, the GPIO generates a digital extension signal to conduct a direction change when it is needed. Furthermore, the "PWM" represents "EHRPWM" ports within Plate 9 in Figure 8.31.

8.3.4 Overall Electrical Hardware Connection

The overall electrical hardware connection graph is shown in Figure 8.34. According to section 8.2.1 to 8.2.3, connect three sets of potentiometer and linear actuator together.

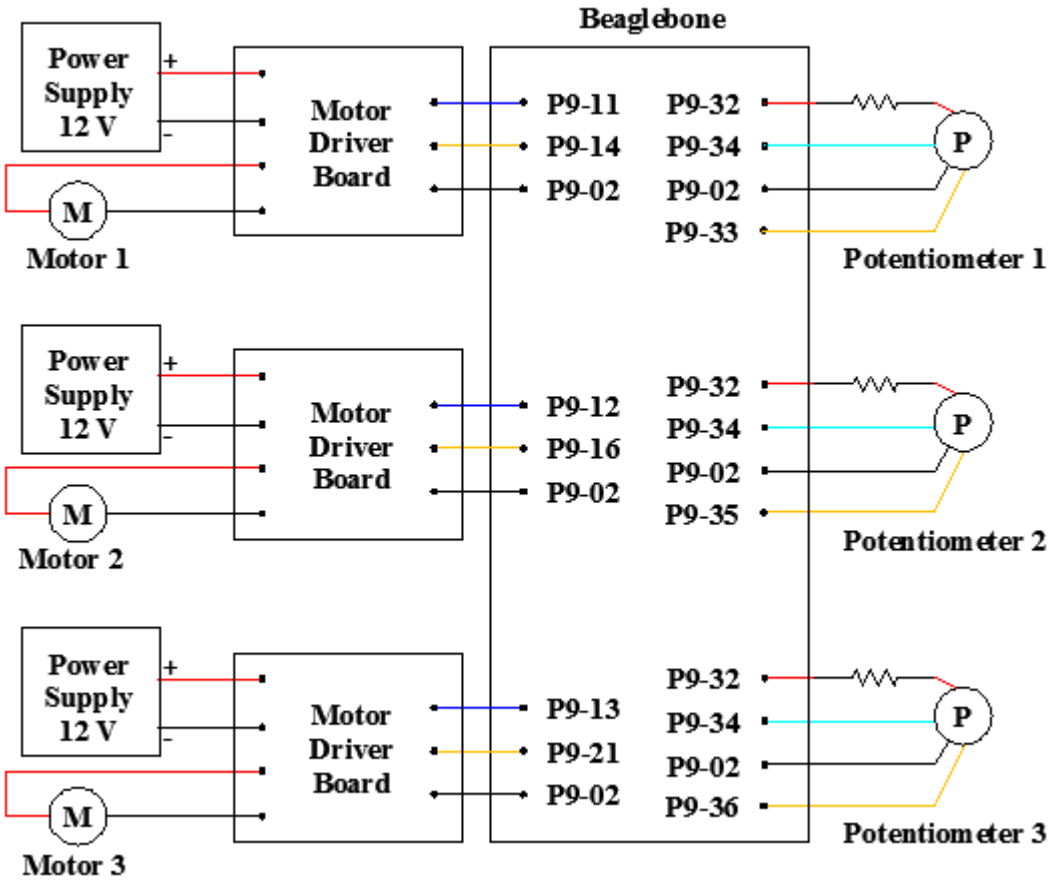

Figure 8.34: Overall electrical hardware connection

8.4 Summary

In this chapter, the mechanical component design, the robot assembly and electronic hardware connection of 3-RPR robot have been introduced. After static analysis, choose the diameter size of the shaft and the thickness of the clamp. As the whole mechanical system has been built, it can be seen that the revolute joint shaft is strong enough to overcome the stress applied on it from bending moment. The built robot is different from the previous design of other scientists. This is the first 3-RPR model in the world that can be made to be reconfigurable. The positions of three fixed joints can be adjusted and relocated on the frame. Three sets of linear actuators are distributed at three different levels.

Chapter 9

Conclusion

9.1 Conclusion

In this Master thesis, the complete design and construction of the 3-RPR PPM was accomplished. As it was requested in the specifications, I have provided a design which allows some level of reconfiguration which is listed as follows:

(a) The manual repositioning of joints connected to fixed base.

(b) The possibility to replace the standard linear actuators by the novel X actuators.

The most important contributions of the thesis are:

(a) I examined manipulator performance by positioning the mobile platform in the entire workspace

(b) I introduced bond graph modeling for the dynamic analysis of the 3-RPR PPM. And it was validated by the results of the application of the virtual work principle.

(c) According to the average DSI values within the workspace, we provide an approach to choose the proper moving platform sizes aiming at balancing manipulator performance in the X and Y directions.

In order to improve the manipulator performance, I have conducted kinematic analysis in Chapter 4 and 5 based on the Jacobian formulation leading to performance indices. The performance improvement is one of the important contributions in this thesis. It is shown

that to put the platform outside the three fixed joints can improve manipulator performance. The kinematic analysis also allowed us to determine the ratio between the platform dimension and the fixed joints distance for improved performance. Three kinematic chains in three different planes make it possible to apply the "cross-leg" configuration to the assembly, which provides improved performance.

Without doubt, virtual work has played a significant role in the field of robot dynamic analysis, the advantages of which have been described in Chapter 6 and 7 and in this thesis; we introduced it to dynamics modeling of the 3-RPR PPM.

However, bond graph is an efficient methodology for dynamic analysis since both bond graph and virtual work produced the same results on open loop control in Chapter 7. The most important merits of bond graph are:

(a) It could integrate different dynamic systems within one method.

(b) It could solve dynamic problems without detailed dynamic equations set up.

(c) It integrates kinematics easily.

(d) It includes any control algorithm.

In Chapter 7, the modeling and simulation procedures were introduced for 3-RPR PPM in 20-sim. As there are numerous elements in the mechanism, it is necessary to automatically calculate initial values for different segments and values for passive parts, rather than inputting each one manually. This thesis introduces a way to generate initial variables of

each elements in bond graph, which shows that bond graph has a great potential for simulation to help the design process.

Furthermore, according to the result, it can be noticed that bond graph can simulate the movement of the PPM properly. Not only the kinematic performance, but also the dynamic plots of each link can be obtained. However, there are some position errors remaining in the end of the simulation of about 1%.

The 20-Sim program produces a very useful manipulator animation, rendering the results in a more intuitive way. Engineers could evaluate numerous points to improve the performance upon.

The construction includes the fixed joints design. The fixed joints were designed to welcome two actuator types, one is the classical linear actuator, and the other one is the X-track actuator, coming from another Master thesis topic in the High Performance Robotics Laboratory, [51]. The frame design is allowing for fixed base reconfiguration, meaning the fixed joints could be placed anywhere on the frame.

It is difficult to find a proper linear actuator for long stroke including a position sensor and allowing for high accelerations (over 5 g). The thesis project was limited to the typical low speed and high force linear actuators. Variable resistors are known for their limited accuracies and noisy signals. The installation of the whole PPM is also very challenging, as it is difficult to adjust three linear actuators to be moving on parallel planes. To obtain

absolute parallelism between one linear actuator and its linear potentiometer is impossible in practice. These limits are non-existent with the X-track actuators.

9.2 Future Work

The author recommends the individuals in the future to:

1. Integrate the high performance linear actuator and manipulator to conduct kinematic and dynamic analysis. Generally, this thesis mainly concentrates upon the manipulator with the classical linear actuator, rather than the high performance one. The research of the high performance actuator and this thesis were processed in parallel in our lab.

2. Develop a more advanced motion control strategy rather than a simple PID loop. The controller in Chapter 6 is just used as a validation test of the control integration in the bond graph. In the future, an appropriate control method will be needed to simulate the robot with the bond graph model, including the path control.

3. There is a difference between the target and actual positions during the simulation. The reason of it might be the parasitic element, involving a slight translation between different joints. It needs further study for better control result.

4. Add additional linear actuators to move the three fixed joints, rather than changing the position manually. The manipulator would comprise a redundant kinematic configuration such as in reference [31].

5. Use high performance “X” linear actuators instead of the classical ones. Control the “X” high performance linear actuator in the laboratory.

Bibliography

[1] Angeles, J. (2007). Fundamentals of robotic mechanical systems.

[2] Arsenault, M., & Boudreau, R. (2006). Synthesis of planar parallel mechanisms while considering workspace, dexterity, stiffness and singularity avoidance. *Journal of Mechanical Design, 128*(1), 69-78.

[3] Au, W., Chung, H., & Chen, C. (2014). Generation of the global workspace roadmap of the 3-RPR using rotary disk search. *Mechanism and Machine Theory, 78*, 248-262.

[4] Bonev, I. A., Zlatanov, D., & Gosselin, C. M. (2003). Singularity analysis of 3-DOF planar parallel mechanisms via screw theory. *Journal of Mechanical Design, 125*(3), 573-581.

[5] Briot, S., Arakelian, V., Bonev, I. A., Chablat, D., & Wenger, P. (2008). Self-motions of general 3-RPR planar parallel robots. *The International Journal of Robotics Research, 27*(7), 855-866.

[6] Coste, M., Chablat, D., & Wenger, P. (2014). Nonsingular change of assembly mode without any cusp. *Advances in robot kinematics* (pp. 105-112) Springer.

[7] Das, S. (2009). Mechatronic modeling and simulation using bond graphs CRC Press.

[8] Firoozabadi, A. E., Ebrahimi, S., & Amirian, G. (2014). Dynamic characteristics of a 3-RPR planar parallel manipulator with flexible intermediate links. *Robotica,* 1-17.

[9] Gosselin, C., & Angeles, J. (1990). Singularity analysis of closed-loop kinematic chains. *Robotics and Automation, IEEE Transactions on, 6*(3), 281-290.

[10] Hossain, M. R., Rideout, D. G., & Krouglicof, D. N. (2010). Bond graph dynamic modeling and stabilization of a quad-rotor helicopter. Dissertation presented at the *Proceedings of the 2010 Spring Simulation Multiconference*, 215.

[11] Kaloorazi, M. H. F., Masouleh, M. T., & Caro, S. (2014). Determining the maximal singularity-free circle or sphere of parallel mechanisms using interval analysis. *Robotica,* 1-15.

[12] Karnopp, D. C., Margolis, D. L., & Rosenberg, R. C. (2012). System dynamics: Modeling, simulation, and control of mechatronic systems. *Modeling, simulation, and control of mechatronic systems* John Wiley & Sons.

[13] Khalil, W., & Dombre, E. (2004). *Modeling, identification and control of robots* Butterworth-Heinemann.

[14] Khalil, W., & Ibrahim, O. (2007). General solution for the dynamic modeling of parallel robots. *Journal of Intelligent and Robotic Systems, 49*(1), 19-37.

[15] Li, S. J., & Gosselin, C. (2009). Stiffness analysis of 3-RPR planar parallel mechanism to the stiffness control. *Applied Mechanics and Materials, 16*, 786-790.

[16] Merlet, J., Gosselin, C. M., & Mouly, N. (1997). *Workspaces of planar parallel manipulators* Springer.

[17] Periasamy, T., Asokan, T., & Singaperumal, M. (2008). Controller design for manipulator trajectory control of an AUV-manipulator system. Dissertation presented at the *Industrial and Information Systems, 2008. ICIIS 2008. IEEE Region 10 and the Third International Conference on,* 1-6.

[18] Rahman, T., Rideout, G., & Krouglicof, N. (2012). Evaluation of dynamic performance of non-spherical parallel orientation manipulators through bond graph multi-body simulation. *Bond Graph Modeling Genoa, Italy,*

[19] Saadatzi, M. H., Masouleh, M. T., Taghirad, H. D., Gosselin, C., & Cardou, P. (2011). On the optimum design of 3-RPR parallel mechanisms. Dissertation presented at the *Electrical Engineering (ICEE), 2011 19th Iranian Conference on,* 1-6.

[20] Sefrioui, J., & Gosselin, C. M. (1995). On the quadratic nature of the singularity curves of planar three-degree-of-freedom parallel manipulators. *Mechanism and Machine Theory, 30*(4), 533-551.

[21] Staicu, S. (2009). Inverse dynamics of the 3-PRR planar parallel robot. *Robotics and Autonomous Systems, 57*(5), 556-563.

[22] Staicu, S. (2009). Power requirement comparison in the 3-RPR planar parallel robot dynamics. *Mechanism and Machine Theory, 44*(5), 1045-1057.

[23] Tsai, L. (1999). Robot analysis: The mechanics of serial and parallel manipulators John Wiley & Sons.

[24] Zein, M., Wenger, P., & Chablat, D. (2006). Singular curves and cusp points in the joint space of 3-RPR parallel manipulators. Dissertation presented at the *Robotics and Automation, 2006. ICRA 2006. Proceedings 2006 IEEE International Conference on,* 777-782.

[25] Žlajpah, L. (2008). Simulation in robotics. *Mathematics and Computers in Simulation, 79*(4), 879-897.

[26] Boschetti, G., Rosa, R., & Trevisani, A. (2011). Parallel robot translational performance evaluation through direction-selective index (DSI). *Journal of Robotics, 2011*

[27] Ma, O., & Angeles, J. (1991). Optimum architecture design of platform manipulators. Dissertation presented at the *Advanced Robotics, 1991.'Robots in Unstructured Environments', 91 ICAR, Fifth International Conference on,* 1130-1135.

[28] Parasuraman, S., & Liang, P. C. J. (2010). Development of RPS parallel manipulators. Dissertation presented at the *Computer and Network Technology (ICCNT), 2010 Second International Conference on,* 600-605.

[29] Chablat, D., & Wenger, P. (2007). The kinematic analysis of a symmetrical three-degree-of-freedom planar parallel manipulator. *ArXiv Preprint arXiv:0705.0959,*

[30] Joubair, A., Slamani, M., & Bonev, I. A. (2013). Kinematic calibration of a five-bar planar parallel robot using all working modes. *Robotics and Computer-Integrated Manufacturing, 29*(4), 15-25.

[31] Kotlarski, J., Abdellatif, H., Ortmaier, T., & Heimann, B. (2009). Enlarging the useable workspace of planar parallel robots using mechanisms of variable geometry. Dissertation presented at the *Reconfigurable Mechanisms and Robots, 2009. ReMAR 2009. ASME/IFToMM International Conference on,* 63-72.

[32] Rakotomanga, N., Chablat, D., & Caro, S. (2008). Kinetostatic performance of a planar parallel mechanism with variable actuation. *Advances in robot kinematics: Analysis and design* (pp. 311-320) Springer.

[33] Campos, L., Bourbonnais, F., Bonev, I. A., & Bigras, P. (2010). Development of a five-bar parallel robot with large workspace. Dissertation presented at the *ASME 2010*

International Design Engineering Technical Conferences and Computers and Information in Engineering Conference, 917-922.

[34] Sharma C, Purohit K. (2003). Design of machine elements. *Prentice Hall of India*.

[35] Merlet, J. (2006). Parallel robots. Springer Science & Business Media, Vol 128.;

[36] Pollard, WLV. (1942). Position-controlling apparatus. *U.S. Patent 2,286,571[P]*.

[37] Pollard, WLG. (1940). Spray painting machine. *U.S. Patent 2,213,108[P]*. *1940*.

[38] Gwinnett JE. (1931). Amusement device. *U.S. Patent 1,789,680[P]*.

[39] Cappel KL. (1967). Motion simulator. *U.S. Patent: 3,295,224[P]*.

[40] Clavel R. (1990). Device for the movement and positioning of an element in space. *U.S. Patent 4,976,582[P]*.

[41] Stewart D. (1965). A platform with six degrees of freedom. Proceedings of the *institution of mechanical engineers*; 180(1):371-386.

[42] Gough V. (1956). Contribution to discussion of papers on research in automobile stability, control and tyre performance; 171:392-394.

[43] Avallone EA, Baumeister T, Sadegh A. (2006). Marks' standard handbook for mechanical engineers (standard handbook for mechanical engineers). *Mcgraw-Hill Professional*.

[44] L'Ecuyer, P., & Owen, A. B. (Eds.). (2009). Monte Carlo and Quasi-Monte Carlo Methods 2008. *Springer.*

[45] Standard, I. S. O. 8373: 2012. (2012). Robots and robotic devices – *Vocabulary*.

[46] ROSELUND, H. A. (1944). Means for moving spray guns or other devices through predetermined paths. *U.S. Patent 2,344,108[P]*.

[47] What is 20-sim? (n.d.). *Retrieved December 20, 2015, from* http://20sim.com/

[48] Chablat, D., Wenger, P., & Bonev, I. A. (2006). Self-motions of special 3-RPR planar parallel robot. *In Advances in robot kinematics (pp. 221-228). Springer Netherlands*.

[49] Chablat, D., & Wenger, P. (2011). Device for the movement and orientation of an object in space and use thereof in rapid machining. *U.S. Patent 7,997,161B2 [P]*.

[50] Williams, R. L., & Joshi, A. R. (1999). Planar parallel 3-RPR manipulator. *In Proceedings of the Sixth Conference on Applied Mechanisms and Robotics (pp. 12-15). Chicago*

[51] Islam, Md Toufiqul (2016). Design Development and Control of a New Generation High Performance Linear Actuator for Parallel Robots and Other Applications (Master dissertation). *St. John's Campus, Memorial University of Newfoundland, St. John's, NL*.

Appendix A

Surface Plot Matlab Code

One highlight of this thesis is the surf plot mapping with Matlab. It is not easy to find a previous sample code to deal with the problem. Many researchers prefer to use Latex to create surf plot when there are several points are void from the result. They obtain the plot from a matrix which comes from the Matlab calculation usually. After checking the code for meshing in Matlab, it was found out that the “meshing” means to divide a certain area into a matrix form. The center of each block represents a certain set of numbers in each loop. The height of surf plot comes from the calculation which based on the position in that area. If there is no value in that block, the small section would become transparent. After a few tests, the method has been mastered to generate a surface plot with some void points in Matlab. In the end of this thesis, the Matlab code for virtual work analysis and surface plots are attached in Appendix A and Appendix B.

```
close all;
clear all;
clc;
set(gcf, 'renderer', 'zbuffer');

N = 800;
xRange = 120;
yRange = 120;
Lmin = 10;
Lmax = 60;
```

```
j = 0;
scount = 0;
jcount = 0;

xs = -60;
ys = -60;
dx = xRange/N;
dy = yRange/N;

th = 0;
Or = 30/(sqrt(3));
O1X = -Or*cos(pi/6);
O1Y = Or*sin(pi/6);
O2X = Or*cos(pi/6);
O2Y = Or*sin(pi/6);
O3X = 0;
O3Y = -Or;
Lmp = 20;

y = ys;
for i = 1:N
   x = xs;
   for k = 1:N
  B1x = x-Lmp*cos(th+pi/6)/sqrt(3);
  B2x = x-Lmp*cos(th+5*pi/6)/sqrt(3);
  B3x = x-Lmp*cos(th+3*pi/2)/sqrt(3);
  B1y = y-Lmp*sin(th+pi/6)/sqrt(3);
  B2y = y-Lmp*sin(th+5*pi/6)/sqrt(3);
  B3y = y-Lmp*sin(th+3*pi/2)/sqrt(3);
  L1 = sqrt((B1x-O1X)*(B1x-O1X)+(B1y-O1Y)*(B1y-O1Y));
  L2 = sqrt((B2x-O2X)*(B2x-O2X)+(B2y-O2Y)*(B2y-O2Y));
```

```
L3 = sqrt((B3x-O3X)*(B3x-O3X)+(B3y-O3Y)*(B3y-O3Y));


IND(i,k) = NaN;
INDx(i,k) = NaN;
INDy(i,k) = NaN;
INDw(i,k) = NaN;
DET(i,k) = NaN;


if all([L1>Lmin, L1<Lmax, L2>Lmin, L2<Lmax, L3>Lmin, L3<Lmax])
  j = j+1;
  if all([x>xs, y>ys])
  WS(j,1) = x;
  WS(j,2) = y;


  a11 = -(2*O1X - 2*WS(j,1) + (2*3^(1/2)*Lmp*cos(pi/6 + th))/3)/(2*((O1X - WS(j,1)
+ (3^(1/2)*Lmp*cos(pi/6 + th))/3)^2 + (O1Y - WS(j,2) + (3^(1/2)*Lmp*sin(pi/6 +
th))/3)^2)^(1/2));
  a12 = -(2*O1Y - 2*WS(j,2) + (2*3^(1/2)*Lmp*sin(pi/6 + th))/3)/(2*((O1X - WS(j,1)
+ (3^(1/2)*Lmp*cos(pi/6 + th))/3)^2 + (O1Y - WS(j,2) + (3^(1/2)*Lmp*sin(pi/6 +
th))/3)^2)^(1/2));
  a13 = -((2*3^(1/2)*Lmp*sin(pi/6 + th)*(O1X - WS(j,1) + (3^(1/2)*Lmp*cos(pi/6 +
th))/3))/3 - (2*3^(1/2)*Lmp*cos(pi/6 + th)*(O1Y - WS(j,2) + (3^(1/2)*Lmp*sin(pi/6 +
th))/3))/3)/(2*((O1X - WS(j,1) + (3^(1/2)*Lmp*cos(pi/6 + th))/3)^2 + (O1Y - WS(j,2) +
(3^(1/2)*Lmp*sin(pi/6 + th))/3)^2)^(1/2));
  a21 = -(2*O2X - 2*WS(j,1) + (2*3^(1/2)*Lmp*cos((5*pi)/6 + th))/3)/(2*((O2X -
WS(j,1) + (3^(1/2)*Lmp*cos((5*pi)/6 + th))/3)^2 + (O2Y - WS(j,2) +
(3^(1/2)*Lmp*sin((5*pi)/6 + th))/3)^2)^(1/2));
  a22 = -(2*O2Y - 2*WS(j,2) + (2*3^(1/2)*Lmp*sin((5*pi)/6 + th))/3)/(2*((O2X -
WS(j,1) + (3^(1/2)*Lmp*cos((5*pi)/6 + th))/3)^2 + (O2Y - WS(j,2) +
(3^(1/2)*Lmp*sin((5*pi)/6 + th))/3)^2)^(1/2));
  a23 = -((2*3^(1/2)*Lmp*sin((5*pi)/6 + th)*(O2X - WS(j,1) +
(3^(1/2)*Lmp*cos((5*pi)/6 + th))/3))/3 - (2*3^(1/2)*Lmp*cos((5*pi)/6 + th)*(O2Y -
WS(j,2) + (3^(1/2)*Lmp*sin((5*pi)/6 + th))/3))/3)/(2*((O2X - WS(j,1) +
(3^(1/2)*Lmp*cos((5*pi)/6 + th))/3)^2 + (O2Y - WS(j,2) + (3^(1/2)*Lmp*sin((5*pi)/6 +
th))/3)^2)^(1/2));
```

```
    a31 = -(2*O3X - 2*WS(j,1) + (2*3^(1/2)*Lmp*cos((3*pi)/2 + th))/3)/(2*((O3X -
WS(j,1) + (3^(1/2)*Lmp*cos((3*pi)/2 + th))/3)^2 + (O3Y - WS(j,2) +
(3^(1/2)*Lmp*sin((3*pi)/2 + th))/3)^2)^(1/2));
    a32 = -(2*O3Y - 2*WS(j,2) + (2*3^(1/2)*Lmp*sin((3*pi)/2 + th))/3)/(2*((O3X -
WS(j,1) + (3^(1/2)*Lmp*cos((3*pi)/2 + th))/3)^2 + (O3Y - WS(j,2) +
(3^(1/2)*Lmp*sin((3*pi)/2 + th))/3)^2)^(1/2));
    a33 = -((2*3^(1/2)*Lmp*sin((3*pi)/2 + th)*(O3X - WS(j,1) +
(3^(1/2)*Lmp*cos((3*pi)/2 + th))/3))/3 - (2*3^(1/2)*Lmp*cos((3*pi)/2 + th)*(O3Y -
WS(j,2) + (3^(1/2)*Lmp*sin((3*pi)/2 + th))/3))/3)/(2*((O3X - WS(j,1) +
(3^(1/2)*Lmp*cos((3*pi)/2 + th))/3)^2 + (O3Y - WS(j,2) + (3^(1/2)*Lmp*sin((3*pi)/2 +
th))/3)^2)^(1/2));

    J = [a11 a12 a13; a21 a22 a23; a31 a32 a33];
    Zd = abs(det(J));
    Zin = sqrt(abs(det(J.'*J)));
    Zinx = sqrt(abs(J(:,1)'*J(:,1)));
    Ziny = sqrt(abs(J(:,2)'*J(:,2)));
    Zinw = sqrt(abs(J(:,3)'*J(:,3)));

    IND(i,k) = Zin;
    INDx(i,k) = Zinx;
    INDy(i,k) = Ziny;
    INDw(i,k) = Zinw;
    DET(i,k) = Zd;

    if Zd==0
      scount = scount+1;
      SI(scount,1) = WS(j,1);
      SI(scount,2) = WS(j,2);
    end
    end
  end

   X(i,k)=x;
```

```
    Y(i,k)=y;
    x = x+dx;
    end
    y = y+dy;
end
```

Appendix B

Virtual Work Analysis Matlab Code

```
clc
close all
clear all

syms X Y phi Vx Vy dotphi Acx Acy Acphi t1 t2 t3

%Variable Inputs

[X, Y, phi, Vx, Vy, dotphi, Acx, Acy, Acphi] = deal(-0.300304002, -0.249949543, -
0.000515925,  0.001257931,  -0.000703925, 0.005192317,  0.049917597,  0.100061697,
        0.000335567);
input = [X,Y,phi,Vx,Vy,dotphi,Acx,Acy,Acphi];

%Kinematic Parameters
e1 = 0.3;
e2 = 0.3;
Lmp = 0.2;
Or = 0.3/(sqrt(3));
A1X = -Or*cos(pi/6);
A1Y = Or*sin(pi/6);
A2X = Or*cos(pi/6);
A2Y = Or*sin(pi/6);
A3X = 0;
A3Y = -Or;

%Moving Platform Position and velocity
p = [X; Y; 0];
wp = [0;0;dotphi];
```

```
xp = [X; Y; 0; 0; 0; phi];
dotxp = [Vx; Vy; 0; 0; 0; dotphi];

%Bi Coordinates
  B1x = X-Lmp*cos(phi+pi/6)/sqrt(3);
  B2x = X-Lmp*cos(phi+5*pi/6)/sqrt(3);
  B3x = X-Lmp*cos(phi+3*pi/2)/sqrt(3);
  B1y = Y-Lmp*sin(phi+pi/6)/sqrt(3);
  B2y = Y-Lmp*sin(phi+5*pi/6)/sqrt(3);
  B3y = Y-Lmp*sin(phi+3*pi/2)/sqrt(3);
  l1 = sqrt((B1x-A1X)*(B1x-A1X)+(B1y-A1Y)*(B1y-A1Y));
  l2 = sqrt((B2x-A2X)*(B2x-A2X)+(B2y-A2Y)*(B2y-A2Y));
  l3 = sqrt((B3x-A3X)*(B3x-A3X)+(B3y-A3Y)*(B3y-A3Y));

% Rotational Matrix from Moving Platform to Global Reference
ORB = [cos(phi) -sin(phi) 0;
   sin(phi) cos(phi) 0;
   0 0 1];
BRO = ORB.';

%The distance between C to Bi
rb = Lmp/(sqrt(3));

% Vector bi in platform reference frame
Bb1 = [-rb*cos(pi/6);-rb*sin(pi/6);0];
Bb2 = [rb*cos(pi/6);-rb*sin(pi/6);0];
Bb3 = [0;rb;0];

% Fixed points position vector
a1 = [A1X; A1Y; 0];
a2 = [A2X; A2Y; 0];
```

```
a3 = [A3X; A3Y; 0];

% Vector bi in global reference frame
b1 = ORB*Bb1;
b2 = ORB*Bb2;
b3 = ORB*Bb3;

% Link Vector
L1 = p+b1-a1;
L2 = p+b2-a2;
L3 = p+b3-a3;

% Link Length
d1 = norm(L1);
d2 = norm(L2);
d3 = norm(L3);

% Unit vector in each link
isi = [0;0;1];
s1 = L1/d1;
s2 = L2/d2;
s3 = L3/d3;

% Link Orientation
th1 = atan2(s1(2),s1(1));
th2 = atan2(s2(2),s2(1));
th3 = atan2(s3(2),s3(1));

% Rotational Matrix from link i to Global Reference
OR1 = [0, -sin(th1), cos(th1);
   0, cos(th1), sin(th1);
```

```
   -1, 0, 0];
OR2 = [0, -sin(th2), cos(th2);
   0, cos(th2), sin(th2);
   -1, 0, 0];
OR3 = [0, -sin(th3), cos(th3);
   0, cos(th3), sin(th3);
   -1, 0, 0];

% Inverse of previous
i1RO = OR1.';
i2RO = OR2.';
i3RO = OR3.';



% Jacobian Matrix for Points Bi
b1x = b1(1); b1y = b1(2); b1z = b1(3);
b2x = b2(1); b2y = b2(2); b2z = b2(3);
b3x = b3(1); b3y = b3(2); b3z = b3(3);

Jb1 = [1, 0, 0, 0, b1z, -b1y;
   0, 1, 0, -b1z, 0, b1x;
   0, 0, 1. b1y, -b1x, 0];
Jb2 = [1, 0, 0, 0, b2z, -b2y;
   0, 1, 0, -b2z, 0, b2x;
   0, 0, 1. b2y, -b2x, 0];
Jb3 = [1, 0, 0, 0, b3z, -b3y;
   0, 1, 0, -b3z, 0, b3x;
   0, 0, 1. b3y, -b3x, 0];

% Calculate Velocity of Bi
```

```
vb1 = Jb1*dotxp;
vb2 = Jb2*dotxp;
vb3 = Jb3*dotxp;

iJb1 = i1RO*Jb1;
iJb2 = i2RO*Jb2;
iJb3 = i3RO*Jb3;

ivb1 = iJb1*dotxp;
ivb2 = iJb2*dotxp;
ivb3 = iJb3*dotxp;

iJb1x = iJb1(1,:);iJb1y = iJb1(2,:);iJb1z = iJb1(3,:);
iJb2x = iJb2(1,:);iJb2y = iJb2(2,:);iJb2z = iJb2(3,:);
iJb3x = iJb3(1,:);iJb3y = iJb3(2,:);iJb3z = iJb3(3,:);

% Velocity and Acceleration Calculation

dotd1 = ivb1(3);
dotd2 = ivb2(3);
dotd3 = ivb3(3);

iw1 = cross(isi,ivb1)/d1;
iw2 = cross(isi,ivb2)/d2;
iw3 = cross(isi,ivb3)/d3;

w1 = OR1*iw1;
w2 = OR2*iw2;
w3 = OR3*iw3;

dotth1 = w1(3);
```

```
dotth2 = w2(3);
dotth3 = w3(3);

dotvp = [Acx; Acy; 0];
dotwp = [0; 0; Acphi];

dotvb1 = dotvp+cross(dotwp,b1)+cross(wp,cross(wp,b1));
dotvb2 = dotvp+cross(dotwp,b2)+cross(wp,cross(wp,b2));
dotvb3 = dotvp+cross(dotwp,b3)+cross(wp,cross(wp,b3));

idotvb1 = i1RO*dotvb1;
idotvb2 = i2RO*dotvb2;
idotvb3 = i3RO*dotvb3;

dotdotd1 = idotvb1(3)+d1*(iw1.')*iw1;
dotdotd2 = idotvb2(3)+d2*(iw2.')*iw2;
dotdotd3 = idotvb3(3)+d3*(iw3.')*iw3;

idotw1 = (1/d1)*cross(isi,idotvb1)-(2*dotd1/d1)*iw1;
idotw2 = (1/d2)*cross(isi,idotvb2)-(2*dotd2/d2)*iw2;
idotw3 = (1/d3)*cross(isi,idotvb3)-(2*dotd3/d3)*iw3;

dotw1 = OR1*idotw1;
dotw2 = OR2*idotw2;
dotw3 = OR3*idotw3;

dotdotth1 = dotw1(3);
dotdotth2 = dotw2(3);
dotdotth3 = dotw3(3);

idotv11 = -e1*cross(idotw1,isi)-e1*cross(iw1,cross(iw1,isi));
```

```
idotv12 = -e1*cross(idotw2,isi)-e1*cross(iw2,cross(iw2,isi));
idotv13 = -e1*cross(idotw3,isi)-e1*cross(iw3,cross(iw3,isi));

idotvr1 = dotdotd1*isi + (d1-e2)*cross(idotw1,isi) + (d1-e2)*cross(iw1,cross(iw1,isi)) +
2*dotd1*cross(iw1,isi);
idotvr2 = dotdotd2*isi+(d2-e2)*cross(idotw2,isi)+(d2-e2)*cross(iw2,cross(iw2,isi)) +
2*dotd2*cross(iw2,isi);
idotvr3 = dotdotd3*isi+(d3-e2)*cross(idotw3,isi)+(d3-e2)*cross(iw3,cross(iw3,isi)) +
2*dotd3*cross(iw3,isi);

% Calculate Velocity of Actuated Joints and Every Link Part
Jp = [iJb1z;iJb2z;iJb3z];
dotq = Jp*dotxp;

sz = size(iJb1x);

iJ11 = (1/d1)*[-e1*iJb1x; -e1*iJb1y; zeros(sz); -iJb1y; iJb1x; zeros(sz)];
iJ12 = (1/d2)*[-e1*iJb2x; -e1*iJb2y; zeros(sz); -iJb2y; iJb2x; zeros(sz)];
iJ13 = (1/d3)*[-e1*iJb3x; -e1*iJb3y; zeros(sz); -iJb3y; iJb3x; zeros(sz)];

iJr1 = (1/d1)*[(d1-e2)*iJb1x; (d1-e2)*iJb1y; d1*iJb1z; -iJb1y; iJb1x; zeros(sz)];
iJr2 = (1/d2)*[(d2-e2)*iJb2x; (d2-e2)*iJb2y; d2*iJb2z; -iJb2y; iJb2x; zeros(sz)];
iJr3 = (1/d3)*[(d3-e2)*iJb3x; (d3-e2)*iJb3y; d3*iJb3z; -iJb3y; iJb3x; zeros(sz)];

idotx11 = iJ11*dotxp;
idotx12 = iJ12*dotxp;
idotx13 = iJ13*dotxp;

idotxr1 = iJr1*dotxp;
idotxr2 = iJr2*dotxp;
idotxr3 = iJr3*dotxp;
```

```
%Inertia and Applied Wrenches.

g = [0; 0; -9.80665];
mi = 1; mri = 1; mp = 1.6;
BIp = diag([0.00578477672 0.00578477672 0.01145826355]);
OIp = ORB*BIp*BRO;
iIi = diag([0.03003800838 0.03003800838 0.00003405505]);

Fp = [-mp*dotvp;-OIp*dotwp-cross(wp,(OIp*wp))];

iF11 = [-mi*idotv11; -iIi*idotw1-cross(iw1,(iIi*iw1))];
iF12 = [-mi*idotv12; -iIi*idotw2-cross(iw2,(iIi*iw2))];
iF13 = [-mi*idotv13; -iIi*idotw3-cross(iw3,(iIi*iw3))];

iFr1 = [-mi*idotvr1; -iIi*idotw1-cross(iw1,(iIi*iw1))];
iFr2 = [-mi*idotvr2; -iIi*idotw2-cross(iw2,(iIi*iw2))];
iFr3 = [-mi*idotvr3; -iIi*idotw3-cross(iw3,(iIi*iw3))];

T = [t1; t2; t3];

Eqn = (Jp.')*T + Fp + (iJ11.')*iF11 + (iJ12.')*iF12 + (iJ13.')*iF13 + (iJr1.')*iFr1 +
(iJr2.')*iFr2 + (iJr3.')*iFr3;

eqn = [eqn(1,:);eqn(2,:); eqn(6,:)];

[t1, t2, t3] = solve(eqn == 0);
t1 = vpa(t1, 8);
t2 = vpa(t2, 8);
t3 = vpa(t3, 8);

T = [t1; t2; t3];
```